THE BIOORGANOMETALLIC CHEMISTRY OF IRON AND THE DIATOMIC LIGANDS CO AND NO AS RELATED TO HYDROGENASE ACTIVE SITES AND DINITROSYL IRON COMPLEXES

A Dissertation

by

RYAN DAVID BETHEL

Submitted to the Office of Graduate and Professional Studies of
Texas A&M University
in partial fulfilment of the requirements for the degree of

DOCTOR OF PHILOSOPHY

Chair of Committee,	Marcetta Y. Darensbourg
Committee Members,	Michael B. Hall
	Tatyana I. Igumenova
	Paul A. Lindahl
Head of Department,	David H. Russell

December 2014

Major Subject: Chemistry

ABSTRACT

The discovery of a diiron organometallic active site, found in the [FeFe]-Hydrogenase (H_2ase) enzyme, has led to a revisiting of the classic organometallic chemistry involving the Fe-Fe bond and bridging ligands. This diiron site is connected to a mainstay of biochemistry, a redox active 4Fe4S cluster, and the combination of these units is undoubtedly connected to the enzyme's performance. The regioselectivity of CO substitution on the diiron framework of the so-called parent model complex (μ-pdt)$[Fe(CO)_3]_2$, (pdt = propane-1,3-dithiolate), and its derivatives, informs on the interplay of electron density in the diiron core of the enzyme active site. The structural isomers (μ-pdt)$[Fe(NHC)(NO)(PMe_3)][Fe(CO)_3]^+$ and (μ-pdt)(μ-CO)$[Fe(NHC)(NO)][Fe(PMe_3)(CO)_2]^+$, synthesized through CO substitution by opposing nucleophilic (PMe_3) and electrophilic (NO^+) ligands provide insight into the reactivity of both irons as a function of their π-acidity.

The intramolecular fluxional processes of a series of (μ-SRS)$[Fe(CO)_3]_2$ complexes allows for the generation of an open site mimicking the structure of the H_2ase where H^+ binds in the catalytic cycle of H_2 production. Density Functional Theory (DFT) was used to support the dynamic ^1H and ^{13}C NMR spectroscopic studies that established the energy barriers to both the chair/boat interconversion of FeS_2C_2X, where X = NR or CR_2, and the rotation of the $Fe(CO)_3$ moiety, a process essential to the formation of an open site. It was determined that the rotation barrier is correlated with the steric bulk of the bridging ligand

that can be directed towards the iron. This is seen with the methyl substituent in both $N(CH_3)$ and $C(CH_3)_2$ producing a lower barrier to $Fe(CO)_3$ rotation than the NH and CH_2 analogues, while the steric bulk of $NC(CH_3)_3$ cannot be directed to the iron and results in a higher barrier than both NH and $N(CH)_3$.

Another class of bioorganometallic molecules, the dinitrosyl iron complexs (DNICs), is formed *in vivo* as the product of NO degradation of iron-sulfur clusters; DNICs are thought to have possible NO storage and transport roles in the body. Computational investigations utilizing DFT have been used to support synthetic and kinetic studies of the reactivity of one such complex, $(NHC)(SPh)Fe(NO)_2$, (NHC = N-heterocyclic carbene) with CO.

TABLE OF CONTENTS

Page

LIST OF FIGURES

Page

LIST OF TABLES

CHAPTER I

INTRODUCTION TO HYDROGENASES*

Introduction

Hydrogenase

The hallmarks of transition metal-organic chemistry are well represented in the catalytic active sites of the hydrogenases. They include low valent metals that are stabilized by π-accepting ligands such as carbon monoxide and cyanide, capable of supporting η^2-H_2 or hydrides as substrates or ligands, and found in molecular constructions that likely contain metal-metal bonds and bridging carbonyls. Even the air sensitivity of most hydrogenases, and light sensitivity of some, are nuisances that synthetic organometallic chemists have learned to accommodate.

In the mid-1990s, six decades after the report of the discovery of hydrogen metabolizing enzymes in methanogenic archaea by Marjory J. Stephenson and Leonard H. Stickland,[1] a confluence of techniques, vibrational spectroscopy (with isotopic labeling)[2-5] and protein crystallography,[6-8] provided convincing evidence that the bimetallic active site of [NiFe]-hydrogenase, [NiFe]-H_2ase, surprisingly contained an iron bound to a carbonyl and two cyanide ligands. Shortly thereafter, vibrational spectroscopy in the isolated, diatomic

*Reproduced with permission from Bethel, R. D.; Darensbourg, M. Y. "Hydrogenase" in *Bioorganometallics* Salmain, J., Ed. 2014; Vol. 2. Copyright 2014 John Wiley and Sons

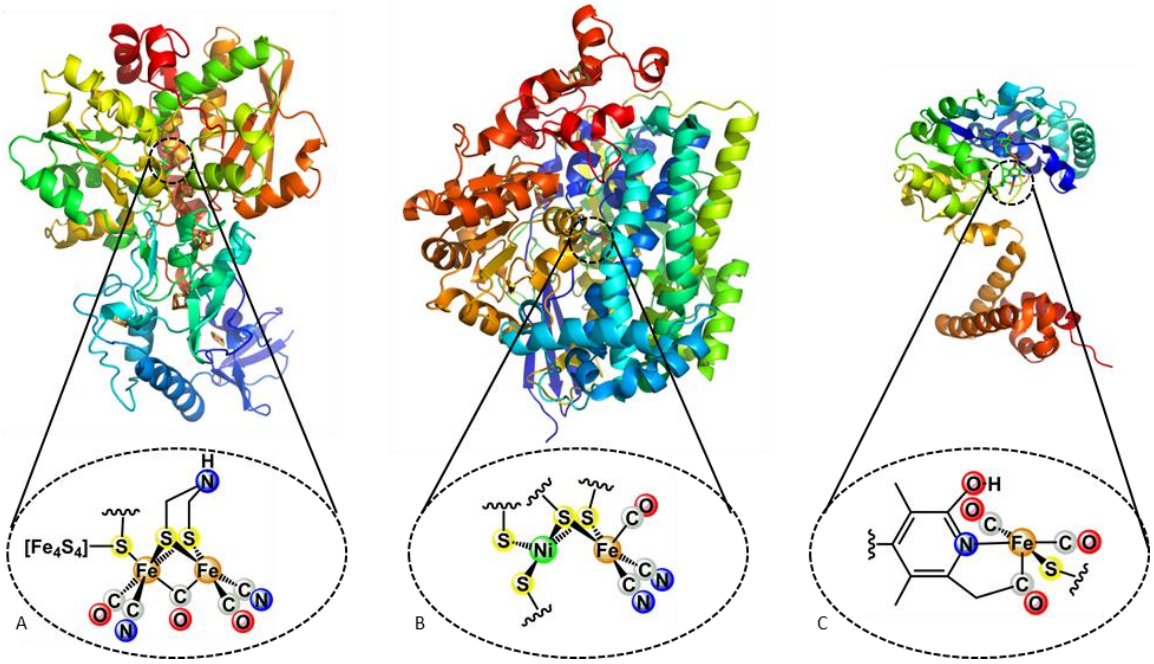

Figure I-1. Ribbon diagrams of the three known classes of hydrogenase; [FeFe]-H_2ase (A),[9] [NiFe]-H_2ase (B),[7,21] and [Fe]-H_2ase (C),[14,15] from protein crystallography. The bioorganometallic active sites, below, demonstrate the unprecedented carbonyl and cyanide ligands, bound to low-valent iron (I) and iron (II).

region of the IR spectrum confirmed the presence of ν(CO) and ν(CN) absorbances in the "all-iron" or [FeFe]-H_2ase, as indicated in protein crystal structures.[9-13] That the highly light sensitive mono-iron or [Fe]-H_2ase likewise contained CO ligands,[14-17] recognized in 2004, made clear that the active sites of the hydrogenase enzymes were most assuredly related to organometallic chemistry, Figure I-1.

Thus, the powerful principles and tenets of transition metal-organic chemistry, a field that matured almost concomitantly with the major advances in hydrogenase science, may be, and indeed are, used in the design of synthetic analogues that reproduce key features of

the active sites and that may lead to understanding the enzymes' mechanisms. It has been generally anticipated that such synthetic analogues might also be developed as robust, base metal catalysts to perform the functions of the [NiFe]- and [FeFe]-H_2ase enzymes, that is, under the mildest of conditions, the controlled dihydrogen oxidation to protons and electrons or proton reduction to dihydrogen.

The widespread biological significance of hydrogenase enzymes was recognized soon after their discovery in the early 1930s.[1] Since that time, hydrogenase activity has been established in a wide range of microorganisms; primarily within the domains of Archaea and Bacteria, but with a presence in Eukarya as well.[18] These include, but are not limited to, methanogens, rumen bacteria, sulfate reducers, Fe^{3+} reducers, photosynthetic O_2 reducers, anaerobic fermenters, and aerobic H_2 and N_2-fixing bacteria.[19] A diverse community of scientists has contributed to all aspects of their characterization. Each decade since the initial discovery has seen major advances, from Hoberman and Rittenberg's discovery of the inhibitors such as oxygen, carbon monoxide, and cyanide in the 1940s[19] to the soluble hydrogenases from *Clostridium* and *Desulfovibrio* first obtained in the 1950s.[20,21] In the 1960s, many proteins involved in biological redox processes were found to contain cysteine-bound iron and inorganic sulfide.[22] By the 1970s, hydrogenases were recognized to contain these iron-sulfur clusters, which were implicated in the role of transporting electrons to and from the active site.[23]

As the major class of hydrogenases contained EPR signals attributed to paramagnetic nickel in different redox levels, the 1980s brought contributions from

bioinorganic/biophysical chemists that further characterized the isolated, oxidized states of [NiFe]-H_2ase.[24-26] The breakthrough that provided the impetus for traditional organometallic chemists to link their expertise with biology came in the 1990s in the form of x-ray diffraction analysis of crystalline proteins, coupled with IR spectroscopy, as described above.

Organometallic-like functions of the bifunctional enzyme acetyl-CoA and carbon monoxide dehydrogenase, ACS/CODH, also call on nickel in ACS and nickel plus iron in the CODH active sites.[27] It is noteworthy that both biocatalysts are multimetallic: two S-bridged nickels are in ACS and nickel is surrounded by S-ligands and bridges to iron in CODH. Although numerous mechanisms of both ACS and CODH have been proposed, one common feature is the inclusion of Ni-C bonds, with both CO and CH_3 ligation.[28,29] As of this dissertation, experimental evidence for a naturally occurring Ni-CO is lacking. Of course the most widely accepted organometallic in biology is based on cobalt in the B_{12} vitamin. Methylcobalamin, containing Co^{3+}-CH_3, is an established source of methyl radicals, formed from the homolytic decomposition of the reduced Co^{2+}-CH_3. The resulting Co^{1+} then regenerates into Co^{3+}-CH_3 by nucleophilic attack of the electron rich Co^{1+} on a CH_3-X.[30]

Myriad functions of iron in biology include roles in catalysis, electron transport and storage, and structure stability. In some metalloproteins, iron is found as an integral component of the peptide, attached to amino acid residues with oxygen, nitrogen, and sulfur donor atoms assembled so as to achieve fairly regular and recognizable coordination

geometries. Other proteins utilize cofactors, such as iron-bound heme, that are assembled whole and delivered to the protein as a stand-alone, often weakly coordinated, unit. Iron is well known to exist in two biologically accessible redox levels, ferrous (Fe^{2+}) and ferric (Fe^{3+}). These are the typically observed oxidation states in such famous systems as the iron sulfur clusters and hemoglobin. Only recently has the veracity of the reactive ferryl (Fe^{4+}) oxo species been accepted within bioinorganic chemistry.[31] In contrast, the fundamental organometallic iron complexes find iron in lowest known oxidation states, e.g., Fe^{2-} in $Fe(CO)_4^{2-}$ or Fe^0 in $Fe(CO)_5$, $HFe(CO)_4^-$ or $Fe_3(CO)_{12}$. Such low valent iron species, requiring toxic CO ligands for electron delocalization, would be reasonably assumed to conflict with nature. Nature's control of such contradictions is of course the stimulus that drives the field of bioorganometallics.

The Chemistry of Hydrogen

The deceptively simple reactions facilitated by the hydrogenases are shown in Equations I-1, I-2, I-3, and I-4. The processing of hydrogen is needed in biology for relief of excess reducing equivalents, or alternatively, to use H_2 as a source of electrons, Equations I-1 and I-2. Indeed, some of the life forms mentioned above utilize H_2 as the primary energy

$$H_2 \rightleftharpoons 2H^+ + 2e^- \quad (1)$$

$$H_2 \rightleftharpoons H^+ + H^- \quad (2)$$

$$H_2 + D_2O \longrightarrow HD + DHO \quad (3)$$

$$H_2 + D_2O \longrightarrow D_2 + H_2O \quad (4)$$

$$Rh^{1+} + H_2 + Sub^{ox} \longrightarrow (Sub)Rh^{3+}(H)_2$$
$$(Sub)Rh^{3+}(H)_2 \longrightarrow Rh^{1+} + H_2Sub^{red} \quad (5)$$

Equations I-1, I-2, I-3, I-4, and I-5

source. The mid-Indian Ocean hydrothermal vents provide an example of an entire ecosystem that uses non-photosynthetic carbon sources with hydrogenase-containing microbes as the producers of H_2, the energy currency.[32,33] Assays, as indicated by Equations I-3 and I-4, reflect the heterolytic mechanism of H_2 cleavage or formation whereby acid/base H/D exchange can take place.[34]

The importance of hydrogen as a reagent in biology and in chemistry can hardly be overstated. The chemical industry and synthetic organic chemistry have realized many goals by developing homogeneous reduction catalysts, typically based on heavier noble metals such as platinum, rhodium, iridium, and palladium. These metals readily undergo two-electron redox level changes; Equation I-5 provides an example of hydrogenation of an organic substrate, such as an olefin, by the rhodium (I) based Wilkinson's catalyst.

The extraction of electrons from H_2 is used for inorganic reduction processes, e.g. sulfate to hydrogen sulfide or iron (III) to iron (II). Thus, the [NiFe]-H_2ase, typically biased towards H_2 uptake is a hydrogenase common to such organisms that perform these reactions.[18] Hydrogen oxidation is also a prominent feature of fuel cells, requiring catalysts for which the most efficient is the expensive and resource-limited platinum.[35] The reverse reaction, generation of H_2 from protons in an aqueous solution and the direction for which the [FeFe]-H_2ase is typically biased, is the desired source of hydrogen for the reactions described above. Hence, a significant target of bioorganometallic chemistry is the synthesis of model complexes of the hydrogenase active sites that might

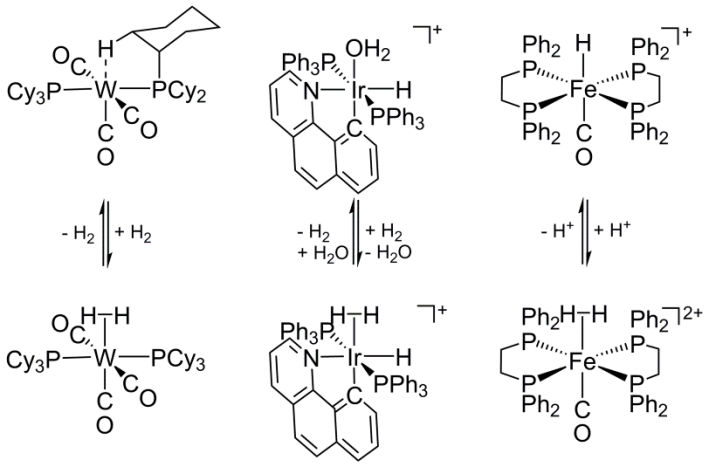

Figure I-2. Metal-H_2 complexes explored by Kubas,[37] Crabtree,[41] and Morris.[45]

reproduce the activity of those enzymes—resulting in cheap catalysts based on first row transition metals.

Dihydrogen Metal Complexes

The coordination chemistry of the hydrogen molecule has been a critical challenge for organometallic chemists.[36,37] As the seminal model for molecular bonding, with two electrons in a single σ-bonding orbital, H_2 is the simplest molecule. However, the strong H-H bond (436 kJ/mol) and lack of non-bonding electrons to act as a "handle" by which to manipulate the molecule, renders it relatively inert to further bonding as an intact molecule. The first metal-dihydrogen complex, initially reported by Kubas and coworkers in 1980,[37] was characterized and accepted as a true molecular hydrogen adduct in 1984.[38] This tungsten(0)-dihydrogen complex, $(\eta^2\text{-}H_2)W(CO)_3(PCy_3)_2$, formed immediately upon the exposure of H_2 to a five-coordinate d^6 tungsten(0), ligated by two bulky phosphine

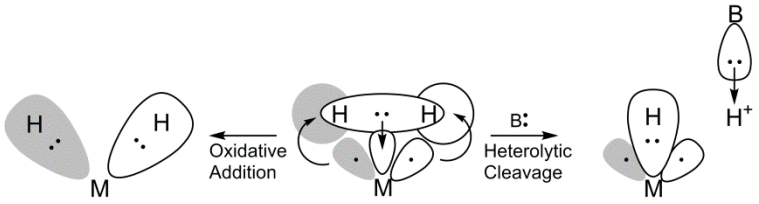

Figure I-3. H_2 binding with H_2 σ-donation and π-back donation into H_2 σ* (center), the oxidative addition of H_2, forming a $M^{n+2}(H)_2$ complex (left), and heterolytic cleavage leading to deprotonation (right).[36,41]

ligands and three carbonyls, Figure I-2. An intramolecular, agostic interaction between the C-H of a cyclohexyl moiety of one of the phosphines protected the sixth coordination site. This weak interaction could be displaced by H_2, in addition to many other small molecules such as N_2. The H_2 in this complex is bound to the tungsten side on, in a non-classical three-center, two-electron bond. As the two electrons originate in the σ-bonding orbital of H_2, all such η^2 complexes (including H-H, C-H, Si-H, etc.) were termed "σ complexes" by Crabtree.[39] The elongation of the H-H bond, from 0.74 Å in the free H_2 to 0.89 Å in the bound molecule, indicates the intact H_2 is destabilized, or more accurately activated, when bound to the metal. The hydrogen could be removed under vacuum in a fully reversible process. The ability of metal-hydrogen complexes to reversibly associate and dissociate H_2 is of critical importance to the hydrogenase enzymes, as is the rendering of the H_2 susceptible to heterolytic (H^+/H^-) splitting.

Since this first system, hundreds of metal-(η^2-H_2) complexes have been synthesized using nearly every transition metal, from vanadium to platinum.[40] The majority contain

octahedral, d^6 metals that are relatively low-valent, with a relatively accessible open site. In such complexes, the metal must be tuned such that its σ-accepting capability will allow H_2 to bind, while π-back donation from filled metal d orbitals into the σ* orbital of the H_2 must not be excessive, Figure I-3. Highly Lewis acidic metal centers with insufficient σ-accepting capacity are unfavorable for H_2 binding, while excessive electron density on the metal results in full oxidative addition and formation of a metal-dihydride, with increase in the oxidation state of the associated metal. The instability of H_2 adducts of strong main group Lewis acids, such as CH_3^+ and BBr_3 support the idea that stabilization of the H_2 σ* orbital by the acceptor's d electrons is required. Even so, the balance of σ-accepting and π-back donation is critical. Often, a π-accepting ligand is *trans* to the H_2 to moderate the back donation.

Soon after Kubas' first report of a dihydrogen-tungsten adduct, Crabtree *et al*. reported an iridium (III) dihydrogen hydride, Figure I-2.[41] At the time, it was anticipated that the reaction of the iridium (III) aqua complex with H_2 would yield the iridium (V) trihydride. Instead, ^{1}H NMR below 260 K clearly showed the presence of two protons at δ = -2.9 and another single proton at δ = -15.3. When warmed to room temperature, the signals coalesce into a single resonance, indicating rapid exchange between the dihydrogen molecule and the hydride.[42-44]

Although both of these metal-hydrogen complexes were synthesized via direct H_2(g) binding, either to an unsaturated precursor or by displacement of a weakly bound solvent molecule, this is not the only technique used. This straightforward reaction proceeds though a characterized hydrogen bond between the incoming acidic proton and the basic hydride, Figure I-4. This scheme has been used on many neutral metal-hydrides, which have been found to be good targets for protonation, forming stable, monocationic metal-hydrogen complexes. In 1997, Forde *et al.* demonstrated that a cationic iron-hydride could also be protonated, forming a dicationic iron-dihydrogen complex, Figure I-2.[45] The iron (II) dihydrogen complex is stabilized by a *trans* π-acidic carbonyl ligand, but the short H-H bond reported, 0.86 Å, as determined by the NMR coupling within the bound HD, indicates that there is little donation into the σ* orbital of the hydrogen.[45] Instead, this complex is almost exclusively stabilized by the H_2 σ-donation. Although the hydrogen is tightly bound, with no loss of H_2 under vacuum at 20˚C, it is strongly acidic. Addition of dry ethyl ether results in deprotonation and reformation of the iron-hydride precursor.[45] Tuning the basicity of the hydride and acidity of the dihydrogen in hydrogenase biases the enzymes towards either H_2 production or oxidation. Thus, our understanding of the organometallic chemistry enlightens our studies of hydrogenase biology, while new

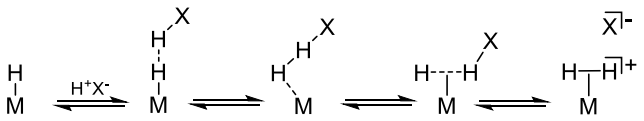

Figure I-4. Protonation of a metal-hydride.[36,41]

understanding of the biology in turn provides new paradigms for the organometallic chemist.

First Coordination Sphere Ligands

As described above, a critical balance of electrophilicity and π-back donating ability of the metal is required, for the uptake and binding of dihydrogen. For a mild two electron electrochemical process, as in the metal-catalyzed proton reduction to dihydrogen, proton coupled electron transfer is required. Both requirements are met for iron in the hydrogenase enzyme active sites by a combination of CO, CN^- and thiolate sulfur, RS^-. Well known for its π-backbonding capability, carbon monoxide delocalizes electron density from the reduced metal, while the anionic X-type ligands, CN^- and RS^-, rely on their capability to morph between strong σ-donor, dative bonds and covalent one-electron bonding. Cyanide and thiolate may be found combined with metals in higher oxidation states; for iron, Fe^{3+} is common. As an excellent 4-electron bridging ligand, RS^- takes on the additional role of maintaining the binuclearity of the [NiFe]- and [FeFe]-H_2ase active sites.

That CN^- is found in the [NiFe]- and [FeFe]-H_2ases and CO is found in all three H_2ases, and that the three enzymes are phylogenetically distinct, speaks to convergent evolutionary processes that recruited these toxic ligands to facilitate the reversible reduction/oxidation process for hydrogen metabolism at iron.

Structure and Function

The Active Sites of the Hydrogenases

Shown in Figures I-5, I-6, and I-7 are graphics depicting the active sites of the hydrogenases, derived from the protein crystal structures as indicated in the captions, Figure I-1. These represent the consensus structures that, in all three hydrogenases, required committed effort over many years, eventually converging on the conclusions shown here; the dedication demonstrated towards this contribution to the hydrogenase field by a broad community of scientists cannot be overestimated. In Figures I-5, I-6, and I-7 we have used ball and stick renditions within ribbon protein structures, and oriented the configurations so as to emphasize the similarities of the pentacoordinate, organoiron units in each.

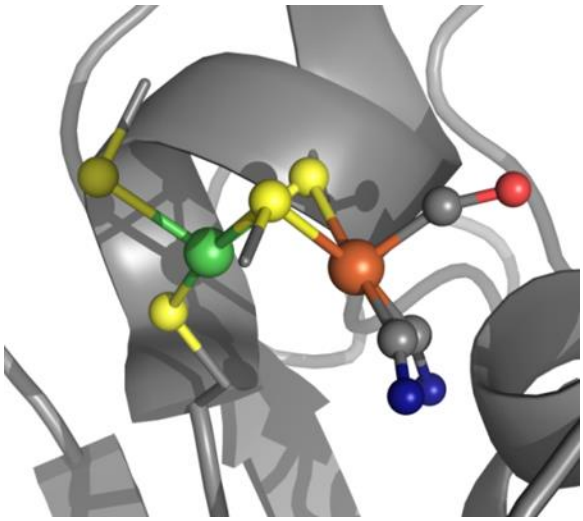

Figure I-5. Active site of [NiFe]-H_2ase.[7,21]

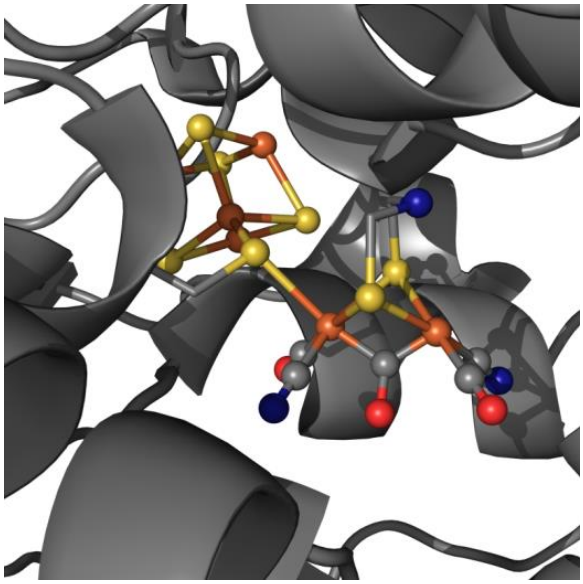

Figure I-6. The active site of the [FeFe]-H_2ase.[9]

[NiFe]- and [FeFe]-Hydrogenase

The first reported (1995) structure of a hydrogenase, [NiFe]-hydrogenase from *D. gigas*, is a heterodimer in which a large subunit contains the [NiFe] active site and a smaller subunit contains several iron-sulfur clusters, Figure I-1.[7] The [FeFe]-H_2ase protein from *C. pasteurianum* is a mushroom-shaped monomer, Figure I-1, for which a consensus active site structure was published in 2000.[9] As with the [NiFe]-H_2ase, a series of iron-sulfur clusters are positioned at ca. 12 Å apart and function as the electron transport route from the exterior of the protein into the active site. While the 4Fe4S cluster closest to the [NiFe]-H_2ase active site is 12 Å away, for [FeFe]-H_2ase the final 4Fe4S cluster is directly attached to the [FeFe] subsite within the 6Fe6S, H-cluster of the protein. Its essential

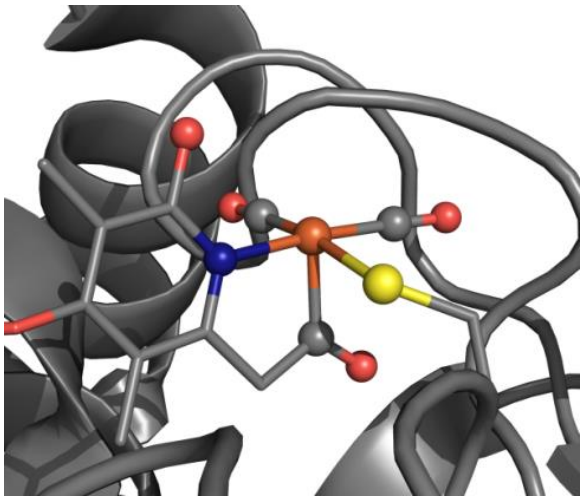

Figure I-7. The active site of the [Fe]-H_2ase.[14,15]

requirement has been established, presumably for both high rates of H_2 production, as well as for activation and electronic tuning of the 2Fe subsite.[46,47]

Thiolate sulfur bridges link the two metals in both the [NiFe]- and the [FeFe]-H_2ase active sites. In the former, the sulfurs are from two of the four protein-bound cysteines that comprise the coordination sphere of the nickel, producing a Ni(μ-SCys)$_2$Fe butterfly shaped core, with Ni-Fe distances that range from ~2.5 Å for the active form (Ni-SI), to ~2.9 Å in the inactive Ni-A and Ni-B forms.[6,8] The larger distance is required for the additional bridging oxy-species. A variant, the [NiFeSe]-H_2ase, has one terminal cysteine replaced by selenocysteine, otherwise the structures are identical.[48] The [NiFeSe]-H_2ase is found to be more oxygen tolerant relative to the [NiFe]-H_2ase, but the basis of the O_2 tolerance is unclear. Recent studies of membrane-bound [NiFe]-H_2ase as in *Ralstonia eutropha* have attributed O_2 tolerance to a unique 4Fe3S cluster with additional cysteines proximal to the active site that aids in rapid repair.[49,50]

For the [FeFe]-H_2ase active site, a unique, abiotic dithiolate bridges the two irons, creating two 6-membered, cyclohexane-like FeS_2C_2N rings displaying typical chair/boat configurations. The central, bridgehead atom of this metallo-heterocycle was the subject of controversy as protein crystallography at typical resolution cannot differentiate between the light atoms: CH_2, NH, or O. Through the use of HYSCORE and ENDOR spectroscopy, Lubitz and coworkers have provided definitive proof that the bridging atom is nitrogen.[51,52] This conclusion has been further supported by Fontecave and coworkers.[53] The mechanistic role played by this pendent amine, or built-in base, for proton shuttling will be discussed below.

[Fe]-Hydrogenase

The mono-iron, [Fe]-H_2ase enzyme is the most recently discovered hydrogenase. Unlike both [NiFe]- and [FeFe]-H_2ases, which are spread across multiple domains with hundreds of species utilizing one or both, that have been known for many decades, [Fe]-H_2ase, the so called "third hydrogenase" was first reported by Thauer in 1990.[54] It is also called H_2-

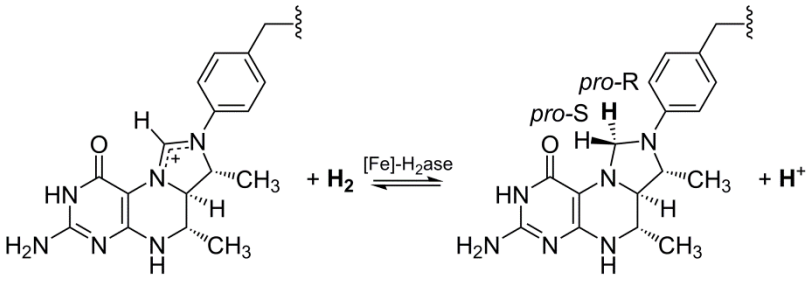

Figure I-8. The reaction catalyzed by [Fe]-H_2ase.[54]

forming methylenetetrahydromethanopterin dehydrogenase (Hmd) and was first isolated from methanogenic archaea grown in the absence of nickel. At the time, the production of N^5, N^{10}-methylenetetrahydromethanopterin (CH_2=H_4MPT) from N^5, N^{10}-methenyltetrahydromethanopterin (CH≡H_4MPT) and H_2, Figure I-8, was found to be catalyzed by an unknown enzyme. Unlike the previously reported hydrogenases, Hmd does not catalyze the reversible interconversion of protons and electrons to H_2, Equations I-1 and I-2, and did not catalyze *per se* the single or double exchange between H_2 and H_2O, Equations I-3 and I-4. Also unlike previously examined hydrogenases, this one contained no iron sulfur clusters—they are not needed; there is no redox chemistry involved. In fact, it was originally thought to contain no metallocenters at all, and was referred to as the "metal-free hydrogenase".[55] It wasn't until 2004 that Lyon *et al.* definitively showed both the existence and catalytic requirement of a single iron atom per enzyme.[15]

The [Fe]-H_2ase is produced by methanogenic archaea that lack access to nickel. When the [NiFe]-H_2ase is not available for the reduction of F_{420} to $F_{420}H_2$, essential to the production of methane, the CH_2=H_4HMPT produced by the [Fe]-H_2ase is capable of carrying out the reduction. It is worth noting that the [Fe]-H_2ase of *M. marburgensis* has a much higher K_m than the [NiFe]-hydrogenase (0.2 mM vs 0.01 mM), and is therefore less active.[56] Thus, the concentration of the [Fe]-H_2ase increases approximately five fold in nickel-limited conditions.

A difficulty in the study of [Fe]-H_2ase is its sensitivity to oxygen and light. Currently, the typical isolation of the functional protein requires first the purification of the inactive

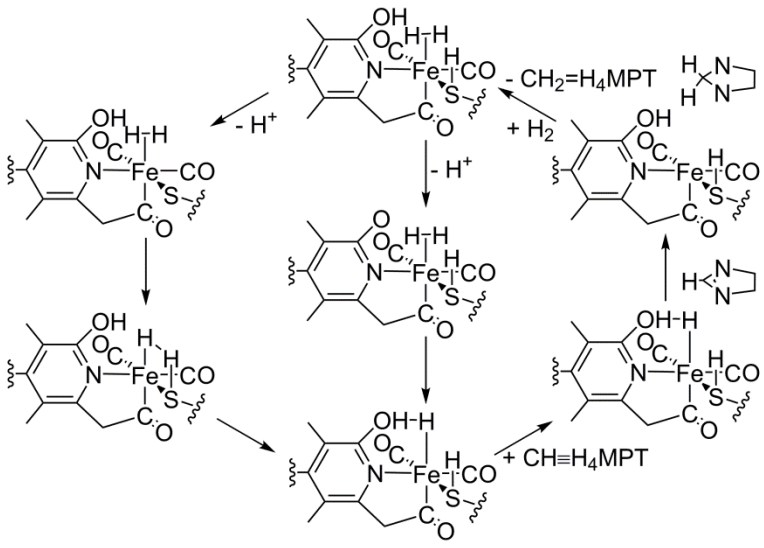

Figure I-9. Proposed mechanism by which [Fe]-H_2ase reduces $CH{\equiv}H_4MPT$ to $CH_2{=}H_4MPT$ utilizing H_2 (only the CN_2C_2 moiety of the cofactor is shown for clarity).[58]

enzyme from the *H. jannaschii* gene (as expressed in *E. coli*), then incorporation of a cofactor isolated from *M. marburgensis*. This cofactor contains the active site itself, and infrared studies have shown that it contains two iron-bound carbonyls in a *cis* configuration.[57] A combination of protein crystallography and EXAFS has resulted in the presently accepted active site structure, Figure I-7. The cofactor is bound to a single iron atom by a pyridinyl nitrogen and an acyl carbon. The two carbonyl ligands and a single cysteinyl sulfur are bound in a square plane with the nitrogen. The sixth coordination site, *trans* to the acyl carbon, is the presumptive site of H_2 binding and activation. The iron is low-spin, d^6, Fe^{II}, and the substrate, $CH{\equiv}H_4MPT$, is positioned directly over the open site on Fe at a distance of *ca.* 3Å.[14]

The Mechanisms of the Hydrogenases

It is noteworthy that despite the separate evolutionary paths and different biosynthetic routes to the three hydrogenase active sites, a constant is the ultimate disposition in all three of a penta-coordinate iron. All three enzymes have iron atoms with two sulfurs (or one S and one N in the case of the [Fe]-H_2ase active site) and diatomic ligands: two cyanides and one carbon monoxide for the [NiFe]-H_2ase; two carbon monoxides and one cyanide for the [FeFe]-H_2ase; and two carbon monoxides and one acyl carbonyl for the [Fe]-H_2ase. With further ligation consisting of a single cysteinyl sulfur and a pyridinyl nitrogen, the apparent simplicity of [Fe]- H_2ase entices us to discern an explanation for its *modus operandi* that is entirely consistent with textbook organometallic chemistry. As hydrogen activation in the three hydrogenases is via heterolysis rather than homolysis of the H-H bond, the single iron of the [Fe]-H_2ase active site and its adjacent ligands must give the minimal mechanism. Nevertheless, as shown in Figure I-9, the computationally investigated catalytic cycle of the [Fe]-H_2ase by Yang and Hall, led to an unexpected dual pathway.[58] After H_2 binding, deprotonation of either the hydroxyl group of the pyridinyl cofactor or the thiol of the coordinated cysteine produced energetically similar pathways. Rearrangement and heterolytic splitting of the H_2 by the newly generated base results in an iron (II) hydride, stabilized by charge delocalization over the adjacent ligands. This hydride is then transferred to the CH≡H_4MPT substrate, generating an equivalent of CH_2=H_4MPT and reforming the catalytic iron center.

While the imidazolium carbocation must be optimally positioned to extract a hydride from H_2, bound to and activated by Fe^{II} in [Fe]-H_2ase, the other hydrogenases are well set up for cooperative interactions and the formation of iron-hydrides. Positioned over the open

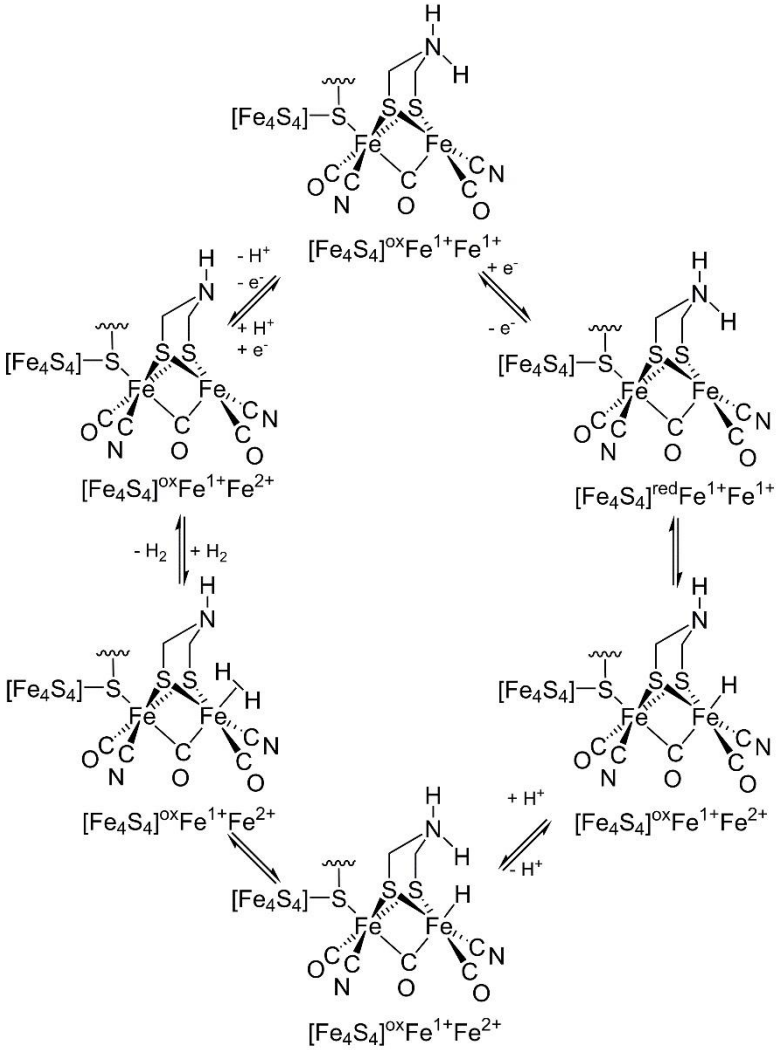

Figure I-10. Proposed mechanism by which [FeFe]-H_2ase reversibly produces (clockwise) and oxidizes (counterclockwise) H_2.[59,60]

site for the [FeFe]-H_2ase is the pendent nitrogen base built into the bridging dithiolate cofactor. This pendent base is attractively available for rapid intramolecular shuttling of a proton into the reduced iron for production of iron hydride in the first step of H_2 formation, followed by a second proton to form Fe^{II}-(η^2-H_2)], Figure I-10.[59,60] Alternatively, in the H_2 uptake process, the pendent base also enables rapid heterolytic bond cleavage of the H_2, forming a protonated amine and iron hydride.

The "open" site on iron in the [NiFe]-H_2ase is oriented towards nickel, hence the cooperative effect for hydrogen uptake or production must involve the ability of nickel or its thiolate sulfur donor to assist iron in the formation of H-bonded species or bridging hydrides.

Original discussions of [NiFe]-H_2ase argued for a Ni-site reactivity based on the observations of paramagnetic nickel and EPR signals that correlated with myriad redox levels of the enzyme. On the basis of FTIR, EPR, electrochemistry, spectroelectrochemistry and X-ray crystallographic studies, nearly a dozen different states of the [NiFe] active site have been assigned. The EPR silent Ni^{2+} species that includes the Ni-SI, Ni-SU, Ni-CO, and other states, can be oxidized to Ni^{3+}, as Ni-A, Ni-B, or Ni-C, or reduced to Ni^{1+}, as Ni-L; however, the iron remains low-spin Fe^{2+}.[61] Currently most of the redox levels can be ascribed to inactive oxidized, oxy-species in the active sites of the enzymes which can be repaired electrochemically as well as by hydrogen reduction.[49,62,63]

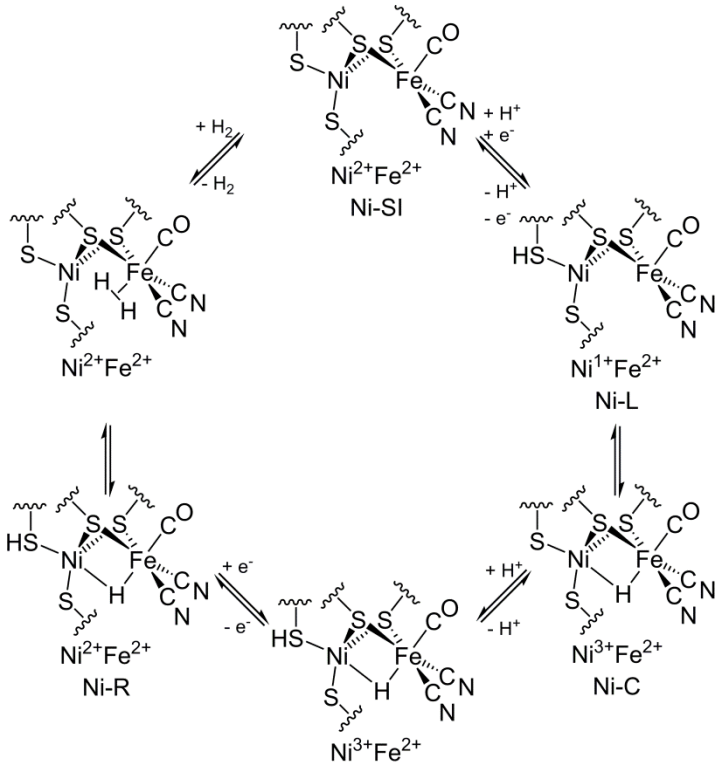

Figure I-11. Proposed mechanism by which [NiFe]-H_2ase reversibly produces (clockwise) and oxidizes (counterclockwise) H_2.[59,60]

The most probable mechanism is shown in Figure I-11, wherein the nickel does indeed change oxidation states, involving Ni(I) and Ni(III) as well as Ni(II). However in the H_2 uptake and oxidation process (the counter-clockwise route), the Fe(II) traps the H_2, as it does in the [Fe]- and [FeFe]-H_2ase, while the roles of the nickel appear to be stabilization of the once-formed hydride, and in easing the transfer of electrons to the iron-sulfur clusters. It should also be noted that with changes in the oxidation state of the nickel, the bridging thiolates change their donating character to iron, hence the $Ni(SCys)_4$ also serves the role of a redox-active, metallodithiolate ligand.

Biosynthesis of the Active Sites

Biosynthesis of Hydrogenase Active Sites

The assembly of the sulfur-rich hydrogenase active sites is a challenge both in nature and at the chemist's benchtop—or in the chemist's glove box—as these molecules are usually air-sensitive, requiring the exclusion of oxygen in nature and in the laboratory. While nature must cope with the production of all components, including control of the diatomic ligands typically toxic to life forms,[64] the chemist has CN^- and CO ligands readily available. In an insightful microreview, Professor Kaz Tatsumi expresses the great challenge to synthetic chemists in strategies to the sulfur-rich [NiFe]-biomimetics is the propensity of thiolate sulfur to bridge metals indescrimately, with resulting self-assembly of large, and largely insoluble, metal clusters containing all iron, all nickel or mixtures of Fe and Ni.[65] Nature has the advantage here as the cysteinyl sulfur donor sites that will bind the metals in proteins are in an evolutionarily perfected protein matrix that fixes a single metal at a time.

Biosynthesis of [NiFe]-Hydrogenase

Given its complexity, it is not surprising that the natural biosynthesis of the [NiFe]-H_2ase active site requires a suite of proteins, at least seven so-called "maturases", which carry out a variety of tasks.[66-68] The order of events along the way to the finished hydrogenase proteins is given in the abbreviated cartoon depiction in Figure I-12. While for [NiFe]-H_2ase the source of carbon monoxide is currently not known, carbamoyl phosphate (CP), a natural product of ammonia and bicarbonate, is the source of cyanide.[64-66] Two maturases, HypE and HypF, hydrolyze the phosphate from the carbamoyl moiety and transfer it to a cysteinyl sulfur. From there, the latter is dehydrated to form a thiocyanate, which donates a CN^- to the pre-active site iron found in a scaffold protein, HypD. An

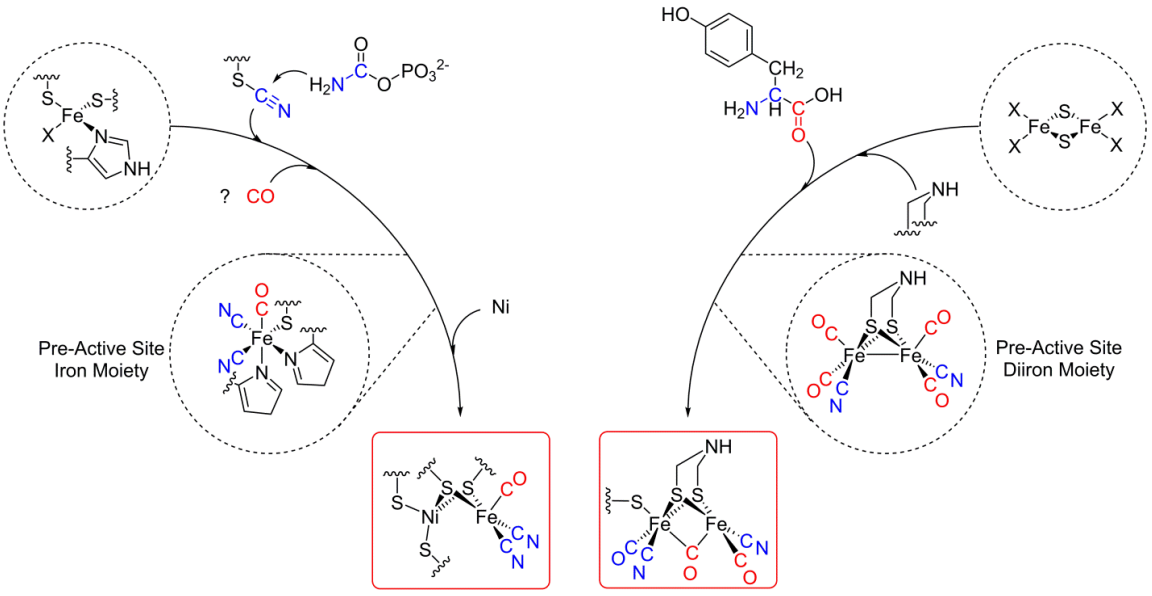

Figure I-12. Abbreviated descriptions of biosynthetic paths to [NiFe]- and [FeFe]-H_2ase active sites.[64]

intact $Fe(CN)_2(CO)$ unit is transiently bound before being transferred, prior to the nickel, into the apo-[NiFe]-H_2ase active site with the assistance of an additional maturase, HypC.[69] The nickel storage protein SlyD is proposed to donate Ni to the maturases HypA and HypB, which act in concert to insert the nickel into the active site, transferred to cysteine sulfurs already positioned. At this point, the [NiFe]-H_2ase active site is complete, as described above. Nevertheless, some hydrogenases are not "turned on" until activated by an additional enzyme, which snips the end of the protein, resulting in assembly channel collapse in the large protein subunit. Subsequent protein aggregation with the small subunit that contains the electron-conducting, iron-sulfur clusters completes the active biocatalyst.[67,68]

Biosynthesis of [FeFe]-Hydrogenase

As expected, the biosynthetic path to the 2Fe subsite, the catalytic engine in the H-cluster of [FeFe]-H_2ase, is simpler than that of the [NiFe]-H_2ase active site, see the right side of Figure I-12.[70] Diiron units are common in metallobiology and an attractive proposal is that nature uses a diiron precursor, as of now ill-defined, found in a scaffold protein known as HydF, modifying it with the diatomic ligands produced by the HydG protein, and the unique bridging dithiolate cofactor that is proposed to be developed on HydE. Notably, HydG has been proven to generate both CO and CN^- from the amino acid tyrosine, Figure I-12.[71,72] The tyrosine undergoes a radical-induced decomposition to yield the carbonyl and cyanide, through interaction of either a glycyl radical (formed via a homolytic route) or a dehydroglycine moiety (formed via a heterolytic route) with an iron-sulfur cluster on

the maturase.[73,74] It has been recently predicted that an individual iron atom, with diatomic ligands in place, may be inserted into HydF, there to combine with another.[75] The formation of the dithiolate would then occur after the iron atoms are in place, perhaps even using them as a scaffold. While the structure of this 2Fe complex has not yet been established, HydF has been shown to bind the [FeFe]-H_2ase model complexes, (μ-$(SCH_2)_2X)[Fe(CO)_2(CN)]_2^{2-}$, where X = CH_2, NH, or O, and insert them into the hydrogenase protein.[53,72] In nature, the pre-active site complex is assembled on HydF, and subsequently delivered to the apo-hydrogenase, apo-HydA. This active site location already contains a 4Fe4S cluster at the end of a tunnel, which then collapses to form the cavity that encloses the fully assembled H-cluster, or the holo-HydA.[76,77]

Synthetic Analogues of the Active Sites

Models of the [NiFe]-Hydrogenase Active Site

While it was known early on in their study that hydrogenases were rich in iron in the form of iron-sulfur clusters, it was not until 1980 that the presence of a single nickel atom was verified in the predominant class of hydrogenases, so named then as [NiFe]-H_2ase, with the Fe representing the multiple irons from the clusters.[78] From EPR and EXAFS spectroscopic studies, the coordination environment about nickel was suggested to contain sulfur donors, and so the first reported models of the [NiFe]-H_2ase consisted of nickel-thiolate complexes.[79,80] This direction yielded a wealth of information in nickel-sulfur coordination chemistry and helped address the control that must be exercised to avoid S-

aggregation of large clusters. In retrospect, we now view those homoleptic $Ni(SR)_4^{2-}$ compounds as apt models of the distorted geometry of the nickel site in [NiFe]-H_2ase.[81]

The discovery of the $Fe^{II}(CO)(CN)_2$ unit bound to the nickel site gave rise to a focus on the synthesis of S-bridged, Ni-Fe heterobimetallics. This paradigm shift offered a new challenge, and a new assay for proof of progress. For the first time in biomimetic synthesis, the infrared spectroscopy of diatomic carbonyl and cyanide ligands, mainstays of organometallic chemistry, could be utilized to link synthetic models to the biological moieties they were made to mimic. One such model, the piano-stool (η^5-C_5H_5)$Fe(CO)(CN)_2^-$ complex,[82] Figure I-13, was shown to have an identical infrared stretching pattern to that of the protein in its oxidized, as-isolated form.[5] This result fully

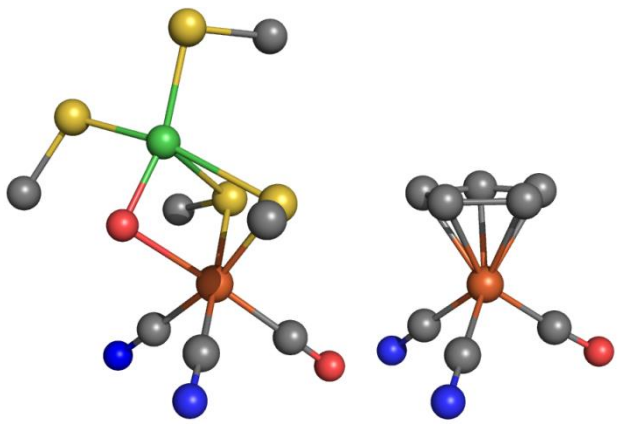

Figure I-13. An organometallic analogue of the $Fe(CN)_2(CO)$ unit in the as isolated, oxidized [NiFe]-H_2ase active site.[82]

corroborated the identity and number of the diatomics in the organoiron portion of the active site and the oxidation state of iron, Fe^{II}.

Several reviews of hydrogenase active sites have extensive descriptions of models prepared over the past two decades and the interested reader is encouraged to explore the structures from effective synthetic designs described therein.[65,79,81,83,84] As in any natural product synthetic effort, selection of precursor is key to success. The structures selected for display in Figure I-14 are largely from recent efforts and were all designed as models of the [NiFe]-H_2ase active site; core features are bridging dithiolates that reproduce the Ni(μ-S_2)Fe rhombic or "butterfly" center.[85-92] In general the nickel is square planar, and the iron has diatomic ligands. Infrared spectroscopy is useful to monitor extent of reaction; vibrational spectroscopy also reports on the match or mismatch of the diatomic ligands' electronic environment with those of the enzyme active sites in various stages of oxidation or inhibition by addition of exogenous CN or CO ligands. In the cases shown in Figure I-11, X-ray crystallography has determined Ni- - Fe distances in a range of 2.5 - 3.3 Å.

As all thiolate-S bridged heterobimetallics can be considered as metallodithiolate ligands complexed to a second metal, we have used that perspective to consider the origin of the [NiFe] complexes in Figure I-14. Complexes on the left have used an intact nickel dithiolate added to an iron precursor containing *cis* leaving groups or labile ligands. The Schröder complex was prepared by reaction of the square planar (dppe)Ni^{II}(pdt) complex, pdt = propane dithiolate, with a source of $Fe^0(CO)_3$.[85] Interestingly the (dppe)Ni(μ-

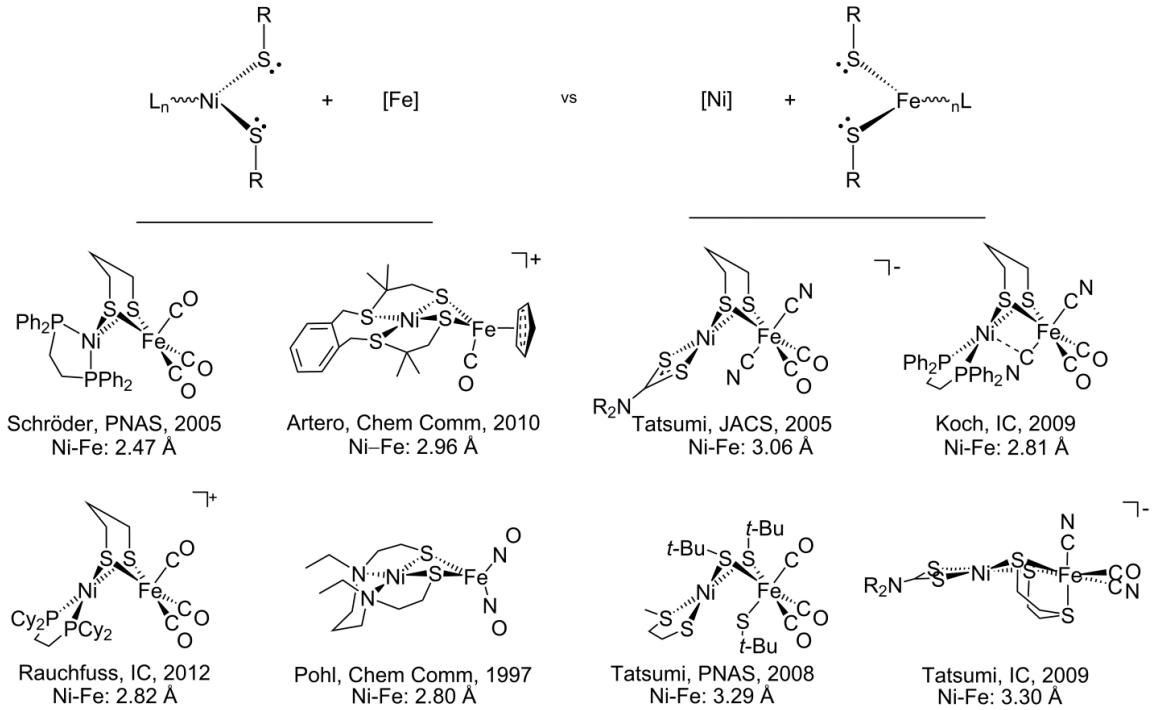

Figure I-14. A selection of biomimetics of the [NiFe]-H_2ase active site.

pdt)$Fe(CO)_3$ product shows a tetrahedral twist within the Ni coordination geometry that implies internal reduction resulting in a $Ni^I(\mu\text{-pdt})Fe^I$ formulation. This complex contains a Ni—Fe distance of 2.47Å, consistent with a M-M bond. Further work with this class of NiFe bimetallics found that the bridging bidentate dithiolates supported a one-electron oxidation, resulting in lengthening of the Ni—Fe distance to 2.82 Å, presumably due to reducing the Ni—Fe bond order to 0.5.[91] Early designs used square planar NiN_2S_2 complexes in combination with iron carbonyls to yield adducts of $Fe^0(CO)_4$ and Fe^{II}, simply illustrating the principle of NiN_2S_2 as metalloligands to iron in two redox levels.[93]

Tetradentate chelating ligands such as Artero's NiS'_2S_2 dithiolate has been found to displace the labile THF ligand from $[(\eta^5\text{-}C_5H_5)Fe(CO)_2THF]^+$ to first add the nickel dithiolate as a mono-dentate metallo ligand, followed by CO displacement to arrive at the bidentate $Ni^{II}(\mu\text{-}SR)_2Fe^{II}$ product, with a long Ni---Fe distance of 2.9 Å.[92] This complex is an electrocatalyst for H^+ reduction/H_2 production using trifluoroacetic acid as proton source and operating at -1.47 V. The same $NiS_2S'_2$ complex was used by Bouwman, *et al*., in the synthesis of NiFe complexes wherein the $Fe(NO)_2$ unit is the iron acceptor.[94] The $Fe(NO)_2$ unit has also been useful to Pohl (1997) and Liaw (2001) in the preparation of $Fe(NO)_2$ derivatives.[89,95] Notably the $Fe(NO)_2$ unit may be considered as an isoelectronic analogue of $Fe(CO)_3$ or a combination of diatomics in $Fe(CO)_x(CN)_{3-x}$.

Complexes on the right of Figure I-14 were prepared from reactions of intact iron(II) dithiolates combined with complexes of nickel containing good leaving groups. Thus the $(pdt)Fe(CO)_2(CN)_2^-$ complex anion reacts with the dithiocarbamate nickel(II) complex containing Br^- and PPh_3 as leaving groups.[87] The resulting complex has cyanide and carbonyls on 6-coordinate iron(II) and a Ni---Fe distance of ca. 3 Å. Jiang and coworkers have derived a similar $Ni^{II}(\mu\text{-}pdt)Fe^{II}$ core in a neutral complex, again converging on a dicyano iron dicarbonyl acceptor with a Ni---Fe distance of 2.81 Å and a cyanide positioned as a bridging ligand.[88] Both Tatsumi, *et al*. and Jiang *et al*. noted that similar NiFe bimetallics with monodentate thiolates as bridging ligands had longer Ni^{II} - - -Fe^{II} distances.[86]

In order to achieve an $Fe^{II}(CN)_2(CO)$ unit thiolate-S bridged to nickel, Tatsumi and coworkers incorporated 3-thiapentanedithiolate into the iron precursor.[90] In the reaction with the dithiocarbamate nickel(II) complex a Ni-Fe complex was achieved that had diatomic ligand stretching frequencies almost identical to that of the reduced form of the [NiFe]-H_2ase enzyme. As shown in Figure I-14, the thioether sulfur to iron bond was retained, and because of the large bite angle of the pentanedithiolate, the $Ni(\mu\text{-}S)_2Fe$ core is diamond-shaped, nearly flat rhombus with Ni---Fe distance of 3.30Å.[90]

The Rauchfuss group has protonated the Schroeder-type Ni^IFe^I complex of Figure I-14, to yield a $(\mu\text{-}H)(\mu\text{-pdt})Ni^{II}Fe^{II}$ complex, Figure I-15.[96] Likewise a bridging hydride was

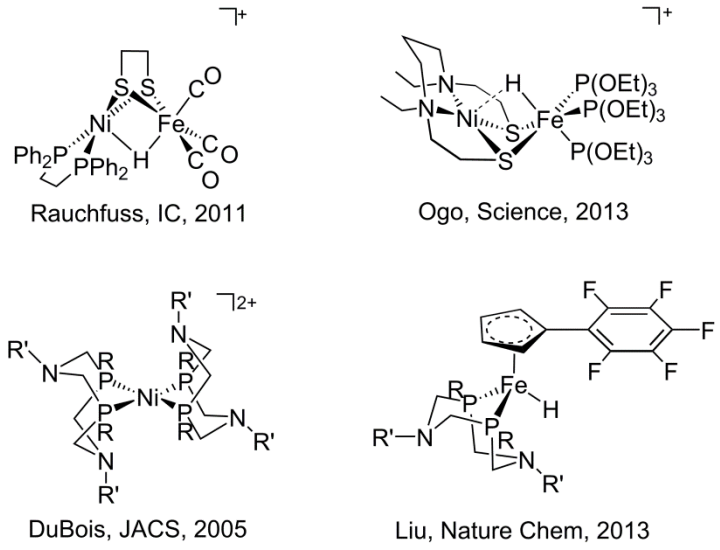

Figure I-15. Functional biomimetics of the [NiFe]-H_2ase active site.

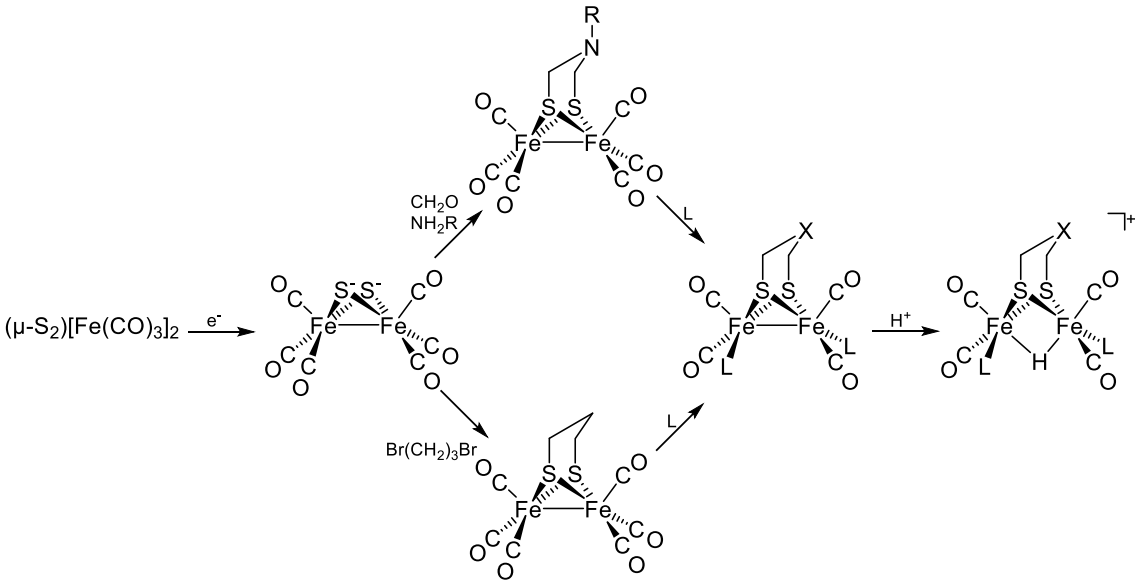

Figure I-16. Common synthetic route to biomimetics of the [FeFe]-H_2ase active site.[105]

reported by Ogo, *et al*., as a functional mimic that catalyzes electron and hydride transfer from dihydrogen.[97] In this case the iron has phosphite ligands replacing the diatomics of the active site. The DuBois catalyst, Figure I-15, was designed to contain several of the functional features of the active sites of both [NiFe]- and [FeFe]-H_2ase, by making nickel the catalytic metal, held in a flexible P_4 donor environment.[98-100] The pendent base nitrogen within a 6-membered NiP_2C_2N cyclohexane type metallocycles facilitate heterolytic H_2 cleavage or formation. The built-in pendent base that serves as a proton relay has been further used in an iron complex, developed by Liu, *et al*., that is a solution electrocatalyst for the oxidation of hydrogen at a low overpotential.[101]

Models of the [FeFe]-Hydrogenase Active Site

The prototypical [FeFe]-H_2ase model complex is $(\mu\text{-SR})_2[Fe^I(CO)_3]_2$, first described by Reihlen in the late 1920s.[102] This complex and the μ-SRS, bridging bidentate dithiolate analogue, may be prepared by oxidative addition of thiols to iron(0) carbonyls, or via the route shown in Figure I-16. The bridging persulfide iron carbonyl, $(\mu\text{-S}_2)[Fe^I(CO)_3]_2$, is arguably of primordial significance;[103] it is as well a prominent molecule in the historical development of Hieber's organoiron carbonyl chemistry.[104] The Fe^IFe^I organometallic, rendered diamagnetic by the metal-metal bond between two d^7 Fe^I atoms at ca. 2.6 Å, is a readily available precursor for both electrophilic addition of alkyl halides to the reduced persulfide ligand, or the condensation of aldehydes and amines that leads to the bridgehead amine complexes, of obvious closer analogy to the [FeFe]-H_2ase active site.[105]

Also shown in Figure I-16 are the CO substitution reactions that typically proceed in bimolecular, thermal processes thus adding ligands such as cyanide, phosphines, N-heterocyclic carbenes and various N-donors. Sequential additions of monodentate ligands proceed with substitutions on alternate iron atoms. This is the observation with cyanide, readily producing the dicyano complex $(\mu\text{-pdt})[Fe(CO)_2(CN)]_2^{2-}$.[106] This complex is remarkably similar to the active site. A single additional replacement of one carbonyl ligand with a 4Fe4S cluster is needed to yield a composition identical to the active site. Unfortunately, the dicyano model complex is inert to further substitution. The cyanide derivatives are also incompatible with electrochemical proton reduction as the cyanide N is readily protonated, leading to decomposition. Hence phosphines are used as good

electron donor surrogates, resulting in many successes in the form (μ-pdt)[$Fe^{I}(CO)_2(PR_3)]_2$ that mimic some expected properties of the [FeFe]-H_2ase active site.[107,108]

Other complexes with strong σ-donating ligands have been utilized in models, especially N-heterocyclic carbenes.[109,110] Nitrogen donor ligands such as pyridine and imidazole lack stability and only a few model complexes include them. Isonitrile ligands appear promising, as they should permit modifications of their steric and electronic properties. However, unlike cyanide, early studies found that isonitrile does not halt at the disubstituted product, but rather continues carbonyl substitution beyond what is desired.[111,112] Multiple substitutions can also occur for PMe_3 under stringent, forcing conditions[113] and the vinyldiphosphine ligand has been highly useful as a scaffold bidentate ligand to promote "rotated" structures with an open site on one iron.[114]

In addition to the propane dithiolate and the azadimethanethiolate as bridging bidentate ligand, other bridgehead modifications extend the list of diiron complexes. The condensation of formaldehyde and primary amines on a $(\mu\text{-}SH)_2[Fe(CO)_3]_2$ scaffold can introduce a variety of amines in the bridgehead position making this a very useful functionality for subsequent immobilization on solid supports or electrode surfaces.[115,116] It has also been used for cyclodextrin inclusion adducts.[117,118] If the amine is excluded in the formaldehyde condensation process, etherdimethanethiolate is obtained.[96] Song and coworkers have improved the synthesis of the etherdimethanethiolate[119] and expanded the field with the first reported thioetherdimethanethiolate.[120]

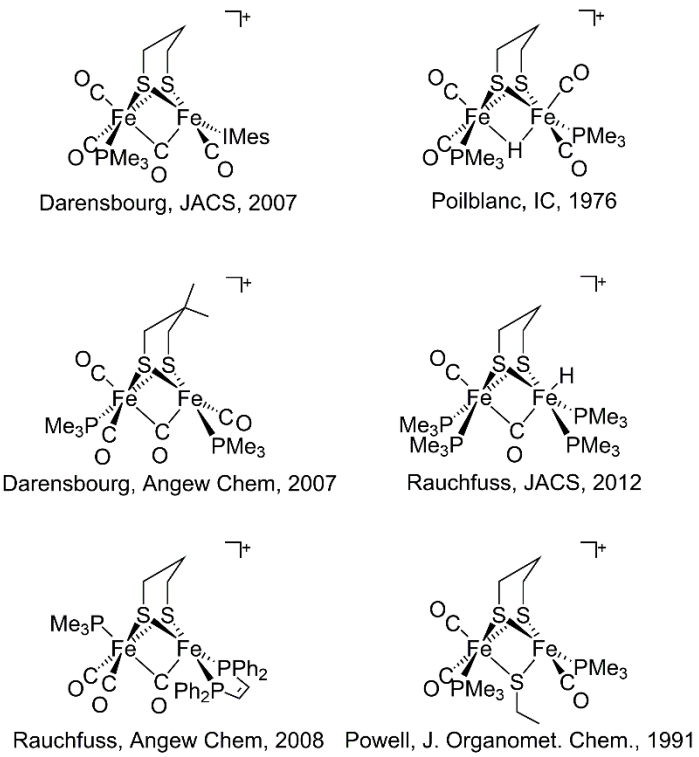

Figure I-17. Biomimetics of the[FeFe]-H_2ase active site in oxidized form: $Fe^{2+}Fe^{1+}$ (left) and $Fe^{2+}Fe^{2+}$ (right).

The requirement of good donor ligands lies in enhancing the pK_b of the iron site for proton uptake and stabilization of higher oxidation states as are needed through the enzyme's catalytic cycle, Figure I-10. Mimics of the diiron complexes in higher oxidation states are shown in Figure I-17 The right column shows structures of protonated (μ-pdt)$[Fe^{I}(CO)_2(PMe_3)]_2$ and (μ-pdt)$[Fe^{I}(CO)(PMe_3)_2]_2$ yielding a thermodynamically favored bridging hydride, $Fe^{II}(\mu\text{-}H)Fe^{II}$,[121] and a terminal hydride, $Fe^{II}(\mu\text{-}CO)Fe^{II}\text{-}H$,[113] respectively, both in the redox level of $Fe^{II}Fe^{II}$. The terminal hydride is the expected configuration of the hydride species in the [FeFe]-H_2ase catalytic cycle.[113]

As the open site on iron is a prominent feature of the [FeFe]-H_2ase active site, and an elusive geometrical isomer of the parent model, considerable effort has targeted such structural analogues.[122] While the crystal structures of various (μ-SRS)[$Fe^I(CO)_3$]$_2$ complexes universally share an edge-bridged square pyramidal geometry, solution ^{13}C NMR spectral studies established axial/basal site equilibration of the individual sets of three carbonyls at room temperature, but axial/basal site differentiation, as in the solid state structures, at low temperatures. Computational investigation identified a transition state that is the square pyramid – inverted square pyramid geometry as is seen in the active site, Figure I-18. Such a structure is a geometrical isomer of the ground state S-bridged square pyramids in the butterfly form of the parent models, (μ-SRS)[$Fe^I(CO)_3$]$_2$ complexes. Stabilization of this transition state relative to the ground state of the complex would require diminishing the Fe—Fe bond order, by removal of an electron, and inclusion of steric hindrance. The exact combination of steric hindrance that leads to reversible one-electron oxidation processes has been reached by accident or by design in less than 10 cases, three of which are displayed in Figure I-17, left column. Steric hindrance at the bridgehead carbon of dimethyl- or diethyl- propanedithiolate, in combination with the PMe_3 ligands, achieve the rotated isomer in the $Fe^{II}Fe^I$ redox level.[59] Steric hindrance from the ligands, the vinyldiphosphine or the dimesityl-NHC, also facilitates these rare isomeric forms.[32,58] The impressive change that occurs in the diiron complex with bridging propanedithiolate is emphasized in Figure I-18 where the

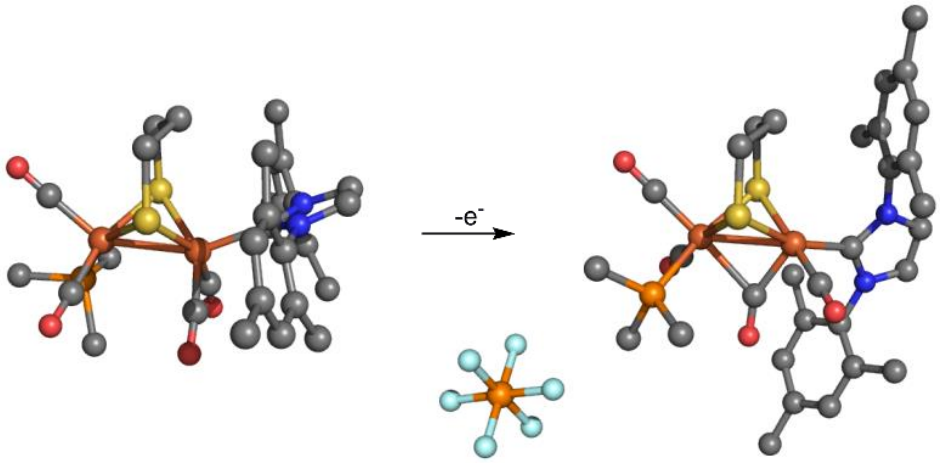

Figure I-18. Rotation of [FeFe]-H_2ase model into an isomer with a bridging carbonyl is initiated by oxidation of a complex with sterically bulky, strong σ-donor ligands.[109]

substituent donor ligands are PMe_3 and the IMes ligand. On one electron oxidation the huge IMes-NHC shifts from apical to basal positon as a CO shifts from terminal to bridging, opening up an open face on iron that is underneath the bridgehead CH_2 of the boat form of the FeS_2C_3 6-membered ring.[32] Clearly bridgehead steric bulk, provided in the protein by the surrounding peptide chain, is capable of maintaining the rotated structure even in reduced, Fe^IFe^I forms of the active site. In fact, the diethylpropane dithiolate form of (μ-SRS)[$Fe^I(CO)_2PMe_3]_2$ is substantially rotated in the solid state.

Clearly the accessibility of a versatile precursor has led to a vast array, in fact, hundreds of synthetic analogues of the [FeFe]-H_2ase active site as have been already published. Some of them are electrocatalysts for proton reduction, the best being the benzene dithiolate diiron hexacarbonyl complex extensively explored by Evans, Glass *et al*.[58] Some have multiple features that relate to individual components of the active site. The only complete H_{ox} cluster mimic is the unique and fragile structure from the Pickett laboratory that has a 4Fe4S cluster connected to the diiron carbonyl core by a thiolate sulfur, Figure I-19.[39] The redox active iron-sulfur cluster is represented by a ferrocenyl group on a phosphine ligand in elaborate construct from the Rauchfuss group, Figure I-19.[40] This prize complex also contains the pendent N-bridgehead base, a diphosphine ligand to mimic the cyanides as donor ligands for the active site, and it is isolated in a

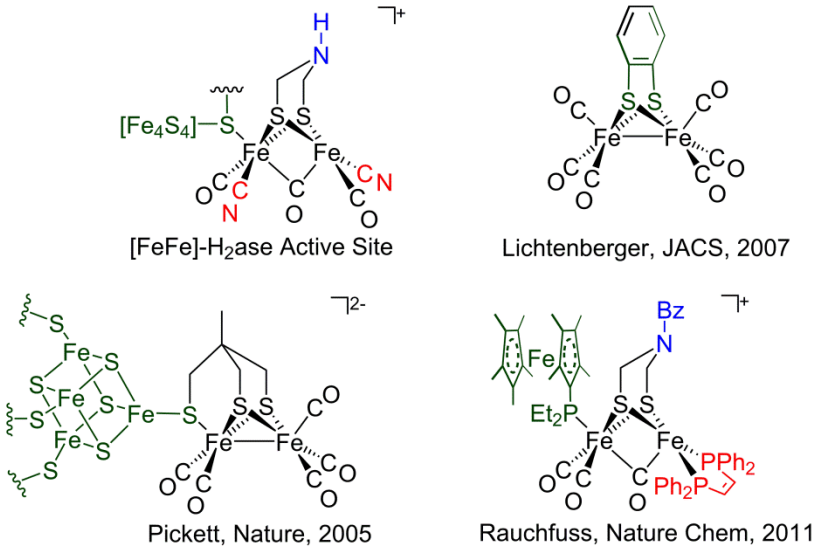

Figure I-19. [FeFe]-H_2ase active site and biomimetics displaying structural and functional similarities.

mixed-valent $Fe^{I}Fe^{II}$ state that is in the "rotated" structural form seen in the enzyme. This complex is active as a H_2 uptake catalyst, rapidly extracting electrons.[40]

Models of the [Fe]-Hydrogenase Active Site

Early model complexes of the [Fe]-H_2ase active site, as with the [NiFe]-H_2ase, were hindered by a lack of structural information. It was known that the enzyme contained a single iron atom, and by its EPR silence the oxidation state could be narrowed down to Fe^0 or Fe^{2+}. Mössbauer spectroscopy confirmed the latter.[150] The combination of FTIR and EXAFS spectroscopies informed organometallic chemists of sulfur ligation as well as

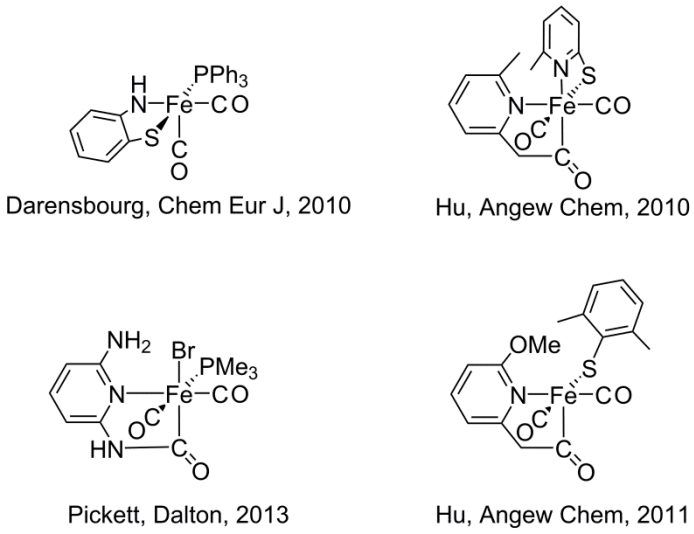

Figure I-20. Biomimetics of the [Fe]-H2ase active site.

the presence of two *cis* carbonyl ligands with apparent unsaturation about the iron.[79] Even with the structure of the light-inactivated cofactor, and the addition of a pyridine ligand, the composite active site structure revealed by Shima *et al*. in 2009 had one more surprise, an acyl ligand *trans* to the open site.[14] The difficulty in stabilizing a five-coordinate square pyramidal Fe^{2+} species was addressed by Liu, *et al*. through the reactivity of $Fe(CO)_3(PR_3)(I)_2$ with the redox non-innocent 2-aminothiophenol (ATP) ligand.[123] The structures of the resulting species revealed that the five-coordinate iron geometry ranged from mixed trigonal bipyramid / square pyramid to near-perfect square pyramid, Figure I-20. However, the non-innocence of the ATP ligand calls into question the oxidation state of the metal. Through a combination of X-ray crystallography, Mössbauer spectroscopy, and density functional theory calculations, it was suggested that the electron density could be more accurately described as an Fe^{1+} antiferromagnetically coupled to an ATP radical. Protonation of the amine decreases the electron density on the metal, leaving the Fe^{2+} more reactive and prompting acid-dependent CO uptake.[123]

A major focus of organometallic chemists has been the acylmethylpyridinyl unit. Hu and coworkers synthesized a model of the [Fe]-H_2ase active site with this bidentate ligand from addition of $Fe(CO)_5$ to a methylpyridinyl radical generated *in situ*.[124] This reaction, similar to the Fischer synthesis of metal-acyl species, yields an $[Fe^0(CO)_4C(=O)R]^-$ complex that binds the pyridinyl nitrogen upon oxidation. A similar carbamoyl unit can be assembled by internal nucleophilic amine attack on Fe^{II}-bound CO[125,126] Initially, this complex was isolated as a six-coordinate iron with the addition of the N,S-ligand:6-methyl-2-mercaptopyridine, Figure I-20. A semi-stable five-coordinate species was

synthesized utilizing a sterically bulky thiolate.[124] This species is a distorted square pyramid, in which the acyl group is *trans* to the open site, as in the protein. The geometrical similarity to the active site is continued with the two *cis* carbonyl ligands, one *trans* to the thiolate, the other *trans* to the pyridine. The H/D exchange of H_2 and D_2 has been observed with this complex as a catalyst. Unfortunately, the sensitivity of the active site is also well-modeled by this complex, with decomposition in solution that is accelerated by light.

Comments and Conclusion

As a final section in this short summary of the organometallic chemistry that is displayed in hydrogenase enzyme active sites, I will focus on a few of the recent literature reports. Electrochemical studies of oxygen tolerant hydrogenase enzymes making use of protein film voltammetry lead to conclusions regarding the importance of rapid repair and reactivation processes that are essential to utilizing hydrogenases as practical technological catalysts where the complete exclusion of adventitious oxygen would be a serious challenge.[127]

Modifications continue to proliferate in the [FeFe]-H_2ase active site models; they are applied towards water solubility,[128] spectroscopic probes,[129] light-harvesting modules,[130,131] and proton delivery units.[132] Progress has also been made in immobilization of the [FeFe] organometallic models in polymers,[133,134] dendrimers,[135] and metal-organic frameworks (MOFs).[136] Efforts to reduce over-potential of proton

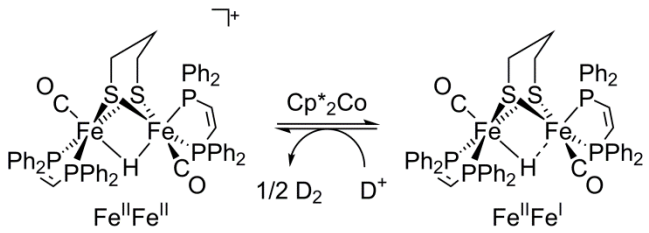

Figure I-21. The "spectator hydride" bridging between the two iron atoms does not participate in the H_2 production cycle.[141]

reduction and to understand factors that improve turnover numbers are also continuing in electrocatalytic studies of the models.[137,138] More accurate models of the [NiFe]-H_2ase active site that use cyanides as ligands to iron carbonyls have been developed wherein the highly reactive cyanide nitrogen is masked by forming arylborane Lewis acid adducts.[139]

Protonation studies of reduced [NiFe]- and [FeFe]-H_2ase synthetic analogues relevant to the enzymes' catalytic mechanisms explore the role of stable thiols (S-protonation)[140] or hydrides (Fe-protonation),[141] respectively. The latter is an elegant example of a "spectator" bridging hydride, permitting proton-reduction catalysis at a biologically relevant oxidation state level, and demonstrating that the initial hydride, a bridging hydride, Figure I-21, is not involved in subsequent chemistry.

The roles of models in bioinorganic chemistry have long been oriented towards providing reference points for spectroscopy and for biochemical reactivity. In terms of catalysis, rarely do the models have more than a superficial connection to the evolutionarily perfected active sites of enzymes. However, in the case of the hydrogenases we see the possibility for a faithful reproduction of not only the spectroscopic features, but also the

chemical and catalytic reactivity in the form of an easily accessible synthetic analogue. In fact, in 2013 the landmark study mentioned above found the (μ-SCH_2XCH_2S)$[Fe(CO)_2CN]_2^{2-}$ "models' of the active site of [FeFe]-H_2ase may be inserted into the maturation process at a step immediately preceding the activation of the apo-[FeFe]-H_2ase.[91] For X = NH, the semi-synthetic enzyme displays full activity for H_2 production, and various spectroscopies indicate the thus formed H-cluster is indistinguishable from the natural enzyme, Figure I-22. This study used the protein to inform on the models, as models with X = O or CH_2 loaded into the apo-enzyme, but were inactive. New studies have shown that the incorporation of the model complexes into the maturase protein is unnecessary, with direct insertion of the model complex into the apo-hydrogenase yielding a fully functional semi-synthetic enzyme.[142]

This presents a challenge to organometallic chemists to not only define the final active site structures, but also to use the tenets, principles and characteristics of organometallic chemistry to identify other steps in biosynthetic pathways of the hydrogenase enzymes. In this dissertation, I have described the synthesis, reactivity, and characterization of the parent model complex, (μ-pdt)$[Fe(CO)_3]_2$, (pdt = propane-1,3-dithiolate), and derivatives in Chapter III. The unique regioselectivity of CO exchange reactions as governed by the choice of nucleophilic or electrophilic ligands provides insight into the interplay of electron density in the diiron core of the enzyme. In Chapter IV, I describe computational investigation of the intramolecular fluxional processes of a series of (μ-SRS)$[Fe(CO)_3]_2$ complexes as a part of a study that aimed to quantify the ease of generation of an open site on the iron, modeling the distal iron of the enzyme active site. Finally, Chapter V details

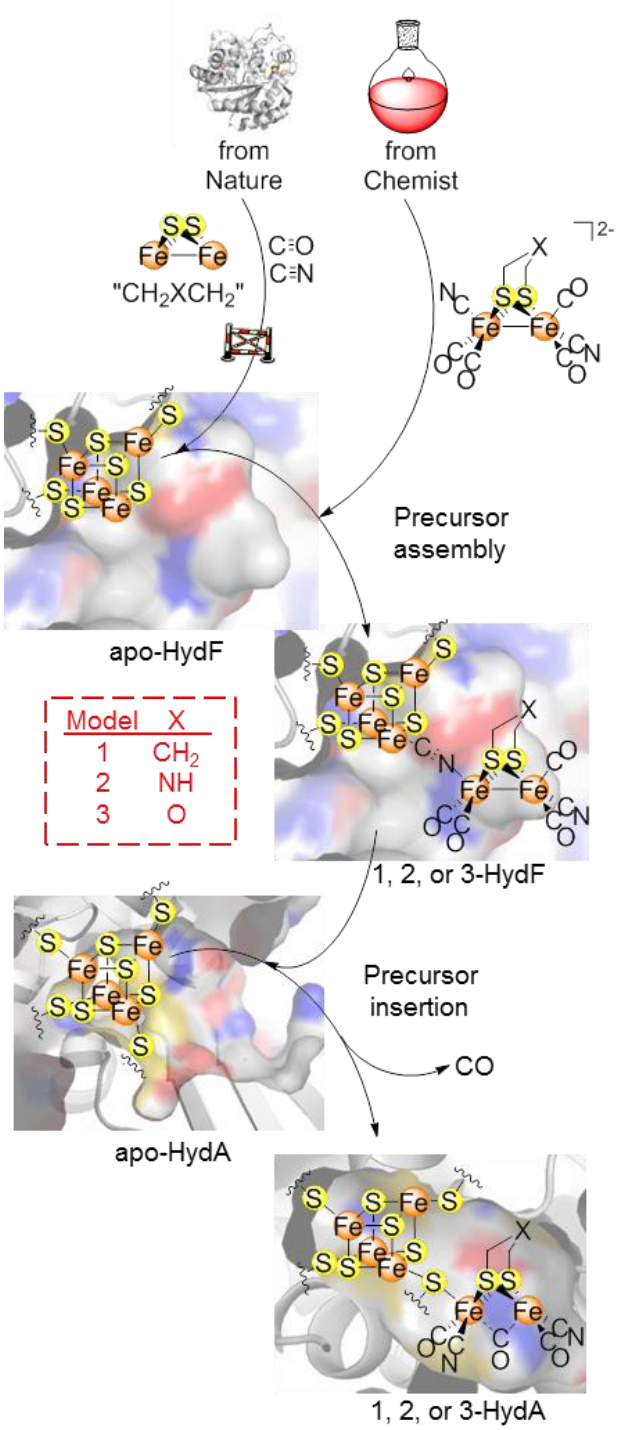

Figure I-22. Semi-synthetic production of [FeFe]-H_2ase from the insertion of an active site model complex into the apo-hydrogenase enzyme.[91]

my computational search for a plausible mechanism of ligand exchange and reduction of another organometallic compound, a dinitrosyl iron complex (DNIC). I identified two possible mechanisms that both involve the iron complex acting as a nucleophile towards a CO molecule, which then binds and promotes the reductive elimination of a thiyl radical. The role of organometallic chemistry in this dissertation has been to improve the knowledge of the selectivity, processes, and mechanisms of intermolecular and intramolecular ligand exchange as it relates to this new area in biological chemistry.

CHAPTER II

EXPERIMENTAL SECTION FOR CHAPTERS III - V

Procedures and Physical Methods for Chapter III

All reactions and operations were carried out on a double manifold Schlenk vacuum line, under an N_2 atmosphere and an Ar-filled glovebox was used in the manipulation and storage of air-sensitive compounds. All solvents were purchased as reagent grade and purified on an MBraun Manual Solvent Purification System, packed with Alcoa F200 activated alumina desiccant. The purified solvents were stored under an N_2 atmosphere prior to use. The N-heterocyclic carbenes, IMe = 1,3-dimethylimidazole-2-ylidene and IMes = 1,3-bis-(2,4,6-trimethylphenyl)imidazole-2-ylidene were obtained by deprotonation of the imidazolium salts (IMe^+I^- and $IMes^+Cl^-$ respectively), which were synthesized according to literature procedures.[143,144] The known complexes (μ-pdt)$[Fe(CO)_3]_2$ (pdt = 1,3-propanedithiolate),[145] **1**; (μ-pdt)$[Fe(CO)_2(IMe)][Fe(CO)_3]$,[146] **1-IMe**; (μ-pdt)][$Fe(CO)_2$(IMes)][$Fe(CO)_3$],[110] **1-IMes**; (μ-pdt)][$Fe(CO)_2$(IMe)][$Fe(CO)_2(PMe_3)$],[147] **5-IMe**; and (μ-pdt)][$Fe(CO)_2$(IMes)][$Fe(CO)_2(PMe_3)$],[109] **5-IMes** were prepared according to literature procedures. The following materials were purchased as reagent grade and used without further purification: trimethylphosphine, nitrosonium tetrafluoroborate, tetrabutylammonium cyanide, chloroform-*d*, methylene chloride-d_2.

Solution and solid-state infrared spectroscopy was carried out on a Bruker Tensor 27 FTIR spectrometer using a 0.1 mm CaF_2 sealed cell for all solution measurements. Solid state samples were measured using the Pike MIRacleTM attachment from Pike Technologies for Attenuated Total Reflectance (ATR) Infrared Spectra. Mass spectrometry (ESI-MS) was performed by the Laboratory for Biological Mass Spectrometry at Texas A&M University. Elemental analyses were performed by Atlantic Microlab, Inc., Norcross, Georgia, United States. Room temperature ^{1}H and ^{13}C NMR spectra were obtained using a Mercury 300 MHz NMR Spectrometer, ^{31}P NMR spectra were obtained using an Inova 300 MHz NMR Spectrometer. Variable temperature and low temperature ^{13}C NMR spectra were obtained by group member Danielle Crouthers on a Unity+ 500 MHz NMR instrument operating between 0 and 30 °C. Exchange of $^{12}CO/^{13}CO$ was monitored by *in situ* infrared spectroscopy by Samuel Kyran, using a Mettler Toledo iC10 ReactIR with an AgX fiber conduit probe having a SiComp ATR crystal.

X-ray data for all complexes was obtained by Chung-Hung Hsieh and Jason Denny at low temperature (110/150 K) on a Bruker Apex-II CCD based diffractometer (Texas A&M University) (Mo sealed X-ray tube, $K\alpha = 0.71073$ Å). A crystalline sample was coated in mineral oil, affixed to a Nylon loop, and placed under streaming N_2. The space groups were determined by systematic absences and intensity statistics, and structures solved by direct methods and refined by full-matrix least-squares on F^2. Anisotropic displacement parameters were employed for all non-hydrogen atoms; H atoms were placed at idealized positions and refined with fixed isotropic displacement parameters. The following programs were used: cell refinement, data collection, data reduction APEX2[148] absorption

correction SADABS[149] structure solutions, SHELXS-97[150] and structure refinement, SHELXL-97.[151]

Preparation of Compounds for Chapter III

*Synthesis of (μ-pdt)[Fe(CO)$_3$][Fe(IMe)(NO)(CO)]$^+$[BF$_4$]$^-$ (**2-IMe**) (first prepared by Dr. C.-H. Hsieh)*

Complex **2-IMe** was prepared from a solution of **1-IMe**, (μ-pdt)[Fe(CO)$_3$][Fe(CO)$_2$(IMe)], (0.440 g, 0.97 mmol), dissolved in 40 mL dichloromethane. This red solution was chilled to 0^{o}C in an ice water bath. A second solution of 0.110 g (0.97 mmol) NOBF$_4$ and 0.260 g (0.97 mmol) 18-crown-6 was prepared in 20 mL dichloromethane in an ice water bath at 0^{o}C. This pale yellow solution was magnetically stirred for up to 30 min. to allow for complete dissolution of the nitrosonium salt, at which time it was slowly added to the solution of **1-IMe**. The reaction was monitored by solution IR until formation of product ceased, after approximately 30 min. The resulting dark red solution was anaerobically filtered through Celite into a clean flask. Under N$_2$, the **2-IMe** product was isolated from unreacted starting material by repeated washes with hexanes and diethyl ether at 0 °C. Crystals of X-ray quality were obtained by layering a soluion of **2-IMe** in dichloromethane under diethyl ether at -5 ^{o}C. Yield: 0.25 g (52 %). IR (DCM) ν(CO): 2085(s), 2058(s), 2018(s); ν(NO): 1809(s). Anal. Calcd. for $C_{12}H_{14}BF_4Fe_2N_3O_5S_2$: C, 26.55; H, 2.60; N, 7.74. Found: C, 27.20; N, 3.11; H, 7.10. Mass Spec. Calcd. $C_{12}H_{14}Fe_2N_3O_5S_2$: 455.91. Found: 455.9185

*Synthesis of (μ-pdt)[Fe(CO)$_3$][Fe(IMes)(NO)(CO)]$^+$[BF$_4$]$^-$ (**2-IMes**)*

In a similar manner to **2-IMe** above, complex **2-IMes** was prepared from a solution of **1-IMes**, (μ-pdt)[Fe(CO)$_3$][Fe(CO)$_2$(IMes)], (0.200 g, 0.30 mmol), dissolved in 40 mL dichloromethane. This red solution was chilled to 0ºC in an ice water bath. A second solution of 0.035 g (0.30 mmol) $NOBF_4$ and 0.080 g (0.30 mmol) 18-crown-6 was prepared in 20 mL dichloromethane in an ice water bath at 0 ºC. This pale yellow solution was slowly added to the solution of **1-IMes** at 0 °C, and the reaction was monitored by solution IR until formation of product ceased, after approximately 30 min. The resulting dark red solution was filtered through Celite into a clean flask under an N_2 atmosphere. The product, **2-IMes**, was isolated from unreacted starting material anaerobically by repeated washes with hexanes. Crystals of X-ray quality were obtained by layering a solution of **2-IMes** in dichloromethane under a layer of hexanes, itself under a layer of diethyl ether at 0 ºC. Yield: 0.08 g (35 %). IR (DCM) ν(CO): 2085(s), 2039(m), 2025(m); ν(NO): 1792(m). Anal. Calcd. $C_{28}H_{30}BF_4Fe_2N_3O_5S_2$: C, 43.78; H, 4.03; N, 5.59. Found: C, 43.92; H, 4.10; N, 5.39. Mass Spec. Calcd. $C_{12}H_{14}Fe_2N_3O_5S_2$: 644.03. Found: 644.0249.

*Synthesis of (μ-pdt)[Fe(CO)$_3$][Fe(IMe)(NO)(CN)] (**3-IMe**) (first prepared by Dr. C.-H. Hsieh)*

Complex **3-IMe** was prepared from **2-IMe** (0.20 g, 0.34 mmol), dissolved in 30 mL tetrahydrofuran. This red solution was chilled to 0 ºC in an ice water bath, then transferred via cannula to a suspension of 0.047 g (0.30 mmol) $Et_4N^+CN^-$ in 10 mL of tetrahydrofuran

at 0ºC. The reaction was monitored by solution IR until formation of **3-IMe** ceased, after approximately 3 hours. The resulting light red solution was filtered through Celite into a clean flask under an N_2 atmosphere, removing any unreacted $Et_4N^+CN^-$. The product, **3-IMe**, was isolated from unreacted starting material by slow addition of diethyl ether, precipitating any remaining unreacted cyanide salts as well as any remaining starting material, **2-IMe**. This solution was washed with a 10:1 mixture of hexanes/ether to remove impurities until none were visible by IR spectroscopy in the diatomic ligand region (2200 – 1600 cm^{-1}). Crystals of X-ray quality were obtained by layering **3-IMe** in dichloromethane under a layer of hexanes, itself under a layer of diethyl ether at 0ºC. Yield: 0.050 g (38%). IR (DCM) ν(CN): 2112(vw); ν(CO): 2054(s), 1988(s); ν(NO): 1755(m). Mass Spec. Calcd. $C_{20}H_{34}Fe_2N_5O_4S_2$: 584.08. Found: 584.0794.

*Synthesis of (μ-pdt)[Fe(CO)$_3$][Fe(IMe)(NO)(PMe$_3$)]$^+$[BF$_4$]$^-$ (**4-IMe**)*

Complex **4-IMe** was prepared from a solution of **2-IMe** (0.20 g, 0.34 mmol) in 40 mL dichloromethane under N_2. The solution was chilled to 0 ºC in an ice water bath and 35 μL (0.34 mmol) PMe_3 was added via microsyringe. The reaction was monitored by IR, with complete conversion to the product in less than 15 minutes. The product, **4-IMe**, was filtered through Celite into a clean flask and washed several times with diethyl ether at 0 °C, maintaining an N_2 atmosphere throughout. Crystals of X-ray quality were obtained by layering **4-IMe** in dichloromethane under a layer of diethyl ether at 0 ºC. Yield: 0.15 g (69 %). IR (DCM) ν(CO): 2062(s), 1996(s); ν(NO): 1758(m). Anal. Calcd.

$C_{14}H_{25}BF_4Fe_2N_3O_5S_2P_1$: C, 27.37; H, 3.95; N, 6.90. Found: C, 27.61; H, 4.14; N, 6.90. Mass Spec. Calcd. $C_{14}H_{23}Fe_2N_4O_4S_2P_1$: 503.96. Found: 503.9367.

*Syntheses of (μ-pdt)(μ-CO)[Fe(IMe)(NO)][Fe(CO)$_2$(PMe$_3$)]$^+$[BF$_4$]$^-$ (**6-IMe**) and (μ-pdt)(μ-CO)[Fe(IMes)(NO)][Fe(CO)$_2$(PMe$_3$)]$^+$[BF$_4$]$^-$ (**6-IMes**)*

Complexes **6-IMe** and **6-IMes** were prepared from solutions of **5-IMe** (0.20 g, 0.37 mmol) and **5-IMes** (0.20 g, 0.28 mmol), respectively, dissolved in 40 mL dichloromethane. These red solutions were chilled to 0^{o}C in an ice water bath, then transferred via cannula to suspensions of 0.043 g (0.37 mmol) and 0.033 g (0.28 mmol) $NO^+BF_4^-$, respectively, in 40 mL dichloromethane at 0 ^{o}C. The reactions were monitored by solution IR until formation of product ceased, after approximately 3 hours for both reactions. A similarly colored reddish brown solution was obtained for both reactions. Each solution was filtered through Celite into a clean flask under an N_2 atmosphere and the products, **6-IMe** and **6-IMes**, were purified by repeated diethyl ether washes of the products until no starting material (**5-IMe** and **5-IMes** respectively) could be observed in the IR spectrum. Characterization of these complexes was limited to infrared spectroscopy, although crystals of X-ray quality were obtained by Dr. C.-H. Hsieh who prepared a solution **6-IMes** in dichloromethane under a layer diethyl ether at 0 ^{o}C. **6-IMe**: Yield: 0.05 g (20 %). IR (DCM) ν(CO): 2031(s), 1977(m); ν(NO): 1784(m). **6-IMes**: Yield: 0.05 g (20 %). IR (DCM) ν(CO): 2035(m), 1996(s); ν(NO): 1782(m).

*Preparation of ^{13}CO labelled **2-IMe***

Illuminating a solution 0.50 g (1.3 mmol) of complex **1**, dissolved in hexanes in a Pyrex flask, with a 275 W GE ultraviolet Sunlamp for five hours while sealed under a ^{13}CO atmosphere produced a sufficiently enriched source for ^{13}C NMR studies. This compound was filtered through a plug of silica gel and the uniformly ^{13}CO enriched **2-IMe** was synthesized by the methods described above. The selectively enriched **2-IMe** was produced by placing a sample of 0.10 g (0.24 mmols) **2-IMe** at 22 °C under an atmosphere of ^{13}CO for two hours. This reaction was performed in a 100mL flask, in ~10mL DCM leaving 90 mL (4.0 mmols) of headspace to be filled with $^{13}CO(g)$ at 1 atmosphere. Under N_2, the selectively enriched product was filtered through a plug of Celite and dried at 0 °C. In order to examine the relative CO exchange of the two $Fe(CO)_x$ moieties, aliquots were removed and flash-frozen under N_2 at the following time points: 0 minutes, 10 minutes, 20 minutes, 30 minutes, and 2 hours.

Computational Methodology for Chapter III

Geometry and frequency calculations were performed with the Gaussian 09[152] suite of programs in the gas-phase with the B3LYP functional[153-155] and the 6-311+G(d,p) basis set[156,157] on all atoms. Crystallographic coordinates were used as starting geometries for optimizations of the ground state structures. Optimizations of the isomeric forms of each complex used the ground state bond angles and distances of each ligand as starting positions. Transition state calculations of the $Fe(CO)_3$ rotor were located using the

quadratic synchronous transit approach (STQN) implemented by Schledel and coworkers,[158,159] in which initial guesses of the reactant, product, and transition state structures are made. Enthalpy and free energy corrections to the electronic energy of all stable geometries were calculated at 298.15 K by Gaussian, where all energies were obtained in hartrees and then converted to kilocalories per mole. All relative free energies were compared to the initial optimized structure based on the crystallographic coordinates. Ground state geometries had no imaginary vibrational modes, while transition states were located with a single imaginary mode. The Ampac Graphical User Interface (AGUI) program[160] was used to extract geometric data as well as infrared frequency and bending and stretching vector data.

Computational Methodology for Chapter IV

Geometry and frequency calculations were performed with the Gaussian 09[152] suite of programs in the gas-phase with the B3LYP,[153-155] MPW1PW91,[161] TPSSTPSS,[162] and ωB97x-D[163] functionals and the 6-311+G(d,p) basis set[156,157] on all atoms. Crystallographic coordinates were used for ground state geometries and utilized as starting geometries for optimizations. Transition state calculations of the $Fe(CO)_3$ rotor utilized starting geometry guesses from previous calculations. Transition states of the FeS_2C_2X chair/boat interconversion and the amine inversion were located through relaxed coordinate scans of the Fe(1)−Fe(2)−X (X = bridgehead atom) and Fe(1)−N−C angles, respectively. All geometries were located with the B3LYP functional, with subsequent

geometry optimizations of the other functionals using the B3LYP structure as an initial guess. Enthalpy and free energy corrections to the electronic energy of all stable geometries were calculated at 298.15 K by Gaussian, where all energies were obtained in hartrees and then converted to kilocalories per mole. To compare to the experimental results, $\Delta G^{\ddagger}$ was recalculated at the coalescence temperature of the corresponding VT NMR experiment. Ground state geometries had no imaginary vibrational modes, while transition states were located with a single imaginary mode. The Ampac Graphical User Interface (AGUI) program[160] was used to extract geometric data as well as infrared frequency and bending and stretching vector data.

Computational Methodology for Chapter V

Geometry optimizations and frequency calculations were performed with the Gaussian 09[152] suite of programs in the gas-phase utilizing the BP86 functional[164,165] with the 6-311+G(d,p) basis set,[156,157] as previously demonstrated to be a suitable combination that best describes the electronic and vibrational structure of dinitrosyl iron complexes.[166] Where possible, geometries were obtained from crystallographic coordinates and utilized as starting geometries for optimizations. Enthalpy and free energy corrections to the electronic energy of all stable geometries were calculated at 298.15 K, where all energies were obtained in hartrees, then converted to kilocalories per mole. These calculated complexes matched closely with the experimental data provided by X-ray crystallography as well as the ν(NO) and ν(CO) IR stretching modes. For computational efficiency, the

mesityl groups of the NHC and phenyl group of SPh were replaced by CH_3. All stable geometries had no imaginary vibrational modes, while transition states were located with a single imaginary mode. The Ampac Graphical User Interface (AGUI) program[160] was used to extract geometric data as well as infrared frequency and bending and stretching vector data.

CHAPTER III

REGIOSELECTIVITY IN LIGAND SUBSTITUTION REACTIONS GOVERNED BY NUCLEOPHILIC AND ELECTROPHILIC LIGAND PROPERTIES*

Introduction

The surprisingly simple iron carbonyl complex, (μ-pdt)[$Fe(CO)_3$]$_2$, pdt = -$S(CH_2)_3S$-, complex **1**,[145] has a broad range of physical and chemical properties that have provided understanding of the the natural diiron catalytic site that exists within diiron hydrogenase, [FeFe]-H_2ase, see Figure III-1, mature HydA for structure of the [FeFe]-H_2ase active site.[85] Although meager, its intrinsic activity as a solution electrocatalyst for proton reduction mimics the function of the enzyme, providing impetus for further development.[87] Modifications via the dithiolate bridging ligand and CO exchange have resulted in myriad, well-characterized diiron complexes.[14,79] Further adaptations including attachment into polymer supports,[133,134] inclusion into metal organic frameworks,[136] *etc*., have probed the potential for the diiron hexacarbonyl complex to be practical as a base metal molecular electrocatalyst replacement for platinum in solar or fuel cells.

*This chapter is to be submitted for review and publication with the authorship as follows: Ryan D. Bethel, Chung-Hung Hsieh, Jason A. Denny, Danielle J. Crouthers, Michael B. Hall, and Marcetta Y. Darensbourg.

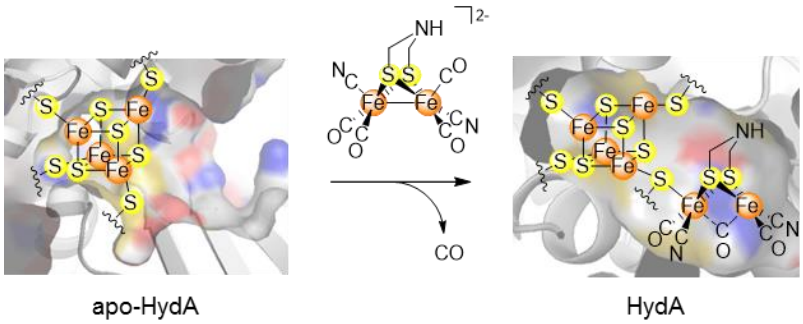

Figure III-1. The synthetic (μ-(adt)[Fe(CO)$_2$(CN)]$_2^{2-}$ may be inserted into the apo-[FeFe]H$_2$ase (apo-HydA, left) generating the fully functional enzyme (HydA, right).[142]

The utility of the (μ-adt)[Fe(CO)$_3$]$_2$, adt = -S(CH$_2$NHCH$_2$)S- or azadithiolate,[167] as a synthetic precursor to the diiron subsite as delivered to apo-[FeFe]-H$_2$ase has been demonstrated in recent studies that showed the dicyano derivative, (μ-adt)[Fe(CO)$_2$(CN)]$_2^{2-}$, when added to the apo-[FeFe]-H$_2$ase, lacking the 2Fe subsite, fully reconstitutes the enzyme in structure and achieves complete reactivity of the wild type enzyme, Figure III-1.[91,142] Hence the CN$^-$ substitution reactions of (μ-pdt)[Fe(CO)$_3$]$_2$,[104] explored over a decade ago for their mechanistic impact, become pertinent again as the full significance and possibility of even more organoiron units in biology is revealed through their presence in precursor proteins. In fact, as the [FeFe] site is incorporated into the mature HydA enzyme,[76,77] there is yet another substitution process when the 4Fe4S cluster displaces an additional CO. A broader question lies in nature's design of this collection of Fe, S, and diatomic ligands and its particular arrangement that undoubtedly

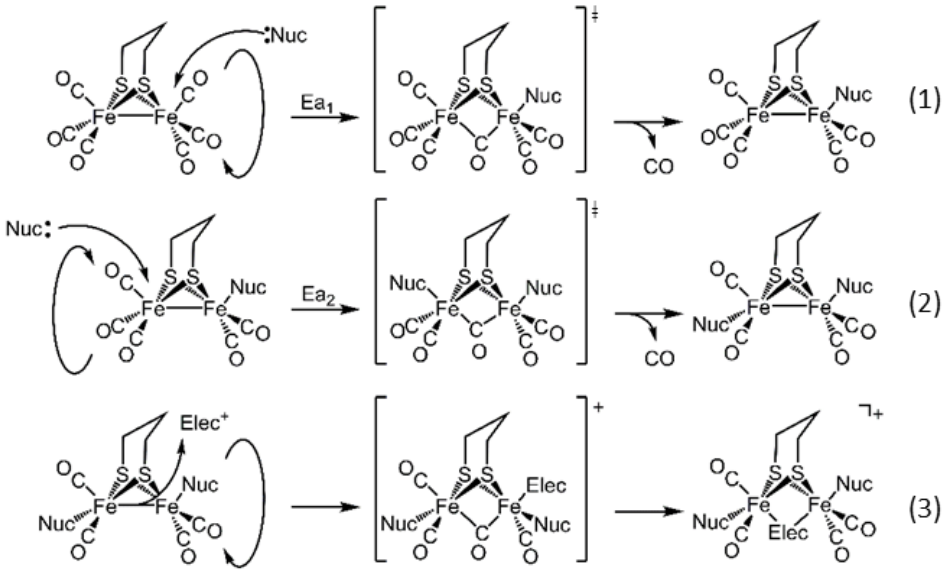

Figure III-2. The mechanisms of nucleophilic CO substitution (1 and 2), where $Ea_1 > Ea_2$ for CN^- and $Ea_1 < Ea_2$ for PMe_3,[106,169] and oxidative addition of electrophilic ligands such as H^+ and MeS^+ (3)[121,170]

involves electron density flow to and from the terminal iron site where hydrogen activity occurs.[168]

Equations 1 and 2 within Figure III-2 summarize nucleophilic substitution reactions which for CN^- and PMe_3 as entering ligands displace CO ligands on alternate irons.[106,169] The most common result of an electrophilic attack on the diiron complexes is the formation of the bridging $(\mu\text{-Elec})(\mu\text{-SRS})[Fe(CO)_2L]_2^+$, Elec = H^+ or SR^+, equation 3, Figure III-2.[121,170] However, the kinetic product of electrophilic attack, according to theory and corroborated by experiment, is a terminal Fe-H or Fe-SR (from H^+ and SR^+, respectively,

as electrophiles).[170,171] A less common site of electrophilic attack is the sulfur of the bridging thiolate. The formation of $[(\mu\text{-SRS(-Elec)})[Fe(CO)_2(L)]_2]^{n+}$ has been observed in the case of the electrophilic attack of Et^+ or O-atoms and has also been implicated as an intermediate step in the protonation of the Fe-Fe bond.[169,172]

Several studies have addressed the use of NO^+ as an electrophile that proceeds with isoelectronic CO exchange.[173-175] The strongly electron withdrawing NO^+ ligand is capable of significantly modifying the electronic environment of such complexes; additionally, the effect of nitrosylation on the structure of the diiron complex can be substantial. This is seen in the isomerization (a "rotation" or inversion of one $S_2Fe(PMe_3)(CO)(L)$ unit) of $(\mu\text{-dmpdt})[Fe^I(CO)_2(PMe_3)]_2$ upon NO^+/CO substitution, yielding a complex that is isostructural with the one-electron oxidized, mixed valent $(\mu\text{-dmpdt})(\mu\text{-CO})[Fe^I(CO)(PMe_3)][Fe^{II}(CO)_2(PMe_3)]^+$.[175] The electronic assignment in the rotated structure was supported by Mössbauer, EPR, and computational studies. As the NO analog was diamagnetic, it was concluded that the diiron core consisted of a spin-coupled d^7-Fe^I - NO· or $\{Fe(NO)\}^8$ by the Enemark-Feltham notation[176] and an Fe^{II}. Nevertheless, other possibilities exist for electronic assignment in such a $\{FeFe(NO)\}^{14}$ arrangement.

Hence it seemed appropriate to further investigate NO^+/CO exchange in $(\mu\text{-pdt})[Fe(CO)_3][Fe(CO)_2(NHC)]$ where NHC = N-heterocyclic carbene, a strong electron donor. Subsequent addition of nucleophiles, CN^- or PMe_3, should inform on the electronic distribution within the diiron organometallic. Thus we have investigated by synthesis,

structure, and computations. We will report that NO^+/CO exchange in (μ-pdt)[Fe(NHC)$(CO)_2$][Fe$(CO)_3$] occurs at the NHC substituted side and subsequent addition of CN^- or PMe_3 as nucleophiles results in the completely dissymmetric (μ-pdt)[Fe(NHC)(NO)(Nuc)][Fe$(CO)_3$]. Only with the doubly substituted (μ-pdt)[Fe$(CO)_2$(L)][Fe$(CO)_2$(L')] was a rotated structural isomer observed on reaction of NO^+, yielding (μ-pdt)(μ-CO)[Fe(L)(NO)][Fe$(CO)_2$(L')]$^+$, see Figure III-3.

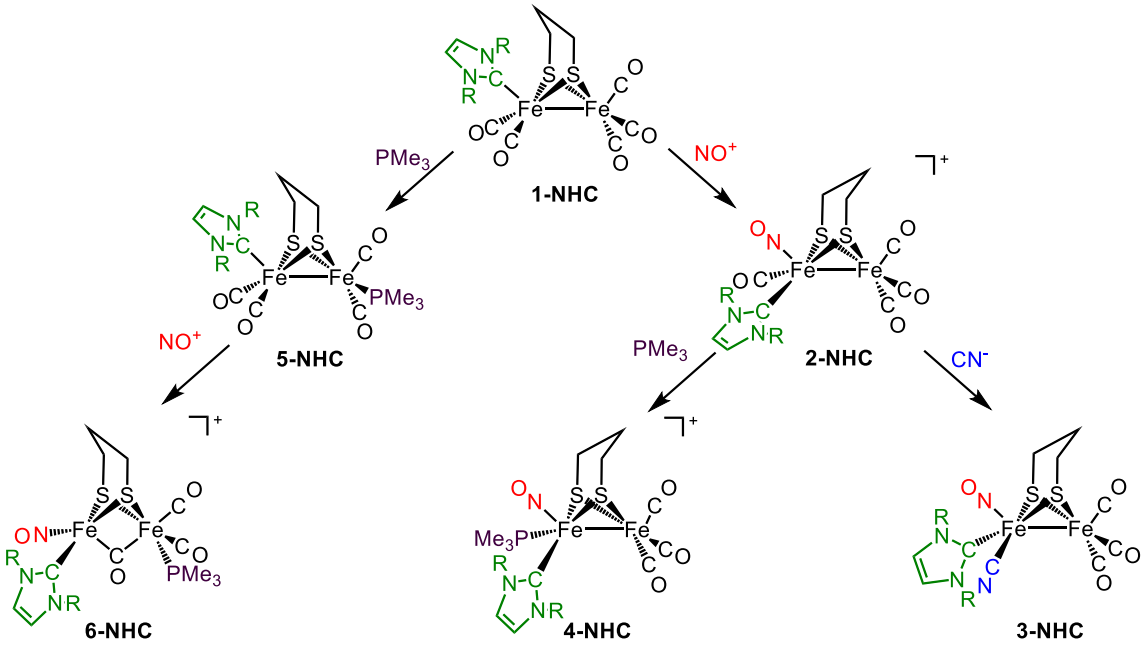

Figure III-3. Synthetic routes toward symmetric and dissymmetric (μ-pdt)[FeFe] complexes.

Results and Discussion

Synthetic Routes to Symmetric and Dissymmetric [FeFe]-H_2ase Model Complexes

The synthesis of (μ-pdt)[Fe(NHC)$(CO)_2$][Fe$(CO)_3$], **1-NHC**, where NHC = IMe, IMes, etc., from (μ-pdt)[Fe$(CO)_3]_2$ has been reliably established.[110,146] The well-characterized complexes **1-IMe** and **1-IMes** were chosen for the current study for their ease of purification as well as their stability. In addition, the IMe and IMes ligands have very similar donor properties with considerably different steric bulk. Figure III-3 outlines the derivatives of **1-NHC** that were obtained and characterized in this study. The stick drawings of products are in geometries established by X-ray diffraction analysis, *vida infra*.

The reaction of either **1-IMe** or **1-IMes** with PMe_3 yields the (μ-pdt)[Fe$(CO)_2$(IMe)][Fe$(CO)_2(PMe_3)$] (**5-IMe**) or (μ-pdt)[Fe$(CO)_2$(IMes)][Fe$(CO)_2(PMe_3)$] (**5-IMes**) complexes with, consistent with their well-known donor properties, nearly symmetric electron density on both irons.[109,147] The one-electron oxidation of **5-IMes** yields the "rotated" [FeFe]-H_2ase active site model complex (μ-pdt)(μ-CO)[Fe(CO)(IMes)][Fe$(CO)_2(PMe_3)]^+PF_6^-$ (**5-IMes$^+$**), containing a bridging carbonyl ligand and a terminal open site.[109] The isoelectronic ligand exchange of NO^+ for CO has been shown to act as a one-electron internal oxidant, as was observed with (μ-dmpdt)(μ-CO)[Fe(NO)(PMe_3)][Fe$(CO)_2(PMe_3)]^+BF_4^-$.[175] Upon NO^+/CO substitution of **5-IMe** or **5-IMes**, in DCM at 0 °C, a product, **6-IMe** or **6-IMes**, was isolated. The structure of **6-IMes** was determined by X-ray crystallography, *vide infra*, to

be "rotated", *i e.*, the (pdt)Fe(IMes)(CO)(NO) square pyramid is rotated by 180° from the neutral $Fe^{I}Fe^{I}$ isomer, such that the apical ligand, now the CO, is in a bridging position between the two iron atoms. Thus, **6-IMes**, (μ-pdt)(μ-CO)[Fe(NO)(IMes)][$Fe(CO)_2(PMe_3)$]$^{+}BF_4^{-}$, is isostructural with **5-IMes**$^{+}$, but with one CO replaced by an NO^{+}. As was seen with **5-IMe**$^{+}$, the use of the less bulky IMe ligand yields a product spectroscopically similar to its IMes substituted counterpart that is assigned to (μ-pdt)(μ-CO)[Fe(NO)(IMe)][$Fe(CO)_2(PMe_3)$]$^{+}BF_4^{-}$, **6-IMe**; however it has not yet been crystalized.

Synthesis of (μ-pdt)[Fe(IMe)(CO)(NO)][$Fe(CO)_3$]$^{+}BF_4^{-}$, ***2-IMe*** *and (μ-pdt)[Fe(IMes)(CO)(NO)][$Fe(CO)_3$]$^{+}BF_4^{-}$,* ***2-IMes***

The addition of the nitrosyl ligand to **1-IMe** or **1-IMes** was carried out at 0 °C to prevent the decomposition of the product, **2-IMe** or **2-IMes**. When the nitrosylated product is held at 22 °C for only a few minutes, it decomposes and additional infrared bands grow into the spectrum at ν(CO) 2055, 2017, and 1984 cm^{-1} and at ν(NO) 1780 and 1750 cm^{-1}. In addition, exposure to air results in the rapid decomposition of solutions of both **2-IMe** and **2-IMes**. The decomposition of **1-IMe** was found to be greatly reduced at low temperatures (~0°C) or by replacement of the inert atmosphere with CO(g). The degradation is also slower when the reaction is carried out in DCM. The $[NO]^{+}[BF_4]^{-}$ salt is all but insoluble in this solvent, which considerably impedes the reaction. Such heterogeneous conditions, even on a small scale (~0.10 g), may take hours to reach 50% completion, greatly increasing the byproducts and the need for purification, thereby

drastically reducing the yield. A helpful guide to chemical redox agents by Connelly and Geiger[177] notes that $[NO]^+[BF_4]^-$ is soluble in DCM in the presence of the cyclic ether, 18-crown-6.[178] With the aid of the crown ether, $[NO]^+[BF_4]^-$ fully dissolves in anhydrous DCM and reacts rapidly at 0 °C with **1-IMe** and **1-IMes**, yielding the pure product in minutes. The crown ether acts only to solubilize the NO^+, as the reaction goes to completion in less than an hour with a sub-stoichiometric amount (10 mol. %) of 18-crown-6. Both **2-IMe** and **2-IMes** are inert to further NO^+/CO exchange.

The addition of 20 equivalents of $NOBF_4$ to **2-IMe** does not result in additional nitrosylation, while maintaining a solution of the same compound under a blanket of CO for up to 72 hours does not show, by FTIR, any reformation of **1-IMe**. Both **2-IMe** and **2-IMes** may be stored as a solid powder under inert atmosphere for days at 0 °C without decomposition.

*Synthesis of (μ-pdt)[Fe(IMe)(CN)(NO)][Fe(CO)$_3$], **3-IMe** and (μ-pdt)[Fe(IMe)(PMe$_3$)(NO)][Fe(CO)$_3$]$^+BF_4^-$, **4-IMe***

The addition of cyanide or trimethylphosphine to **2-IMe** completes the synthetic cycle, and results in one fully substituted iron, while the other remains as an intact $[Fe(CO)_3]$ unit. The addition of CN^- takes place in THF at 0°C where the cyanide salt is sparingly soluble, and the reaction is slow. Although DCM may be used successfully to generate the product, (μ-pdt)[Fe(IMe)(CN)(NO)][Fe(CO)$_3$], **3-IMe**, the reaction in THF produces a cleaner IR spectrum, indicating a single product is present in high purity. The addition of PMe_3 to **2-IMe** takes place at 0°C in DCM. The reaction is complete within minutes,

with a nearly quantitative yield of the product, (μ-pdt)[Fe(IMe)(PMe_3)(NO)][Fe$(CO)_3]^+BF_4^-$, **4-IMe**. Addition of excess PMe_3 does not result in a second CO substitution at this temperature. In contrast to its precursor, **2-IMe**, and its analogue, **3-IMe**, this complex is relatively stable and may be handled under air and at ambient temperatures for several minutes without decomposition.

Table III-1. Experimental CH_2Cl_2 solution vibrational frequencies of diatomic ligands of relevant (μ-pdt)[FeFe] complexes.

Complexes	Vibrational Frequencies [a]
(μ-pdt)[Fe$(CO)_3]_2$, **1**	2072(m), 2037(s), 1990(s)
(μ-pdt)[Fe(IMe)$(CO)_2$][Fe$(CO)_3$], **1-IMe**	2035(m), 1971(s), 1952(m), 1915(m)
(μ-pdt)[Fe(IMes)$(CO)_2$][Fe$(CO)_3$], **1-IMes**	2035(m), 1969(s), 1947(w), 1916(w)
(μ-pdt)[Fe(IMe)(CO)(NO)][Fe$(CO)_3]^+BF_4^-$, **2-IMe**	2085(s), 2058(s), 2018(s), [1809(s)]
(μ-pdt)[Fe(IMes)(CO)(NO)][Fe$(CO)_3]^+BF_4^-$, **2-IMes**	2085(s), 2039(m), 2025(m), [1792(m)]
(μ-pdt)[Fe(IMe)(CN)(NO)][Fe$(CO)_3$], **3-IMe**	{2112(vw)}, 2054(s), 1988(s), [1755(m)]
(μ-pdt)[Fe(IMe)(PMe_3)(NO)][Fe$(CO)_3]^+BF_4^-$, **4-IMe**	2061(s), 1996(s), [1759(m)]
(μ-pdt)[Fe(IMe)$(CO)_2$][Fe$(CO)_2(PMe_3)]^-$, **5-IMe**	1974(s), 1934(s), 1898(m), 1884(sh)
(μ-pdt)[Fe(IMes)$(CO)_2$][Fe$(CO)_2(PMe_3)]^-$, **5-IMes**	1972(m), 1933(s), 1896(m), 1881(sh)
(μ-pdt)(μ-CO)[Fe(IMe)(CO)][Fe$(CO)_2(PMe_3)]^+PF_6^-$, **5-IMe**$^+$	2036(s), 2005(s), 1981(s), 1929(w)
(μ-pdt)(μ-CO)[Fe(IMes)(CO)][Fe$(CO)_2(PMe_3)]^+PF_6^-$, **5-IMes**$^+$	2036(s), 1997(s), 1987(sh), 1861(w)
(μ-pdt)(μ-CO) [Fe(IMe)(NO)][Fe$(CO)_2(PMe_3)]^+BF_4^-$, **6-IMe**	2031(s), 1977(m), [1784(m)]
(μ-pdt)(μ-CO) [Fe(IMes)(NO)][Fe$(CO)_2(PMe_3)]^+BF_4^-$, **6-IMes**	2035(m), 1990(s), [1782(m)]

[a]Values in brackets, [ ], and in braces, { }, are for ν(NO) and ν(CN), respectively.

Infrared Spectroscopy of Dissymmetric Complexes

The infrared stretching frequencies of the diatomic ligands of relevant (μ-pdt)[FeFe] complexes are presented in Table III-1 and displays of the diatomic region of the IR spectra of **1**, **1-IMe**, **2-IMe**, **3-IMe**, and **4-IMe** are presented in Figure III-4. As expected, the ν(CO) IR bands of **1** are shifted to lower frequencies on the substitution of a CO ligand by either of the good donor ligands IMe or IMes. Differences of the pattern and position of ν(CO) bands between the two NHC derivatives, **1-IMe** and **1-IMes**, are minor. The products resulting from addition of $[NO]^+[BF_4]^-$ have ν(CO) shifts at higher values with a dramatic change in the pattern of CO stretches, Figure III-4. In addition to the three ν(CO) bands, a ν(NO) band appears at 1809 cm^{-1}(**2-IMe**) and 1792 cm^{-1} (**2-IMe**). Unlike the minor differences in the spectra of **1-IMe** and **1-IMes**, the respective nitrosylated species are distinct. Although both **2-IMe** and **2-IMes** display an intense, sharp ν(CO) band at 2085 cm^{-1}, the other two carbonyl bands of **2-IMe** are equally intense with minimal overlap, being some 40 cm^{-1} separated at 2058 and 2018 cm^{-1}. In contrast, the two lower ν(CO) bands of **2-IMes** are less intense and overlap much more, with only 14 cm^{-1} separation at 2039 and 2025 cm^{-1}.

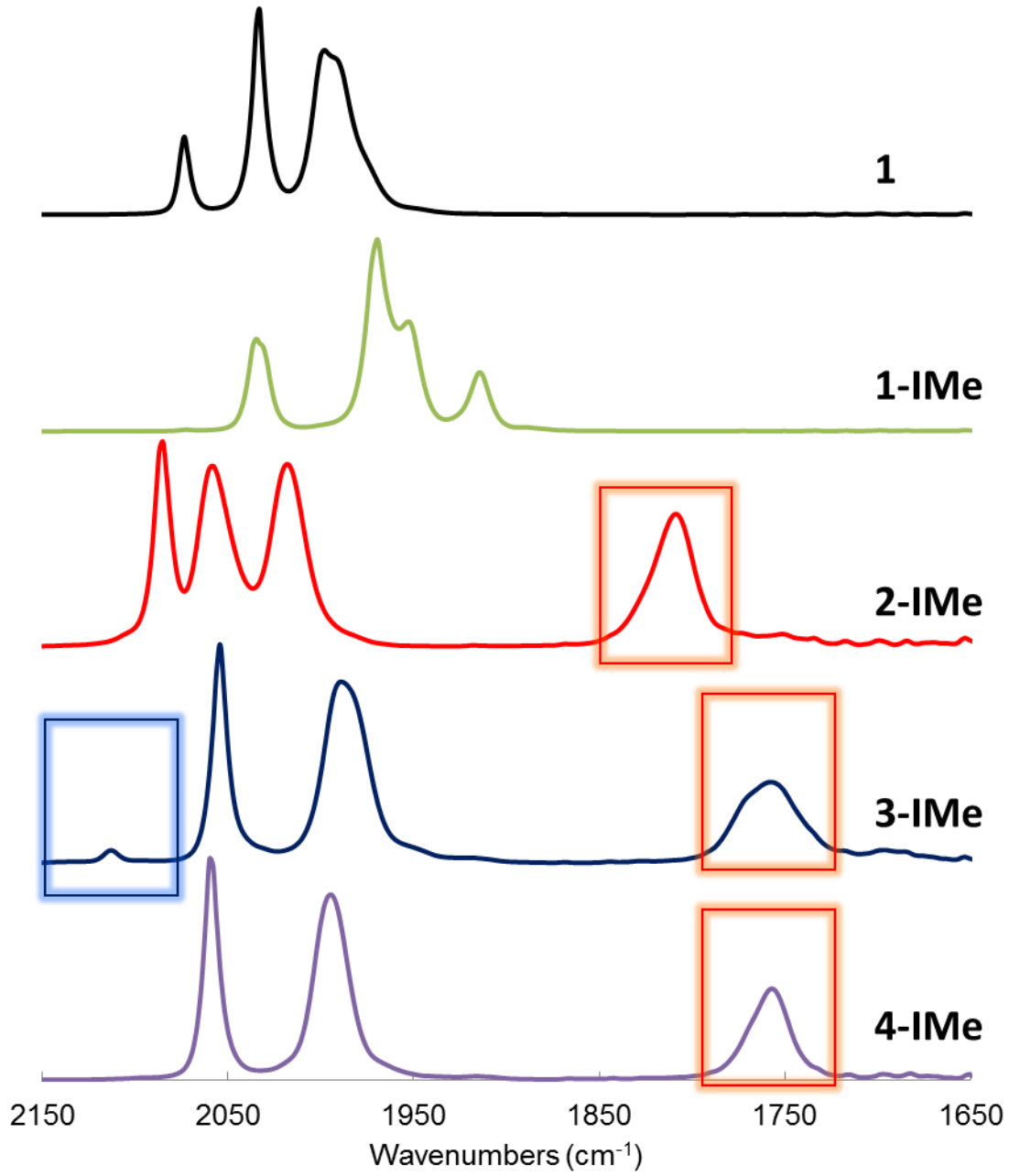

Figure III-4. Solution (CH_2Cl_2) IR spectra for complexes **1**, **1-IMe**, **2-IMe**, **3-IMe**, and **4-IMe** in diatomic ligand region. The CN band of **3-IMe** is marked with a blue box, the NO bands of **2-IMe**, **3-IMe**, and **4-IMe** are marked with red boxes.

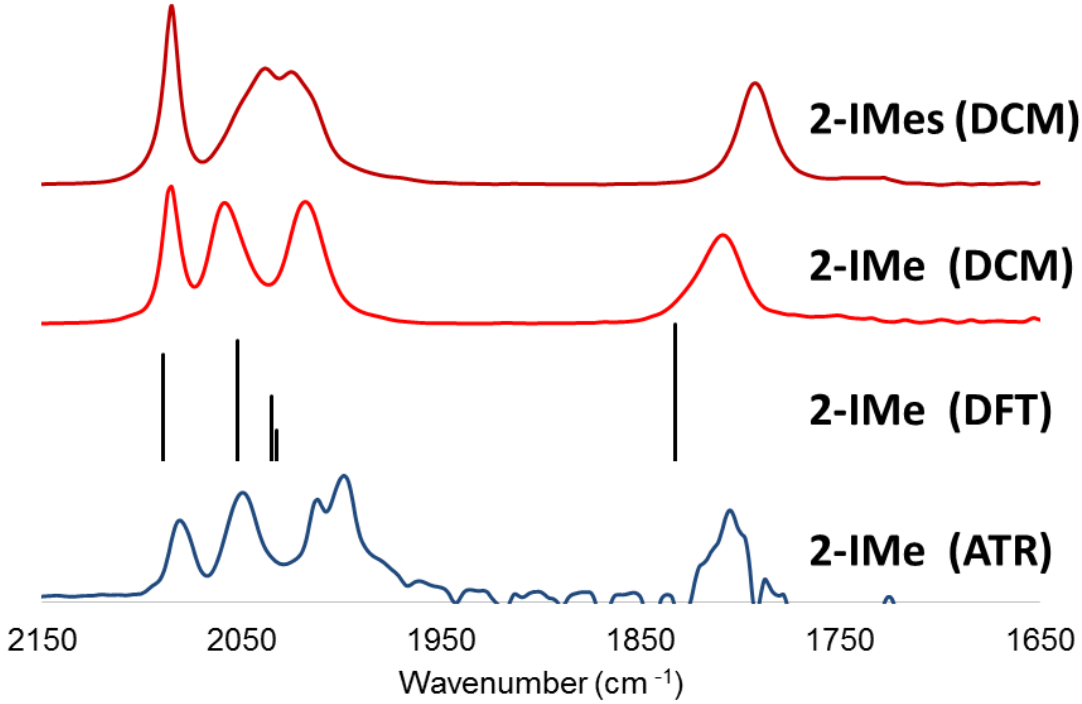

Figure III-5. Solution (CH_2Cl_2) IR spectra for complexes **2-IMes** and **2-IMe** in diatomic ligand region. The diatomic vibrational frequencies predicted using B3LYP/6-311+G(d,p) (scaling factor: 0.966) shows four ν(CO) bands as does the solid state (ATR) spectrum.

The infrared spectrum of **2-IMe** was poorly predicted by Density Functional Theory, utilizing both pure (BP86) and hybrid (B3LYP) functionals with a 6-311+G(d,p) basis set on all atoms. Accordingly, the ν(CO) band at 2085 cm^{-1}, Figure III-5, is assigned to the totally symmetric stretch of the $Fe(CO)_3$ unit with minor coupling to the CO of the other Fe(IMe)(CO)(NO) moiety. In the pseudo-C_{3v} $Fe(CO)_3$ moiety, this would be assigned as the A_1 band. The second band, at 2058 cm^{-1}, is primarily due to the lone CO, with minor coupling to the $Fe(CO)_3$. The third CO stretch in the solution IR spectrum at 2018 cm^{-1},

which would be the band assigned to the E stretching modes, consists of two overlapping bands in the molecule of overall C_1 symmetry. These bands also show minor coupling to the CO of the Fe(IMe)(CO)(NO) unit.

Addition of donor ligands, CN^- or PMe_3, to **2-IMe** results in a shift of ν(CO) and ν(NO) bands to lower frequencies. If cyanide is utilized, a new ν(CN) band appears at 2112 cm^{-1}, Figure III-4. The ν(CO) bands for this complex, **3-IMe**, shift to 2054 and 1988 cm^{-1}, taking on the two-band pattern characteristic of the C_{3v} structure seen, for example, in the piano stool complex $(\eta^5\text{-}C_5H_5)Fe(CO)_3^+$. This pattern is also seen in the ν(CO) bands of complex **4-IMe**, which contains a PMe_3 ligand rather than CN^-. The phosphine is not as strong an electron donor as cyanide, and the ν(CO) bands of the PMe_3-containing complex, **4-IMe**, are slightly higher in frequency, at 2061 and 1996 cm^{-1}. The ν(NO) band of **4-IMe** is also slightly higher than that of **3-IMe**, at 1759 and 1755 cm^{-1} respectively.

*Molecular Structures of **2-IMe**, **2-IMes**, **3-IMe**, **4-IMe**, and **6-IMes** from X-ray Crystallography*

Crystals of **2-IMe, 2-IMes, 3-IMe, 4-IMe,** and **6-IMes** were subjected to X-ray diffraction analysis and the structures obtained are shown in Figures III-6, III-7 and III-8, with relevant metric parameters shown in Table III-2. The crystals of **2-IMe**, **3-IMe**, and **6-IMes** were grown by Dr. Chung-Hung Hsieh. The structures of **2-IMe**, **3-IMe**, and **6-IMes** were solved by Dr. Chung-Hung Hsieh while the structures of **2-IMes** and **4-IMe** were solved with the assistance of Jason Denny. Of the four structures that display an intact $Fe(CO)_3$ moiety i.e., the $Fe_2(CO)_3$ moiety of three (**2-IMe, 3-IMe**, and **4-IMe**) is

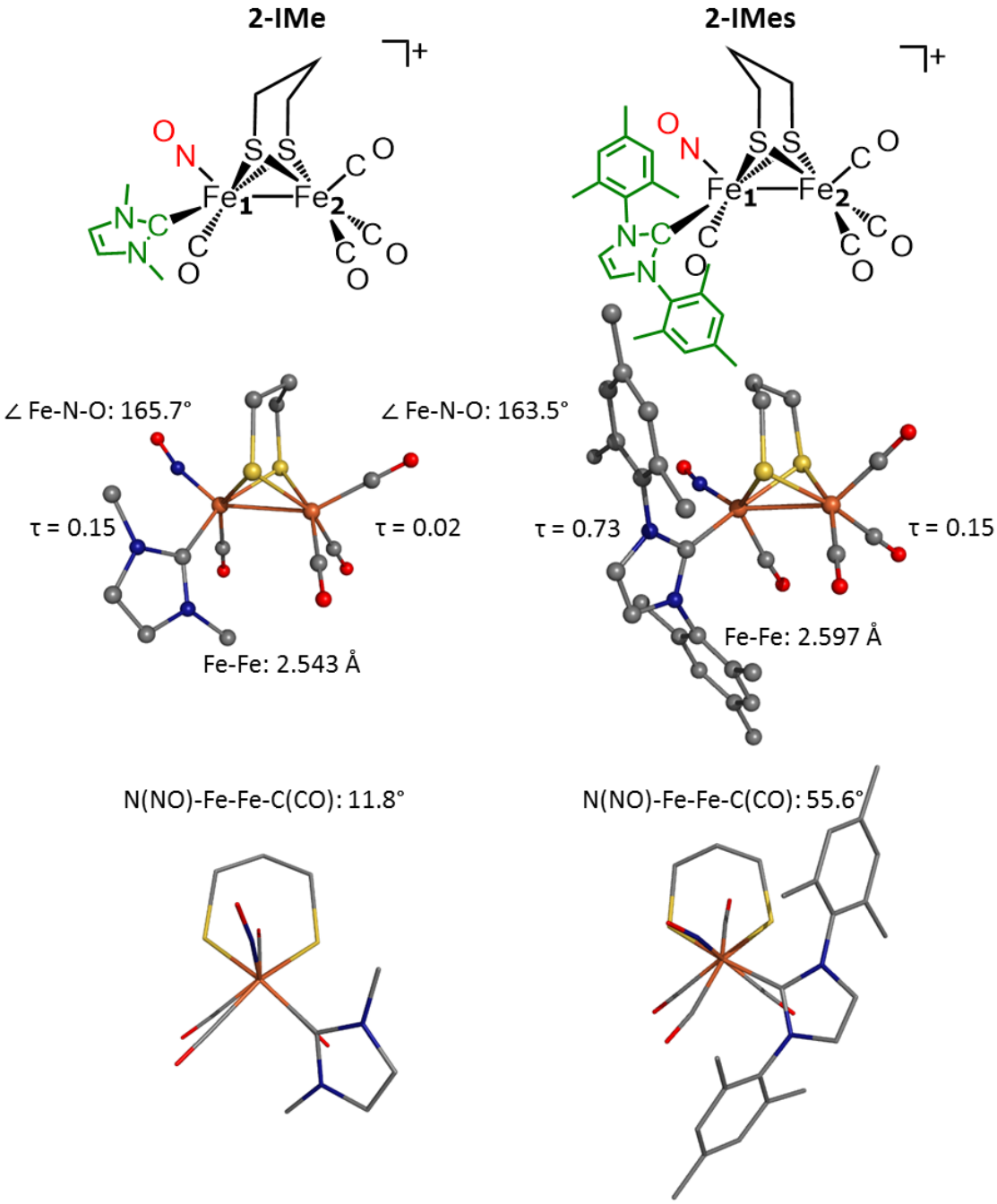

Figure III-6. Molecular structures of **2-IMe** and **2-IMes** from X-ray diffraction analysis with side view (top: ball-and-stick rendition) and end view (bottom: capped stick rendition). Hydrogen atoms and BF_4^- have been omitted for clarity.

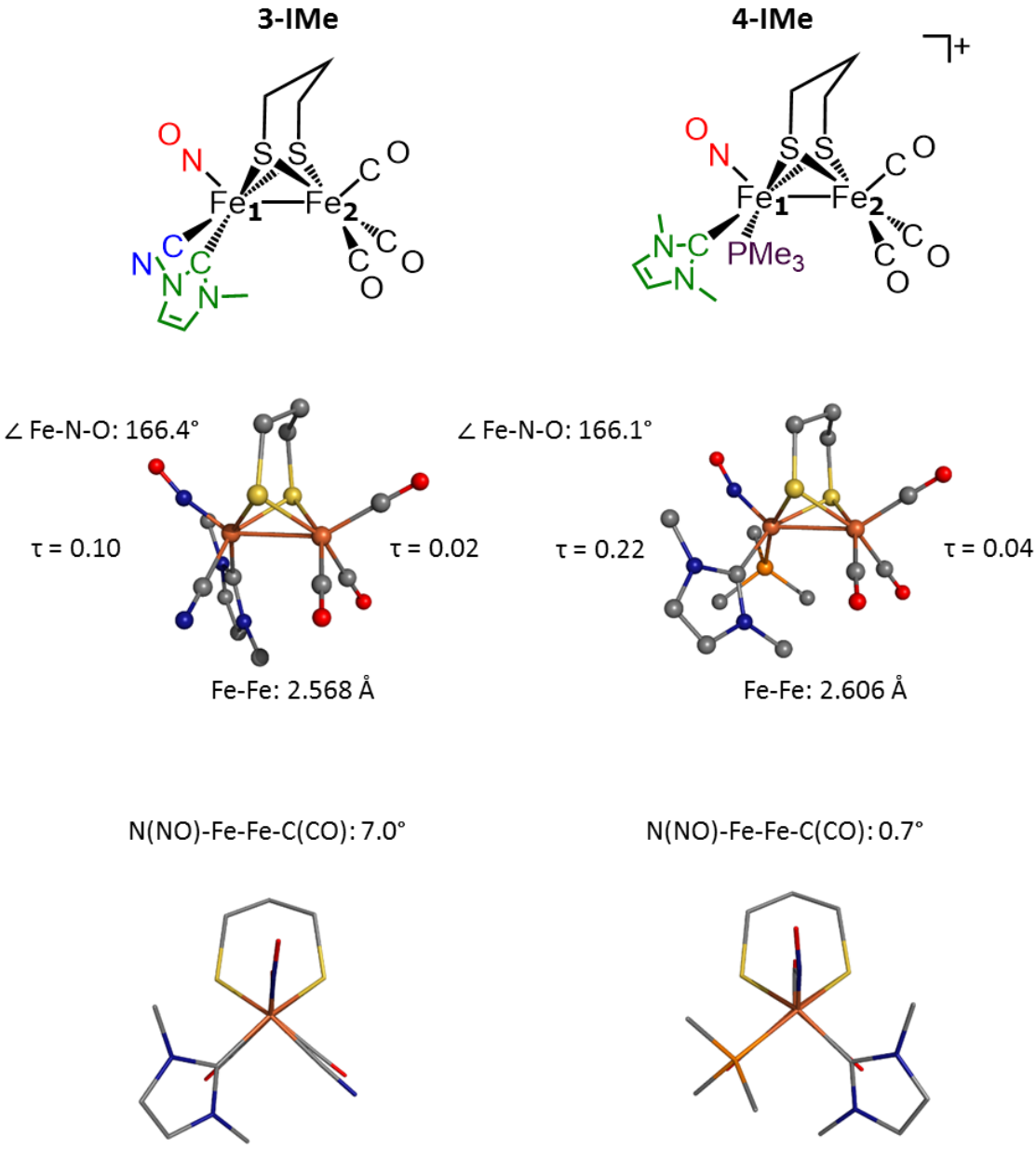

Figure III-7. Molecular structures of **3-IMe** and **4-IMe** from X-ray diffraction analysis with side view (top: ball-and-stick rendition) and end view (bottom: capped stick rendition). Hydrogen atoms and BF_4^- (**4-IMe**) have been omitted for clarity.

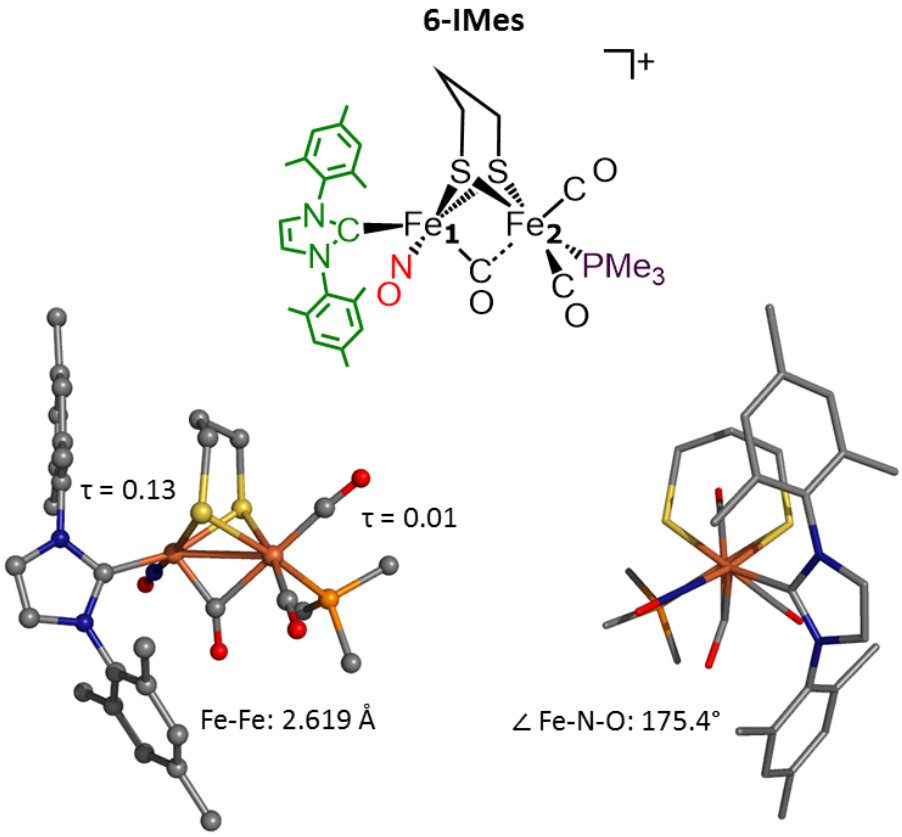

Figure III-8. Molecular structure of **6-IMes** from X-ray diffraction analysis with side view (left: ball-and-stick rendition) and end view (right: capped stick rendition). Hydrogen atoms and BF_4^- counterion have been omitted for clarity.

"under" the propanedithiolate bridgehead; *i.e.*, the boat conformation of the FeS_2C_3 ring is on the $Fe(CO)_3$ side of the diiron construct.

The substituted Fe, Fe_1, has an apical NO ligand within one $S_2Fe(NO)(NHC)(CO)$ square pyramid, slightly bent at $\angle Fe_1\text{-}N\text{-}O$ = 164-166° in all four structures. The basal ligands of Fe_1 include both the carbene, IMe or IMes, and the differentiating ligand: CO (**2-IMe** and **2-IMes**), CN (**3-IMe**), or PMe_3 (**4-IMe**). All four complexes display the typical edge-

Table III-2. Experimental structure metric parameters of compounds **2-IMe**, **3-IMe**, **4-IMe**, **2-IMes** and **6-IMes**.

	2-IMe	**3-IMe**	**4-IMe**[a]	**2-IMes**	**6-IMes**
$Fe_1 – Fe_2$	2.543(2)	2.568(2)	2.6059(5)	2.597(1)	2.619(2)
Fe_1 – C(NHC)	1.995(4)	2.017(4)	2.017(3)	2.033(5)	1.986(6)
Fe_1 – N(NO)	1.655(4)	1.672(4)	1.651(3)	1.662(5)	1.796(8)
Fe – S[b]	2.247	2.260	2.250	2.251	2.325
Fe_1 – C(CO)	1.846(5)	-	-	1.831(6)	1.986(6)
Fe_2 – C(CO)[b]	1.797	1.803	1.800	1.798	1.790
Fe_1 – C(CN)	-	1.955(6)	-	-	-
Fe – P(PMe3)	-	-	2.299(1)	-	2.275(2)
Fe_1 – N – O	165.7(3)	166.4(4)	166.1(3)	163.5(5)	175.4(6)
Fe_1 – C – O	177.9(4)	-	-	168.8(5)	136.1(4)
Fe_2 – C – O[b]	178.6	178.6	177.3	177.7	177.7
Fe – S – Fe[b]	69.4	69.14	70.77	70.45	68.56
S – Fe – S[b]	85.65	85.62	85.63	84.54	85.32
N – Fe – Fe – C	11.8(4)	7.0(4)	0.7(3)	55.6(4)	-
τ values[c]					
Fe_1	0.15	0.10	0.22	0.73	0.13
Fe_2	0.02	0.02	0.04	0.15	0.01
Fe displacement[d]					
Fe_1	0.448	0.470	0.396	-	0.217
Fe_2	0.348	0.383	0.347	0.259	0.145

[a]Values reported are average of 3 distinct molecules within the unit cell. Error is also averaged. [b]Average values reported. [c]reference 179 [d]Taken as distance of Fe from best square plane in each FeS_2L_3 square pyramid.

bridged bi-square pyramidal geometry of the (μ-SRS)[$Fe_2(CO)_x(L)_{6-x}$] family. The N_{ap}-Fe_1-Fe_2-C_{ap} dihedral angles of the three compounds bearing the IMe ligand are between 0.7 and 11.6°, while the analogous angle of **2-IMes** is much larger, at 55.6°. This difference in the structure of **2-IMes** may be attributed to the distortion of the Fe_1, from square pyramidal, its τ value is 0.73 (τ = 1 for trigonal bipyramid; τ = 0, square pyramid).[179,180] The other three structures are more regular square pyramids, with τ values ranging from 0.22 – 0.10. The unsubstituted iron, the $Fe_2(CO)_3$ moiety, of **2-IMe**, **3-IMe**, and **4-IMe** are nearly perfect square pyramids (τ = 0.04 – 0.02), again the **2-IMes** shows more distortion, τ = 0.15. The substituted Fe_1 is also seen to be pulled further out of the S_2L_2 plane, by up to 0.1 Å when compared to the Fe_2 for **2-IMe** (S_2L_2 iron displacements of Fe_1 = 0.448 and Fe_2 = 0.348 Å) and **3-IMe** (S_2L_2 iron displacements of Fe_1 = 0.470 and Fe_2 = 0.383 Å), although **4-IMe** shows less difference (S_2L_2 iron displacements of Fe_1 = 0.396 and Fe_2 = 0.347 Å). There is a subtle elongation of the Fe-Fe bond, from 2.543(2) and 2.568(2) Å for **2-IMe** and **3-IMe** to 2.597(1) and 2.6059(5) Å for **2-IMes** and **4-IMe**, which may be attributed to the steric effects of the larger IMes and PMe_3 ligands. Unlike the four structures above, the square pyramid of Fe_1 in the structure of **6-IMes** is rotated such that the carbonyl ligand bridges Fe_1 and Fe_2. This rotated structure, analogous to the structure of **5-IMes**$^+$, has an elongated Fe_1 – Fe_2 distance of 2.619(2) Å, with the μ-CO bent under the Fe_1 – Fe_2 vector at an ∠Fe_1-C-O of 136°. The NO ligand is in a basal position and the ∠Fe_1-N-O is 175.4(6)°, in contrast the apical NO of complexes **2-IMe**, **3-IMe**, **4-IMe**, and **2-IMes** with ∠Fe_1-N-O nearly 10° less.

*Regioselective ^{13}CO Subsitution of **2-IMe***

As noted above, the decomposition of **2-IMe** occurs in one to two hours at room temperature in non-coordinating solvent, DCM, and under inert atmosphere, N_2 or Ar. It was anticipated that the loss of CO, resulting from Fe – C(CO) bond cleavage by either thermal or hν-induced dissociation may be the initial step in the decomposition pathway. This was supported by the observation that a solution of **2-IMe** under a carbon monoxide atmosphere displayed little decomposition after 24 hours at room temperature. The CO dissociation is presumed to be thermal in nature, as decomposition ceases upon cooling the complex to 0 °C, under N_2 and ambient light, while at 22 °C, even in complete darkness, decomposition of **2-IMe** is observed within hours.

In order to test its CO lability, a solution of **2-IMe** in DCM was placed under a blanket of ^{13}CO. When this reaction mixture was held at 0 °C, no change was observed in the IR spectrum, but when allowed to warm to room temperature, the spectrum changed within minutes, even in the dark. The ν(CO) band at 2058 cm^{-1} was seen to decrease in intensity with a concomitant growth of a new band at 2023 cm^{-1}, Figure III-9. At the same time, the CO stretch at 2085 cm^{-1} was seen to shift only 5 cm^{-1}, to 2080 cm^{-1}, while the band at 2018 cm^{-1} overlapped with the growing band at 2023 cm^{-1} and no shift in the IR frequency could be observed.

The lone carbonyl of the Fe(IMe)(CO)(NO) moiety is, by calculations, primarily associated with the band at 2058 cm^{-1} that changes dramatically while the two bands at 2085 and 2018 cm^{-1}, strongly associated with the $Fe_2(CO)_3$ unit are minimally affected,

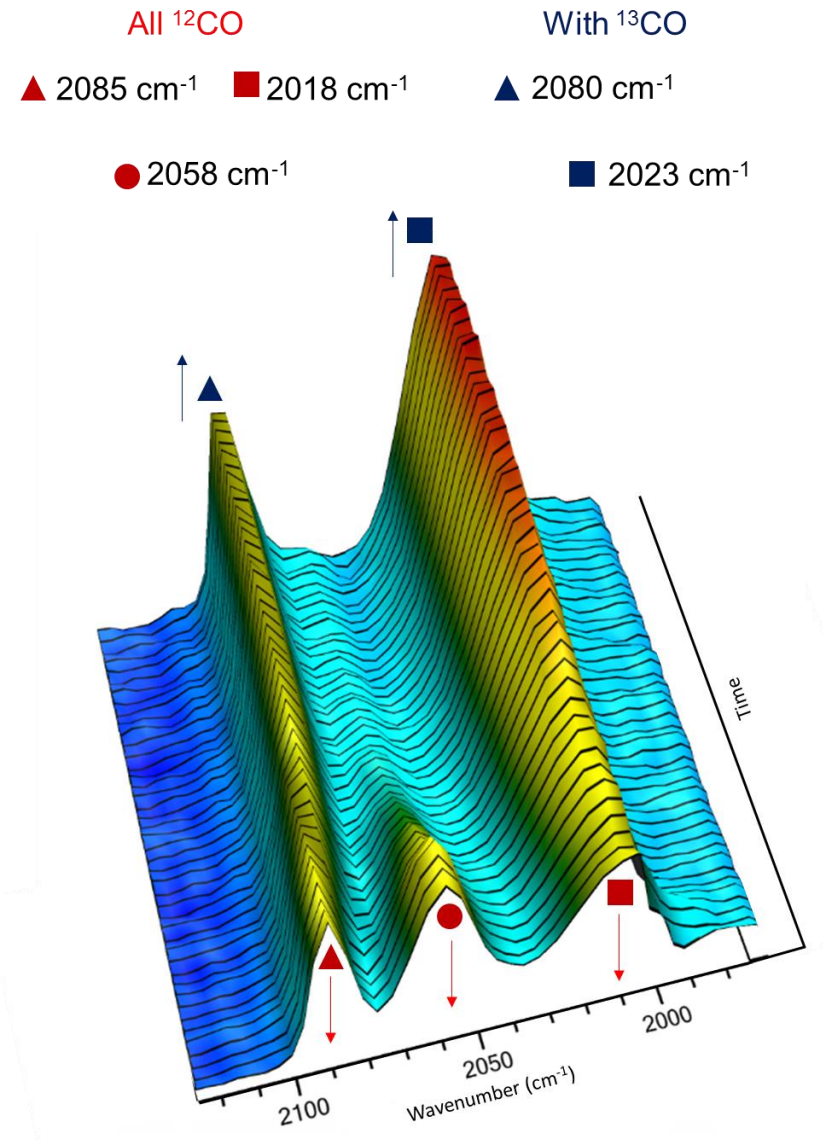

Figure III-9. Three-dimensional stacked plot of the reaction of **2-IMe** with ^{13}CO(g) at 295 K in DCM showing the three CO bands of the all-^{12}CO spectrum (red shapes) shifting to the two band pattern of the selectively substituted complex.

indicating that the ^{13}CO substitution is site selective, exchanging exclusively with the $Fe_1(CO)$. The position shift is in agreement with that expected, as the $^{12}CO/^{13}CO$

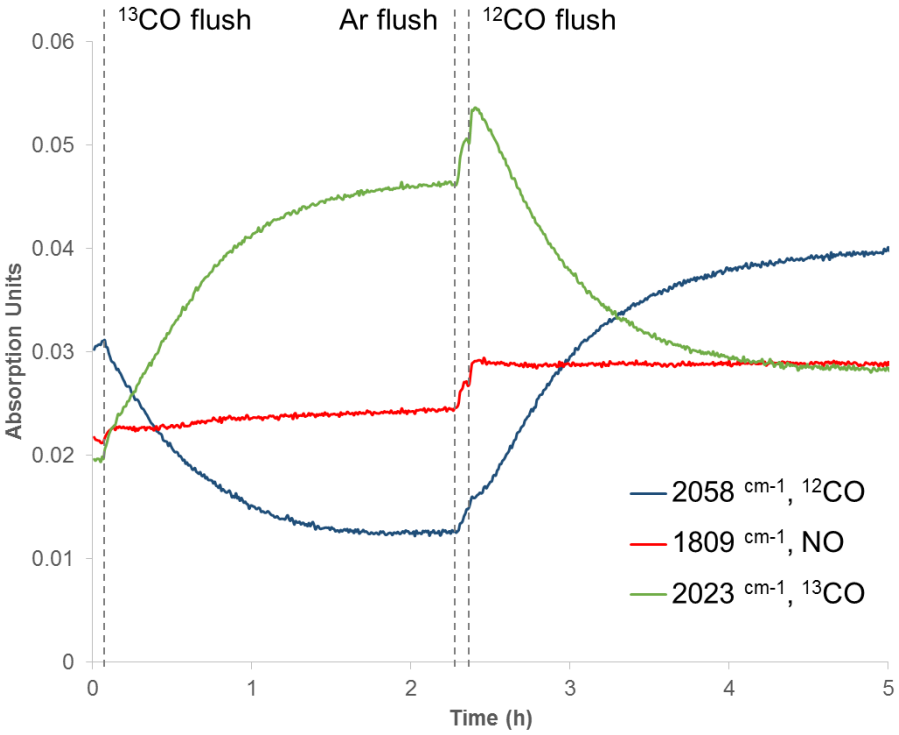

Species	k_{obs} (x 10^4 s^{-1})
2023 cm^{-1}, ^{13}CO ↑	5.32
2058 cm^{-1}, ^{12}CO ↓	-5.59
2058 cm^{-1}, ^{12}CO ↑	5.01
2023 cm^{-1}, ^{13}CO ↓	-5.42

Figure III-10. Top is the reaction profile of IR bands corresponding to the ^{12}CO at 2058 cm^{-1} (blue), the ^{13}CO at 2023 cm^{-1} (green), and the NO at 1809 cm^{-1} (red). The vertical lines show the times when ^{13}CO, argon, and ^{12}CO were flushed into the solution of **2-IMe**. Below are the observed rate constants obtained from linear natural log plots taken over 2-3 half lives.

exchange of a single, uncoupled carbonyl ligand at 2058 cm^{-1} is predicted by the ratio of reduced masses of a single, uncoupled, CO to shift to 2012 cm^{-1}.

In the absence of light, CO adduct formation is observed to take place on the open site of the distal iron in the active site of the [FeFe]-H_2ase. When illuminated, the active site

undergoes $^{12}CO/^{13}CO$ exchange only on that iron. An analogue of the active site reported by Thomas *et al.*,[181] the mixed-valent, $Fe^{I}Fe^{II}$, complex (μ-pdt)(μ-CO)[Fe(IMes)(CO)][Fe(PMe_3)$(CO)_2$]$^+$, **5-IMes**$^+$, is known to exchange CO ligands but only on the "rotated" iron that contains an open site. When this species is exposed to 1 atm. of ^{13}CO for 15 minutes in the dark, then reduced back to the diamagnetic $Fe^{I}Fe^{I}$, complex (μ-pdt)[Fe(IMes)$(CO)_2$][Fe(PMe_3)$(CO)_2$], **5-IMes**, ^{13}C NMR spectroscopy shows that the two carbonyl ligands attached to the same iron as the IMes ligand are labeled while the two carbonyl ligands attached to the same iron as the PMe_3 ligand are not.[181] This regioselective $^{12}CO/^{13}CO$ exchange is similar to what is observed with the complex **2-IMe**.

The $^{12}CO/^{13}CO$ exchange reaction was monitored by *in situ* IR spectroscopy and found to have a half-life of 22 minutes at 23 °C in DCM; the rates are provided in Figure III-10. The labeling of the single $Fe_I(CO)$ of **2-IMe** is effectively complete in two hours. At this point, the system may be purged with argon and the atmosphere replaced with natural abundance carbon monoxide. The reverse reaction, substitution of the ^{12}CO for the single ^{13}CO occurs cleanly, regenerating the all-C-12 IR spectrum at the same rate, Figure III-10.

The photo-dissociation of carbon monoxide from (μ-pdt)[Fe$(CO)_3$]$_2$ is a well-known method for promoting $^{13}CO/^{12}CO$ exchange for the enhancement of ^{13}C NMR studies. This technique does not allow for selective CO lability, either in the iron on which the CO is exchanged or the number of CO ligands exchanged. The thus-obtained ^{13}CO substituted

complex was used as the precursor to synthesize **2-IMe** in which all of the CO ligands are equally enriched. The ^{13}C NMR spectrum of this complex at 0 °C reveals four resonances in the CO region as all four carbonyls are distinct, including the two basal carbonyls of the $Fe(CO)_3$ unit, which are distinguished as being *transoid* or *cisoid* to the NHC on the opposite iron, Figure III-11. On warming this compound to 30 °C, no change is observed in the positions or intensities of the resonances, although the three peaks assigned to the $Fe(CO)_3$ carbonyls broaden slightly. This result is in agreement with the high (*ca.* 19 kcal/mol) calculated barrier to the rotation of the $Fe(CO)_3$ unit, *vida infra.*

The regioselective exchange of only the Fe_1-CO is equally productive in total darkness and under ambient light at room temperature and takes place at a single site. The ^{13}C NMR spectrum of this regioselectively enriched complex at 0 °C shows the same four resonances as above, but the peak at 207.1 ppm, assigned to the $Fe_1(CO)$, is much more intense, Figure III-12. Integration of this spectrum reveals that the ratio of ^{13}CO that has been exchanged for the $Fe_1(CO)$ relative to the $Fe_2(CO)_3$ carbonyls is 9:1. This was less than anticipated, as the predicted $^{13}C/^{12}C$ molar ratio is 17:1, assuming full exchange of the $Fe_1(CO)$ and no exchange of the $Fe_2(CO)_3$ carbonyls. There are three possible explanations for the lower than expected ratio.

The first possibility is an incomplete labelling of the $Fe_1(CO)$ due to less than full exchange with the $^{13}CO(g)$ atmosphere. However, FTIR spectroscopy of this sample confirms a nearly quantitative conversion to $Fe_1(^{13}CO)$ as seen in the absence of a ν(CO) peak at 2058 cm^{-1}.

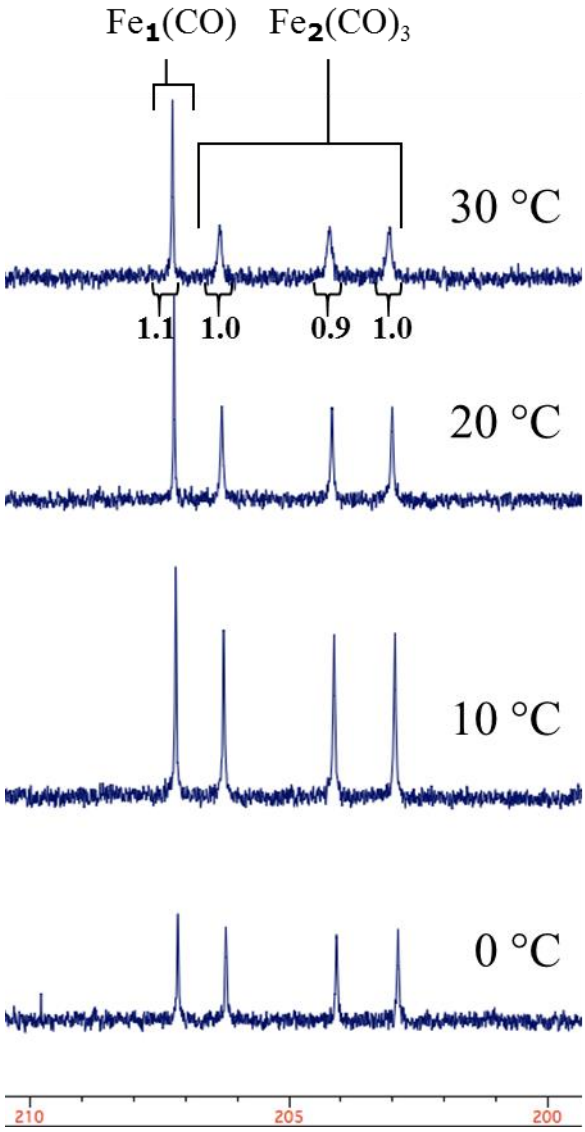

Figure III-11. The uniformly enriched ^{13}C NMR spectra of **2-IMe** in CD_2Cl_2 in the carbonyl region displaying four resonances, from 0 °C to 30 °C. The peak at 207.1 ppm is attributed to the $Fe_1(CO)$ and remains sharp at higher temperatures while the three peaks at 206.2, 204.0 and 202.9 ppm are attributed to the $Fe_2(CO)_3$ and broaden at higher temperatures.

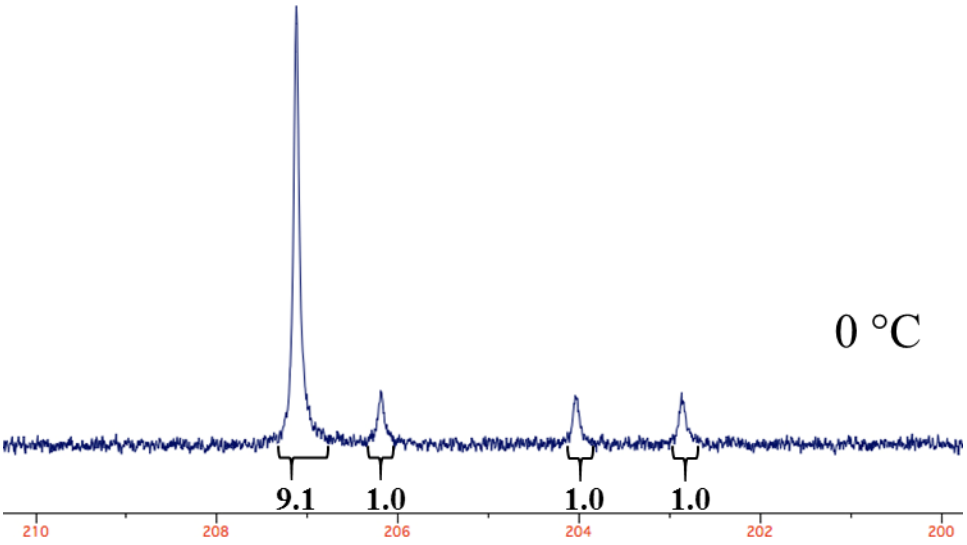

Figure III-12. The selectively enriched ^{13}C NMR spectra of **2-IMe** in CD_2Cl_2 in the carbonyl region at 0 °C. The peak at 207.1 ppm is ~9 times the intensity of the three peaks at 206.2, 204.0 and 202.9 ppm, showing selective $^{13}CO/^{12}CO$ exchange at a single site.

The second explanation of the NMR spectrum is intramolecular site exchange, whereby the labelled ^{13}CO on the $Fe_1(CO)$ is exchanged with an unlabeled ^{12}CO on the $Fe_2(CO)_3$. This hypothesis was tested by monitoring a sample of the regioselectively labelled **2-IMe** by ^{13}C NMR spectroscopy at 20 °C. If the carbonyl ligands were undergoing exchange between the iron atoms, a leveling of the four CO resonances would be observed. However, there was no change in the relative intensities of the $Fe_1(CO)$ and $Fe_2(CO)_3$ resonances after two hours, indicating that no site exchange is occurring.

The third possible explanation of the NMR spectrum is that the $Fe_2(CO)_3$ slowly undergoes $^{13}CO/^{12}CO$ exchange independently of the $Fe_1(CO)$ exchange. As described in Chapter II, an experiment was performed in which a solution of complex **2-IMe** in CD_2Cl_2 was placed under a blanket of ^{13}CO at room temperature and aliquots were removed at 0, 10, 20 and 30 minutes and flash-frozen under N_2. The ^{13}C NMR spectra of these samples show a rapid increase of the intensity of the carbonyl band assigned to the $Fe_1(CO)$ and a much slower increase of the intensity of the three carbonyls assigned to the $Fe_2(CO)_3$. This indicates that the $Fe_2(CO)_3$ is exchanging with the ^{13}CO atmosphere in the reaction flask, but at a much slower rate than the $Fe_1(CO)$.

This thermal exchange of this single carbonyl is presumed to be due to the weakened Fe_1-C bond upon coordination of an NO ligand to the iron. As mentioned above, the thermal dissociation of CO from **2-IMe** is expected to be the source of the instability of the complex in solution. The reduction in bond strength of the Fe_1-CO can be attributed to the increased electron-withdrawing effects of the NO ligand, as the $Fe_1(IMe)(CO)(NO)$ moiety is more electron poor than the $Fe_2(CO)_3$ unit, *vida infra*.

*Density Functional Theory Investigation of Structure Isomer Stability of **2-IMe**, **3-IMe**, and **4-IMe***

In order to gain insight into the structures of **2-IMe**, **3-IMe**, and **4-IMe**, a series of isomers of formula $(\mu\text{-pdt})[Fe_2(CO)_3(NO)(IMe)(L)]^{n+}$, L = CO (**2-IMe**), CN (**3-IMe**), and PMe_3 (**4-IMe**) were optimized using the B3LYP functional[153-155] with the 6-311+G(d,p) basis set[156,157] on all atoms. The calculated free energies reported relative to the isomer

corresponding to the X-ray crystal structure of each, Figures III-13, III-14, III-15 and III-16. The specific questions addressed by the calculations are as follows:

- What is the effect on the stability of complex **2-IMe** if there is no structural rearrangement or if the carbene and NO ligands are on separate irons? (Figure III-13)
- What is the difference between CO and NO bridging the two iron atoms for complex **2-IMe** and what is the effect of the Fe(IMe)(NO)(CO) unit on the rotation of the $Fe(CO)_3$ moiety? (Figure III-14)
- What is the effect on the stability of complex **3-IMe** if the two strong donor ligands are on a different iron than the NO or if they are on a different iron than each other? (Figure III-15)
- What is the difference in stability between complex **4-IMe** and **6-IMe**? Is the bridging CO isomer of **6-IMe** more stable than the all-terminal isomer? (Figure III-16)

The various permutations of the strong σ-donating ligands (IMe, CN, and PMe_3) and π-withdrawing ligand (NO) on each of the iron atoms were investigated to find the most thermodynamically stable form of each structure. The most stable forms of **2-IMe** have the IMe and NO ligands on the same iron, as is observed in the crystal structure. However, this calculation can only inform on the thermodynamic stabilities; there is no way for this study to determine if this is the kinetic product as well.

The structures of in which there are two strong σ-donors, **3-IMe** (IMe and CN) and **4-IMe** (IMe and PMe_3), are generally more stable if the donating ligands are on separate irons. Despite the thermodynamic stability of the symmetric distribution of the strong donor ligands, this is <u>not</u> what is observed in the crystal structures, which are both the dissymmetric complexes. This is evidence that the result of addition of CN or PMe_3 to **2-IMe** is the kinetic product, rather than the thermodynamic product.

All possible permutations of the formula (μ-pdt)$[Fe_2(CO)_4(NO)(IMe)]^+$ in which the bridging propane dithiolate ligand is positioned away from the $Fe_1(NO)$, are displayed in Figure III-13, which contains the all-terminal or unrotated structures, and Figure III-14, which contains the rotated structures. All energies are reported relative to the structure corresponding to the X-ray crystal structure, **2-IMe-1**. The isomer resulting from positioning the IMe ligand apical (**2-IMe-2**) or CO apical (**2-IMe-3**) is less stable than **2-IMe-1** by 1.3 and 2.0 kcal/mol, respectively. Isomers resulting from moving the IMe ligand onto Fe_2 in either the apical (**2-IMe-4**) or basal (**2-IMe-5**) position are also higher in energy, by 1.8 and 1.7 kcal/mol, respectively. Finally, leaving the IMe ligand on Fe_2, but moving the NO into a basal position yields three possible isomers that are 2.0 (**2-IMe-6**), 2.5 (**2-IMe-7**), and 3.2 (**2-IMe-8**) kcal/mol less stable than **2-IMe-1**.

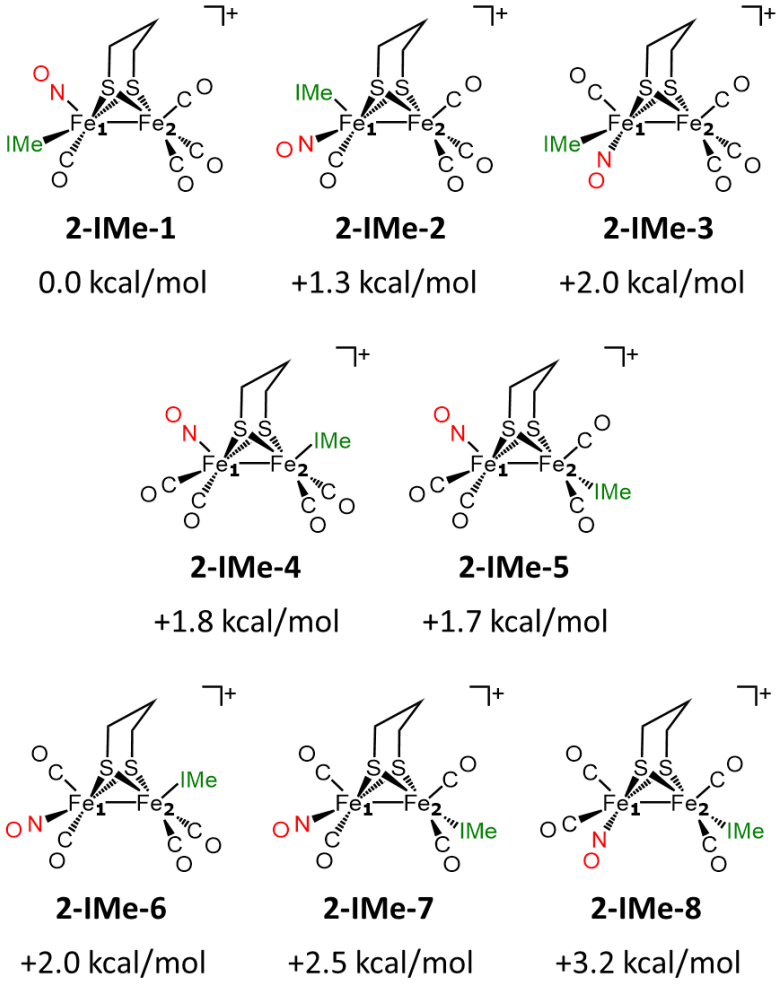

Figure III-13. Calculated relative energies of all-terminal isomers of (μ-pdt)[$Fe_2(CO)_4(NO)(IMe)]^+$, relative to **2-IMe-1**, the structure corresponding to **2-IMe**.

Structures corresponding to the "rotated" structure, with an inverted square pyramid about one iron atom and a carbonyl ligand bridging the two iron atoms, are known to exist as transition states along the rotation of the $Fe(CO)_x(L)_{3-x}$ moiety, Figure III-14. A full description of the rotations of the $Fe(CO)_3$ unit may be found in Chapter IV. Thus, the rotation of the $[Fe(IMe)(CO)(NO)]^+$ moiety has a single bridging CO structure, the

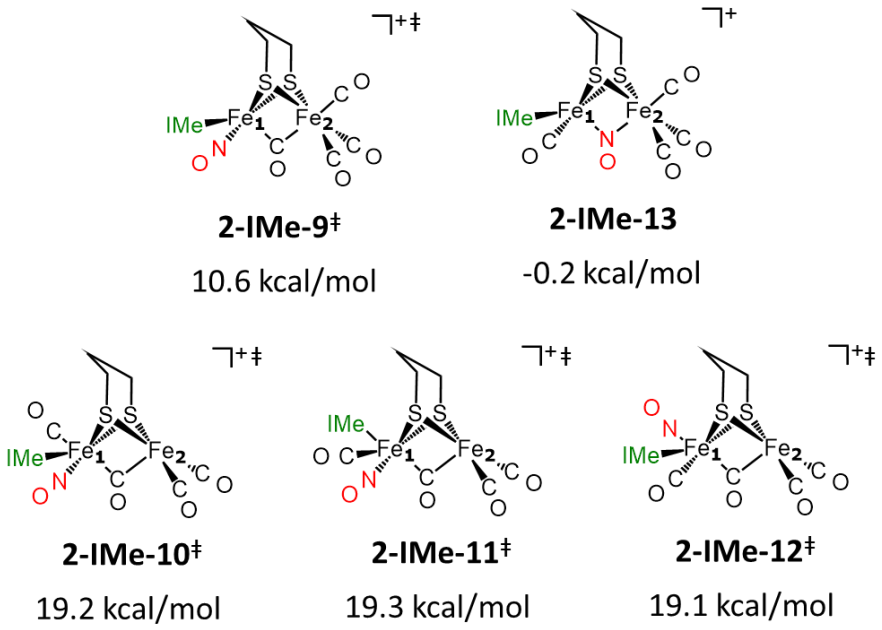

Figure III-14. Calculated relative energies of rotated structures of (μ-pdt)[$Fe_2(CO)_4(NO)(IMe)$]$^+$, consisting of four transition states and one ground state isomer, relative to **2-IMe-1**.

transition state of the rotation that exchanges NO and IMe as apical ligands. This transition, **2-IMe-9**‡, at 10.6 kcal/mol, is only slightly higher in energy than the calculated rotation barrier of an $Fe(CO)_3$ unit in complex **1** (9.6 kcal/mol).[122,182] The rotation of the $Fe_2(CO)_3$ unit of **2-IMe** has a much higher energy barrier. If the apical ligand on the opposite iron is NO, **2-IMe-12**‡, the barrier is 19.1 kcal/mol; there is little difference when the apical ligand on Fe_1 is either IMe (**2-IMe-10**‡, 19.2 kcal/mol) or CO (**2-IMe-11**‡, 19.3 kcal/mol). Attempts to locate a transition state with the NO in a bridging position were unsuccessful; however, a structure with the bridging NO was located as a ground state isomer, **2-IMe-13**, which was 0.2 kcal/mol more stable than **2-IMe-1**. This isomer, calculated in the gas phase, is not experimentally observed, as the expected NO stretch in

the IR spectrum near 1500 cm^{-1},[174] much lower than the observed 1809 cm^{-1} is not found. Additional CO stretches would also appear at higher frequencies than the three ν(CO) bands observed for **2-IMe**.

In the same manner as the study of **2-IMe**, investigations of the isomers of **3-IMe** and **4-IMe** were performed with the free energy of various isomers of (μ-pdt)[$Fe_2(CO)_3$(NO)(IMe)(CN)] reported relative to **3-IMe-1**, Figure III-15, and of (μ-pdt)[$Fe_2(CO)_3$(NO)(IMe)$(PMe_3)]^+$ reported relative to **4-IMe-1**, Figure III-16. Isomers resulting from separation of the electrophilic NO ligand and nucleophilic IMe and CN ligands onto separate Fe atoms are less stable than **3-IMe-1** by 3.2 kcal/mol if NO is apical

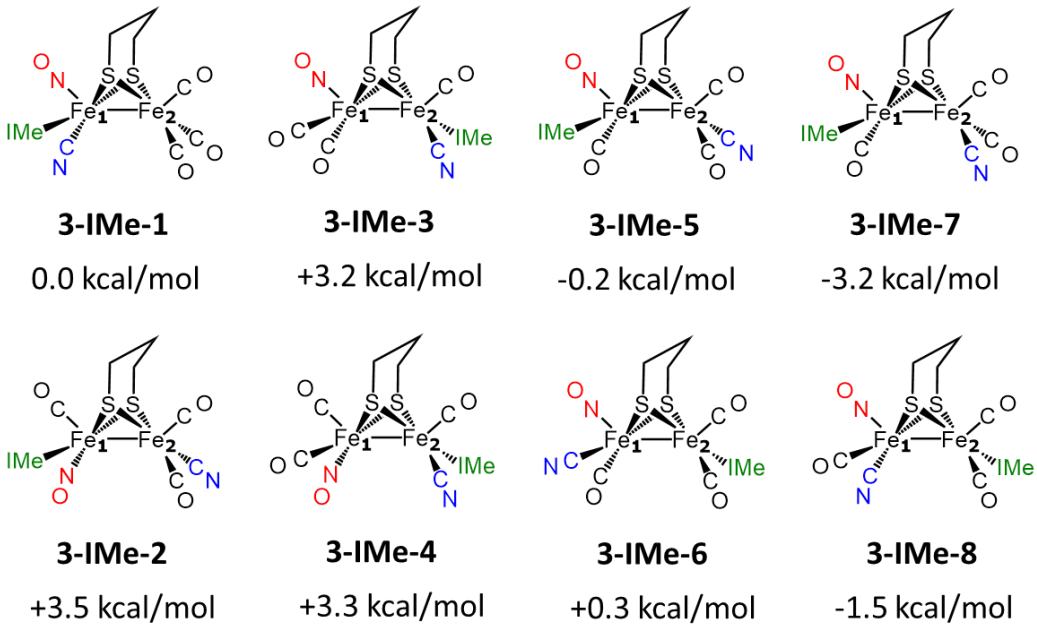

Figure III-15. Calculated relative energies of selected isomers of (μ-pdt)[$Fe_2(CO)_3$(NO)(IMe)(CN)] relative to **3-IMe-1**, the structure corresponding to **3-IMe**.

(**3-IMe-3**), and 3.3 kcal/mol if NO is basal (**3-IMe-4**). A more stable series of isomers involves separation of the nucleophilic ligands onto the two irons. If the two nucleophiles are *transoid*, the isomeric structures are very close in energy to **3-IMe-1**, being 0.2 kcal/mol more stable if IMe is on the same Fe_1 as NO (**3-IMe-5**) and 0.3 kcal/mol less stable if CN is on Fe_1 instead (**3-IMe-6**). When the NO is moved from an apical position, **3-IMe-5**, to a basal position, **3-IMe-2**, the calculated structure is 3.7 kcal/mol higher in energy. If the nucleophilic ligands are *cisoid* instead, the isomers are more stable by 3.4 kcal/mol, with the IMe ligand on the Fe with NO, Fe_1, (**3-IMe-7**) and 1.5 kcal/mol, with the CN ligand on Fe_1 (**3-IMe-8**). The increased stability of the isomers of **3-IMe** that separate the nucleophilic ligands onto different irons is also seen with the isomers of **4-IMe**, Figure III-16. Moving the PMe_3 ligand onto Fe_2, **4-IMe-2**, results in greater stability than the fully dissymmetric **4-IMe-1**, by 3.6 kcal/mol. An even lower energy isomer, obtained by the rotation of the Fe_1, resulting in a bridging CO, **4-IMe-3**, is more stable

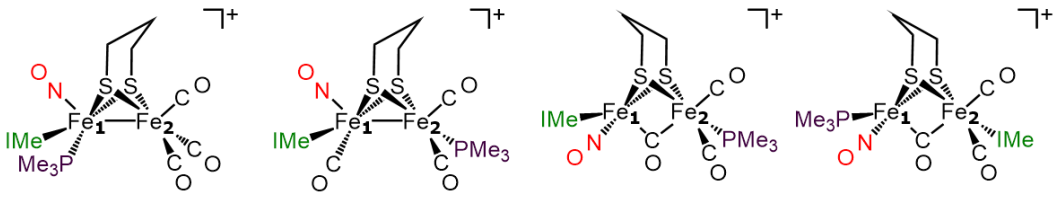

Figure III-16. Calculated relative energies of selected isomers of (μ-pdt)$[Fe_2(CO)_3(NO)(IMe)(PMe_3)]^+$, a comparison of the stability of **4-NHC (4-IMe-1)** and **6-NHC (4-IMe-3)** relative to **4-IMe-1**.

than **4-IMe-1** by 5.0 kcal/mol. This isomer corresponds to the X-ray structure of **6-IMes** *sans* the bulky mesityl groups on the carbene. Another rotated isomer, in which the carbene and phosphine ligands of **4-IMe-3** are switched, **4-IMe-4**, is yet more stable at 9.0 kcal/mol less than **4-IMe-1.**

Concluding Remarks

The Regioselectivity of Nucleophilic and Electrophilic Ligand Substitution on a Diiron Carbonyl Framework

The regioselective PMe_3/CO substitution of **1-IMe** and **2-IMe** offers insight into the diiron core's electronic response to its ligand environment. In an associative ligand exchange on the [FeFe] framework, the incoming nucleophile preferentially attacks the iron with the more π-acidic ligand set, which is more polarizable and may be considered the "softer" iron, Figure III-17. The softer iron is apparent in the case of **1-IMe**, as the $Fe(CO)_3$ unit is more capable of accommodating the nucleophile than the $Fe(IMe)(CO)_2$ moiety. Upon PMe_3/CO substitution, the resulting complex, **5-IMe**, is symmetric with regard to the number of strong σ-donor ligands on each iron. If the incoming ligand is more electrophilic, attack is expected to take place on the iron with the less π-acidic ligand set, i.e., the less polarizable or "harder" iron, Figure III-12. Thus, NO^+/CO substitution of **1-IMe** would be favored to take place on the $Fe(IMe)(CO)_2$ moiety, generating **2-IMe**. Figure III-13 shows that the calculated thermodynamic difference in NO^+ coordination on the two iron atoms is small, only 1.7 kcal/mol, but the observation of a single reaction

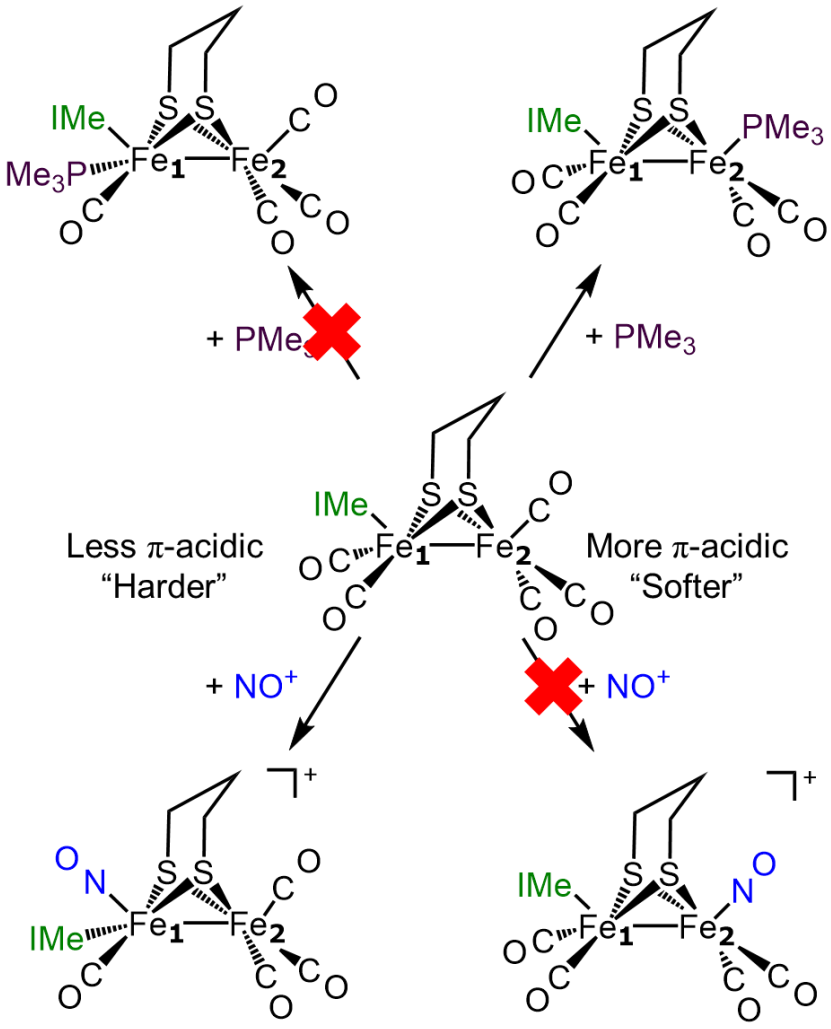

Figure III-17. The $Fe(IMe)(CO)_2$ is less π-acidic than the $Fe(CO)_3$. An incoming nucleophile, such as PMe_3, will attack the more π-acidic $Fe(CO)_3$ (top) while an electrophile like NO^+ is prone to substitution on the less π-acidic $Fe(IMe)(CO)_2$.

product indicates the IMe ligand is much less π-acidic than a CO. In the PMe_3/CO substitution of **2-IMe**, two possible isomers can be imagined. If the Fe(IMe)(CO)(NO) unit is more π-acidic, the totally dissymmetric product, **4-IMe**, will be synthesized. If

instead, the $Fe(CO)_3$ is more π-acidic, the more symmetric **6-IMe** will be observed At 0 °C, the only product observed of the PMe_3/CO exchange is **4-IMe**. Therefore, the $Fe(CO)_3$ moiety is less π-acidic than the Fe(IMe)(CO)(NO) unit. Figure III-15 shows that this is not the most stable isomer of the formula (μ-pdt)$[Fe_2(CO)_3(IMe)(PMe_3)(NO)]^+$, indicating kinetic control of the reaction.

CHAPTER IV

COMPUTATIONAL STUDIES RELATING TO (μ-SRS)[Fe(CO)$_3$]$_2$ AS INFORMANTS ON THE [FeFe]-HYDROGENASE ACTIVE SITE: INTRAMOLECULAR SITE EXCHANGE*

Preface

Chapter IV describes my contributions to the following co-authored manuscript: "Conformational Mobility and Pendent Base Effects on Electrochemistry of Synthetic Analogues of the [FeFe]-Hydrogenase Active Site" Crouthers, D. J.; Denny, J. A.; Bethel, R. D.; Munoz, D. G.; Darensbourg, M. Y.; *Organometallics*, DOI: 10.1021/om500023j (2014). My computational results, found within that publication, were used to identify the transition states corresponding to the processes investigated by VT NMR and to support the assignment of the fluxional processes observed experimentally. All of my published results are provided herein, as well as an extended description and discussion of those findings.

*This chapter is reproduced in part with permission from Crouthers, D. J. D., J. A.; Bethel, R. D.; Munoz, D. G.; Darensbourg, M. Y., Conformational Mobility and Pendent Base Effects on Electrochemistry of Synthetic Analogues of the [FeFe]-Hydrogenase Active Site. *Organometallics* DOI: 10.1021/om500023j (2014). Copyright 2014 ACS Publications

Introduction

Summary of the Paper

The investigation of the (μ-SRS)[Fe(CO)$_3$]$_2$ series of complexes as mimics of the [FeFe]-H$_2$ase active site has been a focus of organometallic chemists since the enzymatic structure was elucidated some 15 years ago.[104,106,183] Figure IV-1 is adapted from our paper[182] and displays the active site of the [FeFe]-H$_2$ase as determined by protein crystallography, Figure IV-1 (A). One area of investigation of the simple models involves the intramolecular site exchange processes as it has been suggested that the well-known dynamics[122,184-186] of such compounds may relate to the requirement for configurational mobility in order to function as solution electrocatalysts for the reduction of protons to produce H$_2$. The structure in Figure IV-1 (B) is that of the so-called parent model complex (μ-pdt)[Fe(CO)$_3$]$_2$, pdt = propane-1,3-dithiolate,[183] from which numerous derivatives have been prepared. This complex, perhaps more than any other, has provided an entry point

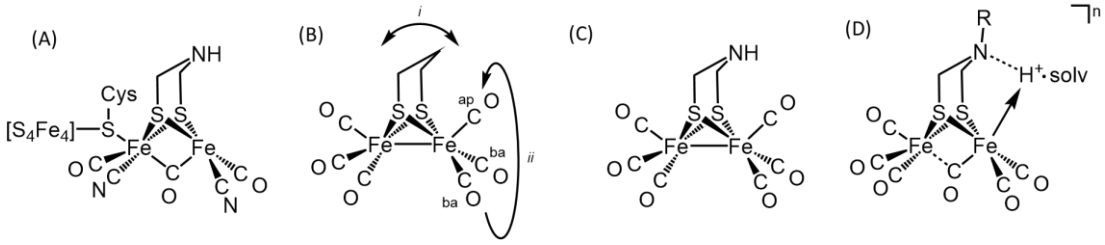

Figure IV-1. Depiction of (A) the 6Fe H-cluster of the [FeFe]-H$_2$ase active site;[9] (B) the (μ-pdt)[Fe(CO)$_3$]$_2$ parent model complex, in the eclipsed, "all-terminal" geometry and its fluxional processes: *i.* chair/boat interconversion, *ii.* apical/basal CO site exchange;[122] (C) (μ-adt)[Fe(CO)$_3$]$_2$ with a N bridgehead;[167] (D) the expected transition state during protonation of reduced (μ-adt)[Fe(CO)$_3$]$_2^{n-}$.[122]

into biomimetic chemistry for the organometallic community. In particular, its spectroscopic handle, FTIR in the diatomic region, permitted the close monitor of electron density at the iron centers. Carbon-13 and proton NMR spectroscopy has been used to interrogate the fluxional processes involved in the chair/boat interconversion of the FeS_2C_3 metallacycle, as the 6-membered ring flips from one side to the other, Figure IV-1 (B, *i*), and the apical/basal CO site exchange through a turnstile type $Fe(CO)_3$ rotation, Figure IV-1 (B, *ii*).[106]

In the neutral Fe^IFe^I redox level, the (μ-pdt)$[Fe(CO)_3]_2$ complex is in an edge-bridged bi-square pyramidal geometry with the CO ligands in an eclipsed, "all-terminal" geometry. The HOMO of this complex well delineates the Fe—Fe bond.[122] Theory has shown that this bond may be weakened by either oxidation, removing an electron from the bonding orbital, or reduction, adding an electron to the LUMO, which is Fe—Fe antibonding in character.[122] According to theory, both lead to an easier access to the so-called "rotated" isomer. This isomeric form results from the reorientation of one of the $Fe(CO)_3$ units by rotation, or inversion, maintaining the μ-SRS unit, in order to expose that iron to attack at the now revealed terminal open site.

Another series of model complexes utilize the azadithiolate (adt) bridging ligand,[167] as seen in the complex (μ-adt)$[Fe(CO)_3]_2$, Figure IV-1 (C). These complexes have an amine in the "bridgehead" position of the bridging dithiolate cofactor that facilitates proton transfer to and from the catalytic iron site, as shown in Figure IV-1 (D).[122] This pendent amine, within 3.5 Å of the open faced iron, is critical to the function of the enzyme, as

demonstrated by recent reports of the hybrid synthesis of an [FeFe]-H_2ase enzyme with an active site derived from small molecule compounds containing either CH_2 or NH bridgeheads. Only the azadithiolate-bridged diiron subsite is capable of reducing protons to generate H_2.[53,142]

The experiments in this study investigated the fluxional processes of a series of diiron hexacarbonyl complexes, using variable temperature NMR spectroscopy, and looked for a correlation with their function as solution proton reduction electrocatalysts, determined by cyclic voltammetric responses to added acid.[107] It was found that the energy barriers of the fluxional processes related to the steric bulk of the bridging dithiolate ligand that can be directed towards an $Fe(CO)_3$ unit. However, differences in the mobility of the diiron complexes did not correlate with their electrocatalytic reduction of protons. Instead, the presence of an amine in the bridgehead position of the dithiolate ligand was responsible for a 1.5- to 2- fold increase in electrochemical response to acid when compared to the species with carbon in the bridgehead of comparable steric bulk.

^{1}H and ^{13}C VT NMR Studies

In addition to the proton signals from the substituent in the bridgehead position of the bridging dithiolate ligand, the rapidly equilibrating methylene (elbow carbon) protons for **NH**, **NMe**, **NtBu**, **pdt**, and **dmpdt** show a single resonance in the ^{1}H NMR spectra at room temperature.[106] For many of the complexes, these signals are observed to resolve into two broad resonances when cooled to the slow exchange regime, reflecting the nonequivalency of the axial and equatorial H atoms. From this, the energy barrier of the

chair/boat interconversion of the FeS_2C_2X metallacycle can be experimentally determined.[187]

The $Fe(CO)_3$ rotor fluxionality was measured by VT ^{13}C NMR spectroscopy. From the values for the chair/boat interconversion, Figure IV-1 (B, *i*), and CO intramolecular site exchange, Figure IV-1 (B, *ii*), energy barriers of all complexes were obtained using the formulas $\Delta G^{\ddagger} = -(RT)\ln[k_t h/k_b T_{coal}]$ and $k_t = (\pi\Delta\nu)/2^{1/2}$, where the coalescence temperature (T_{coal}) and peak separation ($\Delta\nu$) were found from analysis of the spectra.[187]

Computational Investigation of the Structures and Fluxional Processes of Diiron Hexacarbonyl Complexes

Density Functional Theory was utilized in the study of the $(\mu\text{-SRS})[Fe(CO)_3]_2$ complexes. Specific questions asked of the calculations were:

- Can the calculations provide structures with both the geometry and vibrational frequencies comparable to the experimental data?
- Can the calculations locate the transition state structures of the fluxional processes known to take place in the $(\mu\text{-SRS})[Fe(CO)_3]_2$ system?
- Do the calculated energies of those transition states compare favourably to the experimental energy barriers of those processes?
- Does the choice of functional affect the calculated geometries of the ground state and transition state structures and their relative energies?
- Can the calculations provide insight into the experimental results that are ambiguous or, because of certain limitations, cannot be measured?

The structures and fluxional processes of the (μ-SRS)[$Fe(CO)_3$]$_2$ complexes have been previously investigated by DFT. Hall and co-workers have shown that the rotation of the $Fe(CO)_3$ moiety leads to a transition state, observed by a *ca.* 60 degree twist of the $Fe(CO)_3$ unit.[122] This disrupts the Fe – Fe bond, making the two irons asymmetric in their calculated charges and positions a CO ligand between the iron atoms in a semi-bridging position. It has been shown that addition of steric bulk on the bridging ligand decreases the barrier to rotation; changing the "bridgehead" atom from carbon to nitrogen, as in Figure IV-1 (B) and (C), does not have a notable effect on the rotation barrier for (μ-$(SCH_2)_2X$)[$Fe(CO)_3$]$_2$, where X = CH_2 or NH. The effects of ligands other than CO on the structure of diiron dithiolate have been investigated by Hall, who has demonstrated that good donor ligands, such as phosphine, may subtly raise the rotation energy barrier if the donor ligand is *trans* to the bridging site.[122] The computational investigations of de Gioia have also been utilized in the investigation of (μ-pdt)[$Fe_2(CO)_5(CN)]^-$, where the transition state corresponding to the bridgehead flip was located and the interconversion of isomers varying by cyanide position were compared.[185] The calculated ring flip energy was reported to be slightly higher (8.7-9.8 kcal/mol) than the experimental energy barrier (9.3 kcal/mol).

Table IV-1. Experimental and *calculated* spectroscopic and metric parameters of (μ-SRS)[Fe(CO)$_3$]$_2$

Complex	IR ν(CO) (cm^{-1})[a]	Fe - Fe (Å)	S - S (Å)	torsion angle (°)[b]	C/N --- Fe (Å)[c]
NH	2075, 2036, 2007, 1990, 1981	2.5150(3)	3.045(2)	0.00(9)	3.47(2)
	2067, 2028, 2007, 1985, 1975	*2.522*	*3.113*	*0.096*	*3.498*
NMe	2075, 2036, 2002, 1990, 1984	2.4924(7)	3.0398(7)	0.0(4)	3.27(1)
	2066, 2029, 2003, 1992, 1981	*2.524*	*3.099*	*0.079*	*3.320*
NtBu	2075, 2036, 2002, 1994, 1982	2.5172(9)	3.0147(8)	6.1(2)	3.319(2)
	2065, 2026, 2003, 1987, 1978	*2.520*	*3.082*	*0.762*	*3.359*
S-S	2084, 2044, 2007	2.553(4)	2.006(3)	0.89(1)	-
	2077, 2037, 2011, 2004, 1990	*2.549*	*2.078*	*0.035*	-
edt	2078, 2037, 2008, 1995, 1986	2.502(1)	2.886(1)	1.0(4)	-
	2069, 2030, 2007, 1992, 1983	*2.512*	*2.951*	*0.104*	-
pdt	2076, 2035, 2005, 1992, 1981	2.5105(8)	3.050(2)	0.0(2)	3.498(6)
	2067, 2028, 2006, 1987, 1979	*2.515*	*3.106*	*0.162*	*3.522*
dmpdt	2075, 2034, 2005, 1992, 1980	2.4939(4)	3.0171(7)	6.5(2)	3.735(2)
	2067, 2037, 2007, 1985, 1976	*2.506*	*3.066*	*0.000*[d]	*3.822*

[a]Experimental IR spectra obtained in hexanes, calculated IR spectra obtained using TPSSTPSS functional and 6-311+G(d,p) basis set on all atoms. [b]CO_{ap}-Fe-Fe'-$CO_{ap'}$ angle. [c]Distance from the central atom of the bridgehead (C or N) to the closest iron; the **S-S** and **edt** molecules have no bridgehead. [d]Calculated torsion angle is exactly 0 as the **dmpdt** only optimized into a minimum when constrained to C_s symmetry.

In this chapter, I provide computational support for the experimentally observed effect of steric bulk in lowering the $Fe(CO)_3$ rotation barrier and the negligible effect of carbon versus nitrogen in the bridgehead position, while showing that the bridgehead atom does correspond to a difference in the ring flip. The primary focus of the computational investigation was the identification of the transition states of all fluxional processes involved in the dynamic intramolecular site exchange processes for all complexes as well as the assignment of ^{1}H and ^{13}C NMR resonances at various temperatures. In total, 8 ground states and 21 transition states were located for each of four functionals, resulting in a total of 116 relevant structures. A summary and comparison of experimental and computed ν(CO) stretching frequencies and important metric parameters is provided in Table IV-1.

The four functionals selected for this investigation were B3LYP,[153-155] TPSSTPSS,[162] MPW1PW91,[161] and ω-B97xD[163] and each utilized the 6-311+G(d,p) basis set[156,157] on all atoms.

The B3LYP functional was originally selected for this investigation as it was utilized by Hall, de Gioia, and others for their investigations into the [FeFe]-H_2ase active site and the myriad model complexes thereof.[60,122,184,186,188,189] In the B3LYP functional, the B3 exchange functional,[153,154] which contains partial Hartree-Fock exchange, is paired with the correlation functional of Lee, Yang, and Par (LYP).[155] This combination has been specifically optimized as a hybrid functional, and is immensely popular.[190] As an example of its popularity, Sousa *et al.* analysed the titles and abstracts of every paper in the Web

of Science from 1990 to 2006, and found that 80% of the functionals listed were B3LYP.[191]

The TPSSTPSS functional developed by Tao, Perdew, Staroverov, and Scuseria combines their exchange and correlation functionals.[162] This pure-DFT functional does not contain any Hartree-Fock exchange, but it has been reported to improve on the overestimated bond lengths and poor vibrational frequencies of previous functionals of this type.[192]

The MPW1PW91 functional is essentially the Perdew-Wang 1991 functional[193,194] in which the exchange component has been modified by Adamo and Barone,[161] in order to improve the performance of the overall functional. This functional has been found by Truhlar and coworkers to accurately model both covalent and nonconvalent interactions.[195]

The fourth functional, ω-B97xD, is a standalone functional and is not split into exchange and correlation components.[163] Originally devised by Grimme to include dispersion forces, we expected this functional to accurately model the noncovalent interactions between the bridging ligand and the iron carbonyls.[196]

Finally, these calculations provide a means to clarify ambiguous experimental results, such as the low temperature ^{13}C NMR of **NtBu**, in which a single peak may be due to exchange of the carbonyl ligands or a serendipitous overlap of the peaks of non-exchanging COs. The results below provide evidence that the ligands are not exchanging at temperatures lower than -60 °C, but the non-exchanging COs happen to have the same chemical shift. Another benefit of the calculations is the ability to estimate energy barriers

that have not been determined experimentally. For example, the ring flip of **dmpdt** has been observed to continue at temperatures as low as -120 °C.[197] The combination of calculated structures and energies with the experimental energies obtained from VT NMR spectroscopy, the fluxional processes of (μ-SRS)[Fe(CO)$_3$]$_2$ are identified and described below.

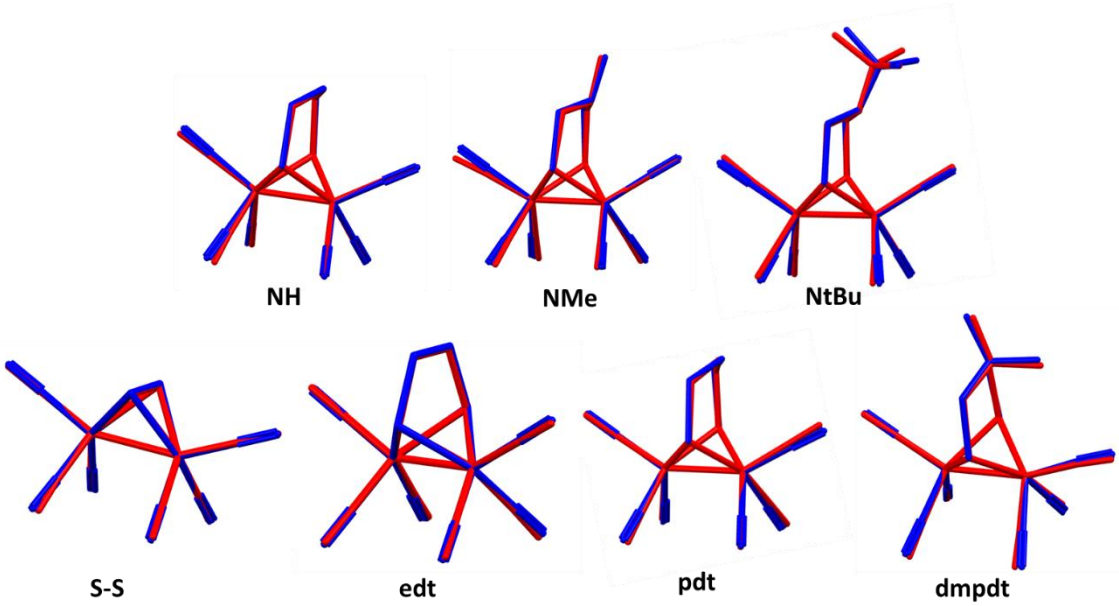

Figure IV-2. Overlays of the seven diiron hexacarbonyl complexes investigated in this chapter are displayed above with the X-ray crystal structures in red and calculated structures, optimized in the gas phase using the B3LYP functional, in blue.

Results and Discussion

Structural Features of Diiron Hexacarbonyl Species

The molecular structures of the following diiron hexacarbonyl complexes (μ-$(SCH_2)NH)[Fe(CO)_3]_2$, **NH**;[167] μ-$(SCH_2)_2N(Me))[Fe(CO)_3]_2$, **NMe**;[96] μ-$(SCH_2)_2N(t$-Bu))$[Fe(CO)_3]_2$, **NtBu**;[167] (μ-$S_2)[Fe(CO)_3]_2$, **S-S**;[198] (μ-$(SCH_2)_2)[Fe(CO)_3]_2$, **edt**;[199] (μ-$(S(CH_2)_3S)[Fe(CO)_3]_2$, **pdt**;[183] and (μ-$(SCH_2)_2C(Me)_2)[Fe(CO)_3]_2$, **dmpdt**;[197] were optimized in the ground state and compared to the structures determined by X-ray diffraction analysis. Selected experimental and calculated metric parameters are provided in Table IV-1 along with ν(CO) IR data. The seven complexes investigated in this study are displayed in Figure IV-2, where the B3LYP calculated structures (blue) are overlaid with the X-ray crystal structures (red). By visual inspection, there is little difference in the structures optimized using any of the four functionals: TPSSTPSS, B3LYP, MPW1PW91, and ω-B97xD.

The crystal structures of both **NH** and **NMe** have the pyramidal amines cocrystalized in both the axial (where the N-R is pointed down, towards the $Fe(CO)_3$) and equatorial (where the N-R is pointed up, away from the $Fe(CO)_3$) positions.[96,167] In contrast, the **NtBu** was experimentally found to crystalize only in the equatorial position.[182] For simplicity, the structures in Figure IV-2 are all shown with the N-R in the equatorial position. This explains the most apparent discrepancy in the overlaid structures, where the apical CO of **NMe**, directed away from the bridgehead, is bent further away from the dithiolate bridge in the crystal structure than in the calculated structure. This is due to the

partial occupancy of an axial N-CH_3 bridgehead that is above that iron, which provides steric repulsion for the apical CO in a manner similar to the C-CH_3 in the **dmpdt** bridgehead.[197] Because the calculated structure does not have this isomer in any occupancy, the unhindered CO is not bent down. Finally, the experimental observation of **NtBu** only in the equatorial conformation is consistent with computational data, for which the axial conformation of the *tert*-butyl group did not converge for all four functionals, *vide infra*.

The four remaining structures are either totally symmetric with respect to the bridging dithiolate and have no bridgehead atom; i.e., the **S-S** and **edt** complexes, or they have CR_2 bridgehead atoms, where R = H (**pdt**) or CH_3 (**dmpdt**). The only minor discrepancy between these calculated and crystal structures is the **dmpdt**, which was optimized as C_s symmetric. Thus, the CO_{ap}-Fe-Fe'-$CO_{ap'}$ dihedral angle is exactly 0°, while the reported dihedral from the crystal structure is 6.5(2)°.[197] Finally, as indicated by almost identical ν(CO) values, Table IV-1, the electron density on the iron centers is the same throughout the series.

*Fluxional Processes of **edt** and **S-S***

The **edt** and **S-S** complexes are the simplest of the diiron hexacarbonyl class in terms of their fluxional processes. The absence of a 6-membered metallacycle eliminates the ring flip process, and without the bridgehead to distinguish the iron atoms, the two $Fe(CO)_3$

Table IV-2. Experimental and computational $Fe(CO)_3$ rotation barriers and FeS_2C_2X ring flip barrier in kcal/mol. The experimental values were determined by ^1H and ^{13}C VT NMR spectroscopy and the computations were carried out with the four functionals listed with the 6-311+G(d,p) basis set on all atoms

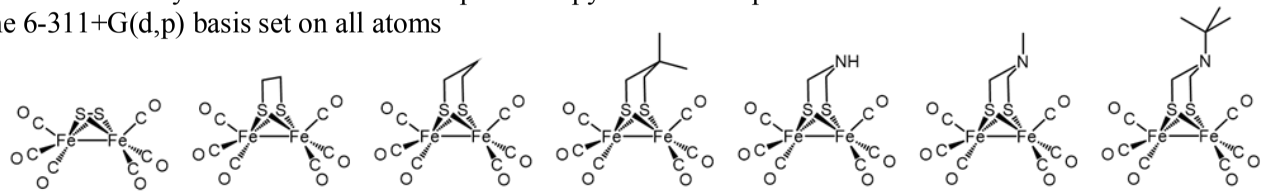

$Fe(CO)_3$ Rotational Barrier	S-S	edt	pdt	dmpdt	NH	NMe	NtBu
Experimental[a]	9.2 (±0.24)	12.1 (±0.24)	9.9 (±0.24)	7.4 (±0.24)	9.4 (±0.24)	8.0 (±0.24)	11.0 (±0.24)
Computed[b,c]							
TPSSTPSS	9.0 / 9.0	12.1 / 12.1	12.4 / 9.6	13.3 / 6.6	12.0 / 9.5	10.9 / 6.6	12.0 / 10.5
B3LYP	11.0 / 11.0	14.1 / 14.1	14.5 / 11.6	15.5 / 9.1	14.1 / 11.5	13.2 / 10.4	14.9 / 14.4
MPW1PW91	10.8 / 10.8	13.8 / 13.8	14.4 / 11.2	15.2 / 8.0	14.1 / 11.1	12.8 / 9.9	13.4 / 13.3
ωB97xD	12.0 / 12.0	15.3 / 15.3	16.1 / 13.0	17.0 / 9.6	16.0 / 12.9	14.8 / 11.6	14.8 / 16.9

Ring Flip Barrier	pdt	dmpdt	NH	NMe	NtBu
Experimental[a]	9.6 (±0.24)	-[d]	13.3 (±0.24)	11.3 (±0.24)	11.2 (±0.24)
Computed[b]					
TPSSTPSS	8.8	5.2[e]	15.1	10.9	10.4
B3LYP	9	5.9[e]	14	10.4	11.6
MPW1PW91	9.5	5.4[e]	14.1	10.5	11.4
ωB97xD	10.7	6.1[e]	14.3	11.4	12.6

[a]Error estimated using ±5 °C for detected coalescence temperature. [b]Computational free energy recalculated at the experimental coalescence temperature using the indicated functionals. [C]The values to the left and right of the slash are the calculated rotation barriers for each iron with respect to the bridgehead position. [d]Experimental data could not be obtained, as the coalescence temperature was < -120 °C. [e]Free energy estimated by using the coalescence temperature of the $Fe(CO)_3$ rotation, -87 °C.

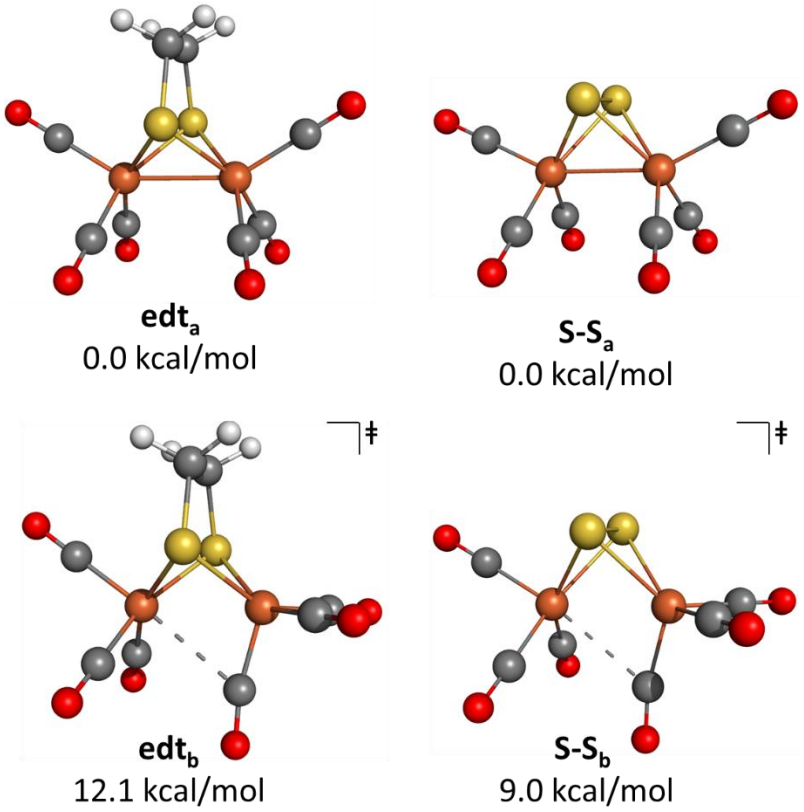

Figure IV-3. Calculated structures of the all-terminal ground states of **edt** and **S-S**, **edt$_a$** and **S-S$_a$** respectively, and the transition states of the $Fe(CO)_3$ rotation, **edt$_b$** and **S-S$_b$** with free energies of the calculation with the TPSSTPSS functional reported.

rotors are identical. Both **edt** and **S-S** display a single ^{13}C NMR resonance at room temperature, which splits into two peaks with an integration of 2:4 at 0 °C for **edt** and -60 °C for **S-S**.

Computational investigation of both complexes has revealed a single ground state structure in which the six carbonyl ligands are in the eclipsed "all terminal" geometry,

edt$_a$ and **S-S$_a$** respectively, Figure IV-3. For both complexes, the single transition state of a fluxional process consists of the rotation of an iron in which one of the $Fe(CO)_3$ units is inverted, with one CO in a bridging or semi-bridging position between the two iron atoms, Figure IV-3. This transition state for the edt bridged complex, **edt$_b$**, is calculated to be 12.1 – 15.3 kcal/mol higher in energy than **edt$_a$**; the transition state for the disulfide complex, **S-S$_b$**, is 9.0 – 12.0 kcal/mol higher in energy than **S-S$_b$**, Table IV-2. With both iron units identical by symmetry, the rotation of either $Fe(CO)_3$ is the same. These are the simplest complexes with respect to fluxional processes, requiring the consideration of only a single $Fe(CO)_3$ rotation each. Therefore the only coalescence event observed by VT NMR is the splitting of the two equivalent apical and four equivalent basal COs when the $Fe(CO)_3$ rotation ceases.

*Fluxional Processes of **NH***

The ^{13}C NMR spectrum of **NH** at room temperature in the CO region reveals a single ^{13}C resonance at δ = 208.3 ppm for NH, Figure IV-4, indicating both $Fe(CO)_3$ units are freely rotating and the chair/boat interconversion is making both $Fe(CO)_3$ rotors equivalent. Upon cooling to 0 °C, the single peak separates into two resonances that integrate as three carbons each. At -60 °C the ^{13}CO resonances have split into three , observed at δ = 208.3, 208.2, and 206.8 ppm with relative intensities of three carbons at δ = 208.3, one carbon at δ = 208.2 and two carbons at 206.8. Four resonances are seen at -80 °C, which have relative intensities of 2:1:1:2. At this temperature, the apical and basal COs, both under

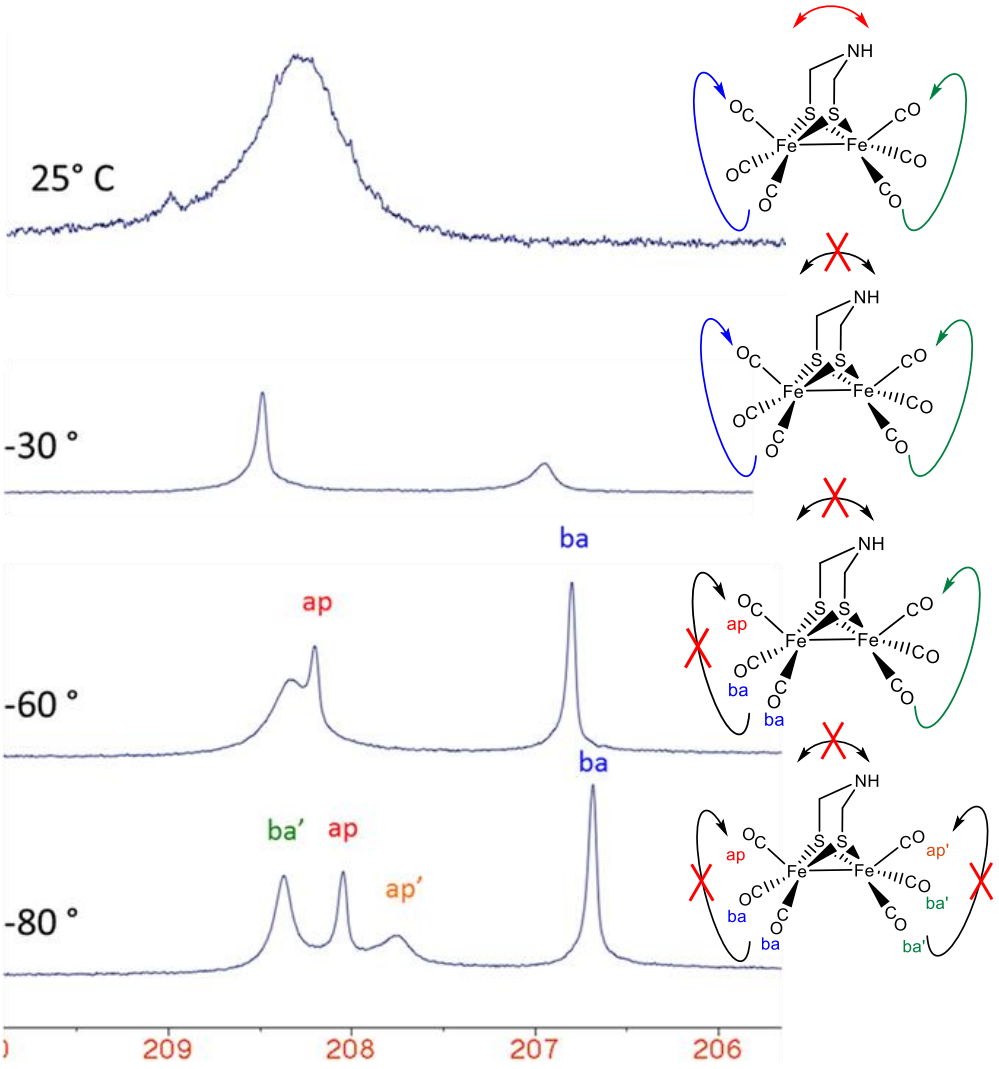

Figure IV-4. Variable temperature ^{13}C NMR spectra at 500 MHz in CD_2Cl_2 of **NH** in the low-field CO region with depiction of the fluxional processes at the various temperatures, reproduced with permission.[182]

and away from the bridgehead are distinct, indicating that all fluxional processes have ceased. This is shown in Figure IV-4, reproduced with permission from our paper.[182]

The computational investigation of the fluxional processes of **NH** located two ground state and five transition state structures, the greatest number for the series of (μ-SRS)$[Fe(CO)_3]_2$ complexes. The two ground state structures have the expected structure of the two FeS_2C_2N metallacycles, with one iron in the chair conformation and the other iron in the boat conformation. The six carbonyl ligands are in the "all terminal" geometry, with the only significant difference of the two structures being the position of the N-H hydrogen. If the hydrogen is in an axial position of the FeS_2C_2N metallacycle, pointed "up" away the iron atoms, the structure $\mathbf{NH_a'}$ is 3.4 - 4.7 kcal/mol higher in energy than if the hydrogen is axial, pointed "down" towards the iron atoms, $\mathbf{NH_a''}$, Figure IV-5. The lowest energy isomer $\mathbf{NH_a''}$ is set as 0.0 kcal/mol, with all other structure energies reported relative to it. Of the five transition states located, four are the transition states of the rotations of the $Fe(CO)_3$ moiety in which the iron is in the boat conformation, under the NH bridgehead, or in the chair conformation, away from the bridgehead. In both structures, the N-H may be either axial or equatorial. If the N-H is axial, Figure IV-5 (right side), there is a substantial difference in the rotation barrier of the two irons. The transition state

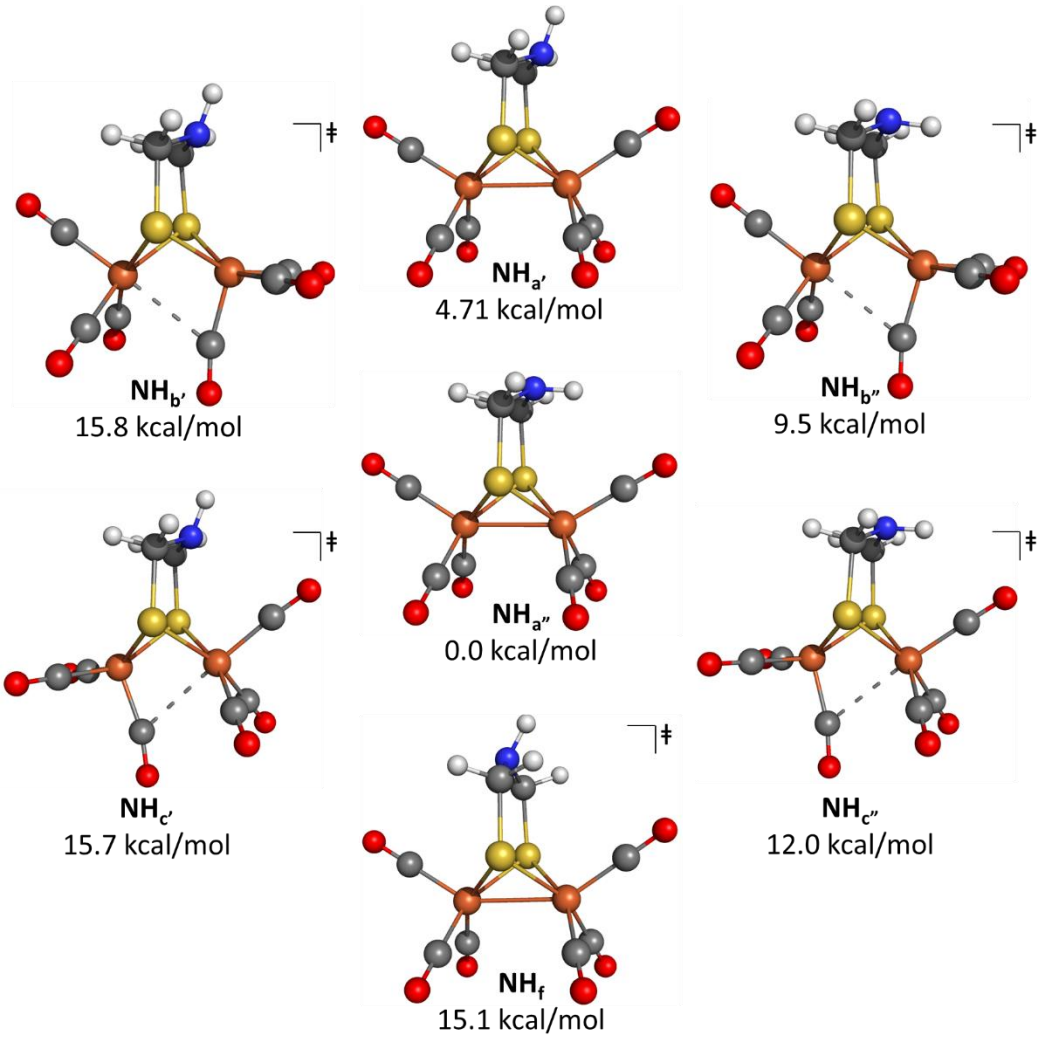

Figure IV-5. Calculated structures of the all-terminal ground states of **NH** with the N-H in the equatorial and axial positions**,** $\mathbf{NH_{a'}}$ and $\mathbf{NH_{a''}}$ respectively, and the transition states of the rotation of the iron in the boat conformation, $\mathbf{NH_{b'}}$ and $\mathbf{NH_{b''}}$, the rotation of the iron in the chair conformation, $\mathbf{NH_{c'}}$ and $\mathbf{NH_{c''}}$, and the ring flip, $\mathbf{NH_f}$, with free energies of the calculation with the TPSSTPSS functional reported.

corresponding to the rotation of the iron in the boat conformation, $\mathbf{NH_{b''}}$, is the lowest in energy at 9.5 – 12.9 kcal/mol, while the transition state structure corresponding to the chair

conformation, **NH$_{c}$"**, is higher in energy at 12.0 – 16.0 kcal/mol. If the N-H is equatorial, both iron units have a higher barrier to rotation, similar to each other at 15.8 – 17.9 kcal/mol for the boat conformation, **NH$_{b}$'**, and 15.7 – 17.9 for the chair conformation, **NH$_{c}$'**, Figure IV-5 (left side).

The fifth calculated transition state structure corresponds to the chair/boat interconversion, in which the C_2S_2 and C_2N planes are coplanar as the bridgehead moves from one side to the other. In this transition state geometry, the bridgehead amine remains pyramidal with amine inversion occurring either before or after the ring flip, Figure IV-5 (bottom). This final transition state was calculated to be 14.0 – 15.1 kcal/mol. Because the two rotational transition states and the ground state all containing the N-H in the axial position are higher in energy than their equatorial counterparts, they are not the most energetically preferred route to $Fe(CO)_3$ rotation. Thus, the chair/boat interconversion is predicted to be the highest energy process observed. This is in agreement with the split of the single NMR resonance observed at room temperature into two peaks of equal intensity at 0 °C. The two $Fe(CO)_3$ units are still rotating at -30 °C but because the bridgehead is locked on one side, the two rotors are slightly different, resulting in two NMR resonances of equal intensity, one for each $Fe(CO)_3$ rotor. The next highest energy process is the rotation of the chair iron, which corresponds to the splitting of a single three carbon peak into a 2:1 ratio at -60 °C. At this temperature, the only the $Fe(CO)_3$ moiety under the NH bridgehead continues to rotate. This rotation is the lowest energy process, but upon cooling **NH** to -80 °C, this motion is also frozen out.

Fluxional Processes of ***NMe***

The ^{13}C NMR spectrum of **NMe** at room temperature reveals a single resonance at δ = 208.4 ppm that, upon cooling to -40 °C, splits in a manner indicating a distinction in the two $Fe(CO)_3$ units, Figure IV-5 (A). However, unlike **NH**, which showed two signals of equal intensity, cooling the **NMe** sample reveals that the higher field resonances become distinct between -40 and -50 °C. In contrast the broad lower field resonance does not split apart, collapsing into the base line, until -80 °C. The resonances at δ = 208.0 and 207.1 ppm have relative intensities of 2:1, with the third peak having a relative intensity of 3. This may be seen in Figure IV-6 (A), reproduced with permission from reference [34]. This indicates that the rotation of one $Fe(CO)_3$ unit has ceased at the higher temperature, *ca.* -45 °C, while the other $Fe(CO)_3$ unit has a much lower rotation barrier , and remains in motion until cooled to temperatures lower than -80 °C. The sample of **NMe** could be further cooled in the solvent $CDFCl_2$ to temperatures as low as -120 °C. At that temperature, four ^{13}C resonances are seen at δ = 209.5, 208.4, 207.7, and 207.5 ppm, indicating that both $Fe(CO)_3$ units have ceased rotation.

The calculated ground state of **NMe** corresponds to the X-ray crystal structure in which the N-CH_3 is equatorial, **NMe$_a$'**, Figure IV-7.[96] The rotation of the iron in the boat conformation results in two possible transition states. The first, **NMe$_b$'**, in which the N-CH_3 is equatorial, has a higher energy, 11.4 – 15.6 kcal/mol, while the second, **NMe$_b$"**, in which the amine has inverted, has a lower energy, 6.6 – 11.6 kcal/mol, putting the methyl group in an axial position over the open site. In the ground state, the N-CH_3 inversion

barrier corresponding to the change from equatorial to axial, was found to be 1.1 kcal/mol, making this lower energy rotation easily accessible. A transition state for the rotation of the iron in the chair configuration was only located with the aminomethyl group in the equatorial position. **NMe$_{c'}$**, at 10.9 – 14.8 kcal/mol. The transition state for final fluxional process, the chair/boat interconversion, **NMe$_f$**, was located at a similar energy, 10.4 – 12.6

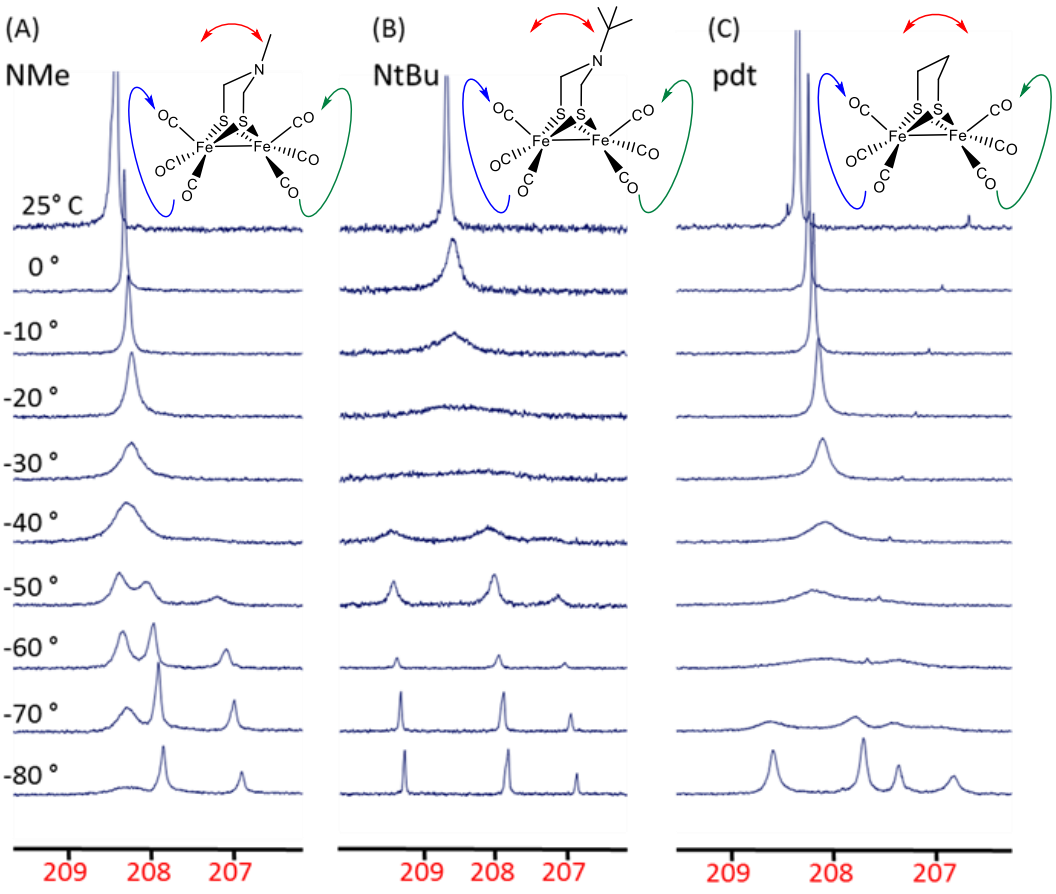

Figure IV-6. Variable temperature ^{13}C NMR spectra at 500 MHz in CD_2Cl_2 in the low-field CO region (A) **NMe**, (B) **NtBu**, and (C) **pdt**.[182]

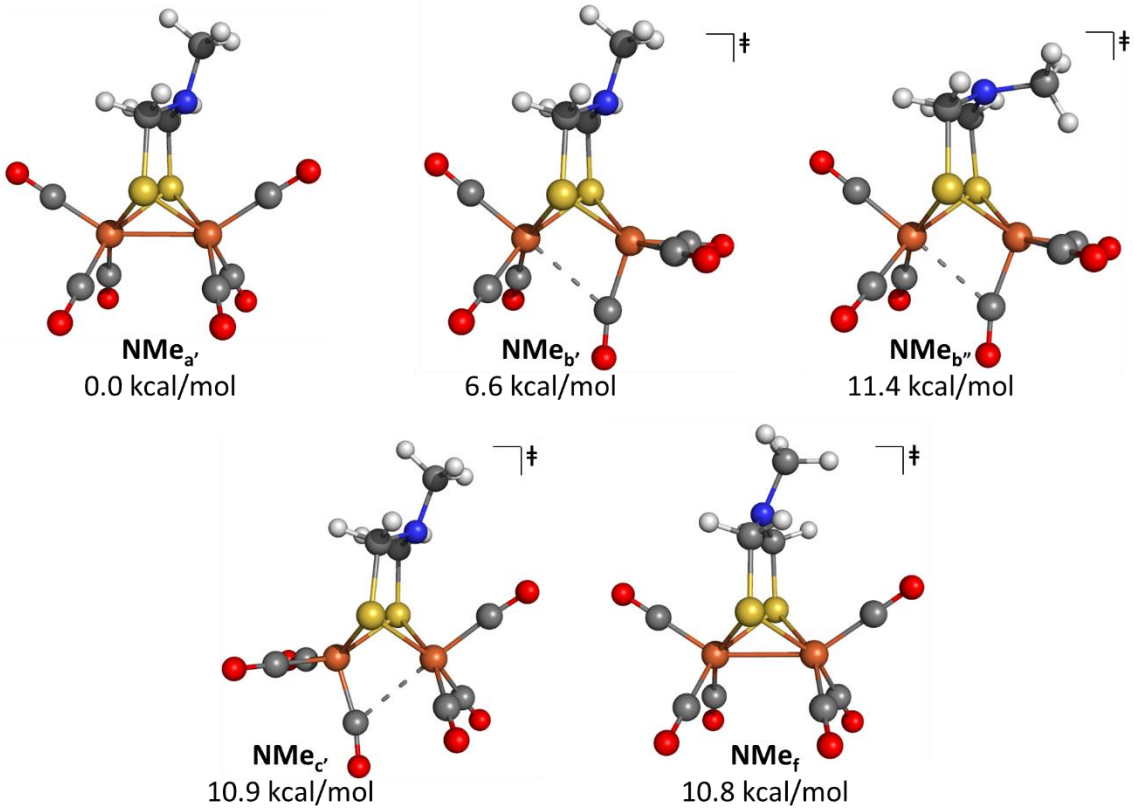

Figure IV-7. Calculated structures of the all-terminal ground state of **NMe** with the N-CH_3 in the equatorial position**, NMe$_{a'}$**, and the transition states of the rotation of the iron in the boat conformation, **NMe$_{b'}$** and **NMe$_{b''}$**, the rotation of the iron in the chair conformation, **NMe$_{c'}$**, and the ring flip, **NMe$_{f}$**, with free energies of the calculation with the TPSSTPSS functional reported.

kcal/mol. Thus, the $Fe(CO)_3$ rotation of one of the irons ceases at the same temperature as the ring flip, resulting in the single resonance splitting into three peaks concurrently as the NMR sample was cooled. This makes the NMR peaks with an intensity of 2:1 the basal and apical COs, respectively, of the iron in the chair conformation. The third peak is the $Fe(CO)_3$ unit under the N-CH_3 bridgehead, which is only split into two distinct

resonances at -120 °C as the low energy process for apical/basal site exchange is frozen out.

*Fluxional Processes of **NtBu***

The single ^{13}C CO resonance of **NtBu** at 25 °C, Figure IV-6 (B), broadens and collapses upon cooling to -30 °C. In a similar manner as observed with the **NMe**, the NMR spectrum at temperatures -40 °C and below shows three sharp resonances at δ = 209.3, 207.8, and 206.8 ppm, which integrate in a 2:3:1 pattern. This is consistent with the possibility that one $Fe(CO)_3$ unit is fixed while the other is still in flux, as is observed with **NMe**. However, as all three resonances remain sharp, with no hint of additional coalescence events even at temperatures as low as -80 °C, there is a second possibility. It may be that the fluxional processes all stop at the same temperature and that the NMR resonance of the apical CO of one iron overlaps with the basal COs of the other.

Computational investigation of **NtBu** found a single ground state, **NtBu$_a$**, and three transition states, one for each $Fe(CO)_3$ rotation as well as one for the ring flip, Figure IV-8. In all four structures, the bridgehead amine is in a pyramidal geometry with the *tert*-butyl group in the equatorial position, in agreement with the crystal structure. Attempts to optimize the all-terminal CO ground state or either bridging CO transition state with an axial *tert*-butyl group always resulted in an amine inversion, generating the structure with

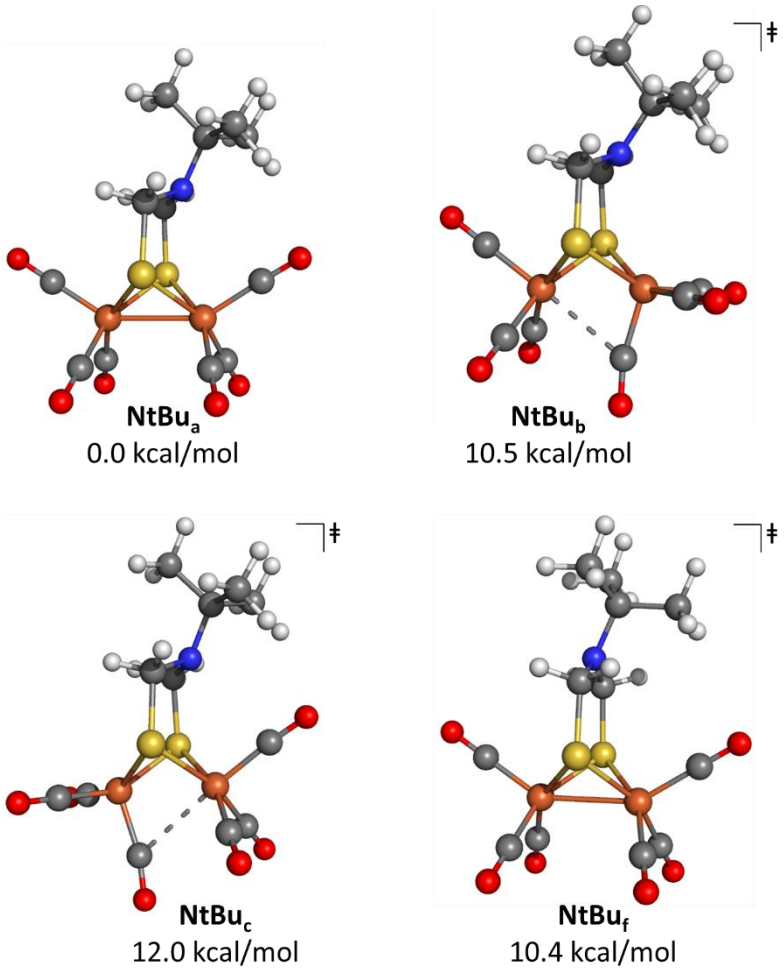

Figure IV-8. Calculated structures of the all-terminal ground state of **NtBu, NtBu$_a$**, and the transition states of the rotation of the iron in the boat conformation, **NtBu$_b$**, the rotation of the iron in the chair conformation, **NtBu$_c$**, and the ring flip, **NtBu$_f$**, with free energies of the calculation with the TPSSTPSS functional reported.

an equatorial *tert*-butyl. If the bridgehead is forced into the axial position, pointed towards the $Fe(CO)_3$ unit, there is no way to position the carbonyls such that they are not highly destabilized by the steric bulk of the *tert*-butyl group The transition state for the rotation

of the $Fe(CO)_3$ unit under the bridgehead, the iron in the boat configuration, **NtBu$_b$**, was found to be 10.5 – 16.9 kcal/mol. The rotation of the other $Fe(CO)_3$ moiety, **NtBu$_c$**, was found to have a higher transition state energy, at 12.0 – 15.6 kcal/mol. The transition state of the ring flip was calculated to be at a slightly lower energy than the $Fe(CO)_3$ rotations, with **NtBu$_f$** at 10.4 – 12.6 kcal/mol.

In the previous examples, **NH** and **NMe**, the difference in the energy barriers to rotation of the $Fe(CO)_3$ units, distinguished by the chair and boat conformations of the irons, resulted in two different coalescence events as the two sides of the molecule ceased rotation at different temperatures. However, experimental results from NMR spectroscopy clearly show a single coalescence event, Figure IV-6 (B). This apparent discrepancy can be accounted for by considering all of the fluxional processes of the **NtBu** molecule. With sufficient energy the **NtBu** molecule is in constant flux, as is observed at room temperature, with three fluxional processes making all six carbonyls equivalent at the NMR timescale. Upon cooling to the point that the rotation of the $Fe(CO)_3$ unit away from the bridgehead has ceased, there are still two fluxional processes available to the **NtBu**. If the rotation of the $Fe(CO)_3$ unit under the bridgehead is still possible, there is enough energy to flip the bridgehead as well. This chair/boat interconversion allows both iron atoms to spend some time in the boat conformation, which allows both $Fe(CO)_3$ units to rotate on the NMR timescale. With the lower energy rotation and the ring flip ceasing at roughly the same temperature, the single room temperature resonance splits into all four peaks at the same time as the apical and basal COs are frozen out and the $Fe(CO)_3$ units are distinguished by the bridgehead. That only three peaks are visible, in a 2:3:1 ratio, is

happenstance as the apical CO from one iron has the same chemical shift as the basal COs from the other.

*Fluxional Processes of **pdt** and **dmpdt***

The $Fe(CO)_3$ rotors of **pdt** also cease rotation at the same temperature, as the single room temperature resonance broadens and collapses at -60 °C and reforms into four distinct resonances at -80 °C, Figure IV-5 (C). The computational investigation of **pdt** was simplified by the presence of a methylene carbon at the bridgehead rather than an amine, eliminating the possibility of bridgehead inversion. Thus a single ground state structure, $\mathbf{pdt_a}$, and three transition states that correspond to the rotation of the iron in the boat configuration, $\mathbf{pdt_b}$, the rotation of the iron in the chair conformation, $\mathbf{pdt_c}$, and the chair/boat interconversion, $\mathbf{pdt_f}$, were located, Figure IV-9. Like the **NtBu** $Fe(CO)_3$ rotors, the rotation of the boat iron was found to be easier, with a calculated energy of $\mathbf{pdt_b}$ at 9.6 – 13.0 kcal/mol, than the rotation of the chair iron, with $\mathbf{pdt_c}$ calculated to be 12.4 – 16.1 kcal/mol. Also like the **NtBu**, the ring flip was found to have a transition state, $\mathbf{pdt_f}$, with a lower energy than the rotations, 8.8 – 10.7 kcal/mol. The much larger difference in the energies of the two rotors of **pdt** makes it clear that so long as the bridgehead can continue to flip, both sides continue to rotate until both the chair and boat

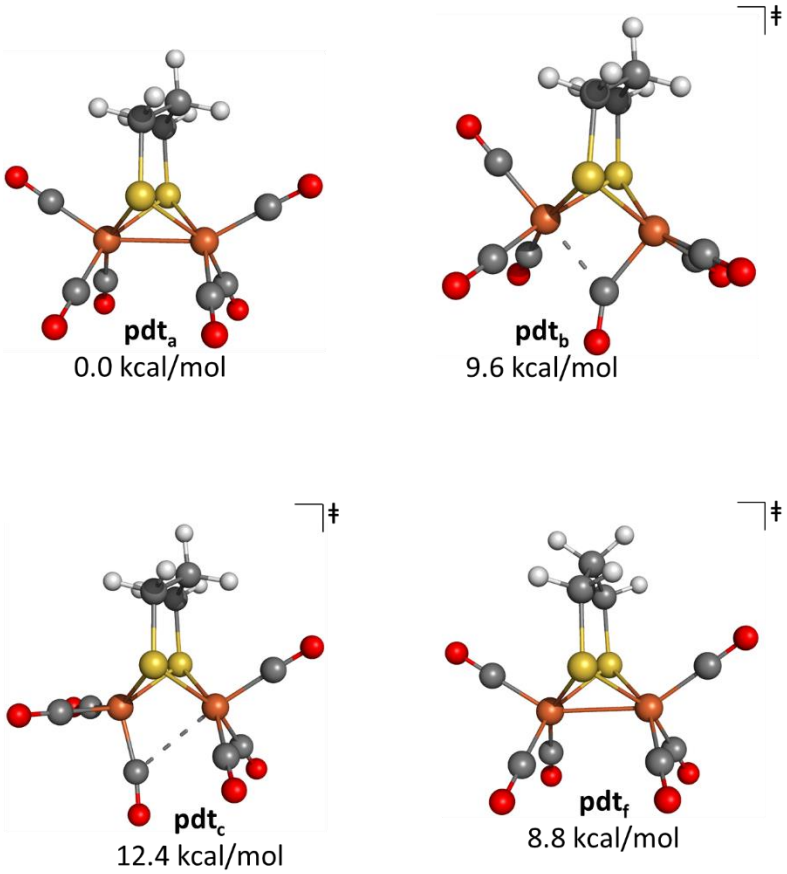

Figure IV-9. Calculated structures of the all-terminal ground state of **pdt, pdt$_a$**, and the transition states of the rotation of the iron in the boat conformation, **pdt$_b$**, the rotation of the iron in the chair conformation, **pdt$_c$**, and the ring flip, **pdt$_f$**, with free energies of the calculation with the TPSSTPSS functional reported.

rotations are frozen out. This leads to two equivalent apical COs and four equivalent basal COs, like **edt** or **S-S**, until the bridgehead stops flipping. Once that motion also ends, all four NMR peaks may be observed. For **pdt**, the second rotation and bridgehead flip are

both frozen out at a similar temperature, but the two NMR peaks with an intensity ratio of 2:4 can just be observed at -60 °C.

A more obvious example may be seen in the case of **dmpdt**. The ^{13}C CO resonance of **dmpdt** splits into two at low temperature, with an integration of 2:4. As the calculations

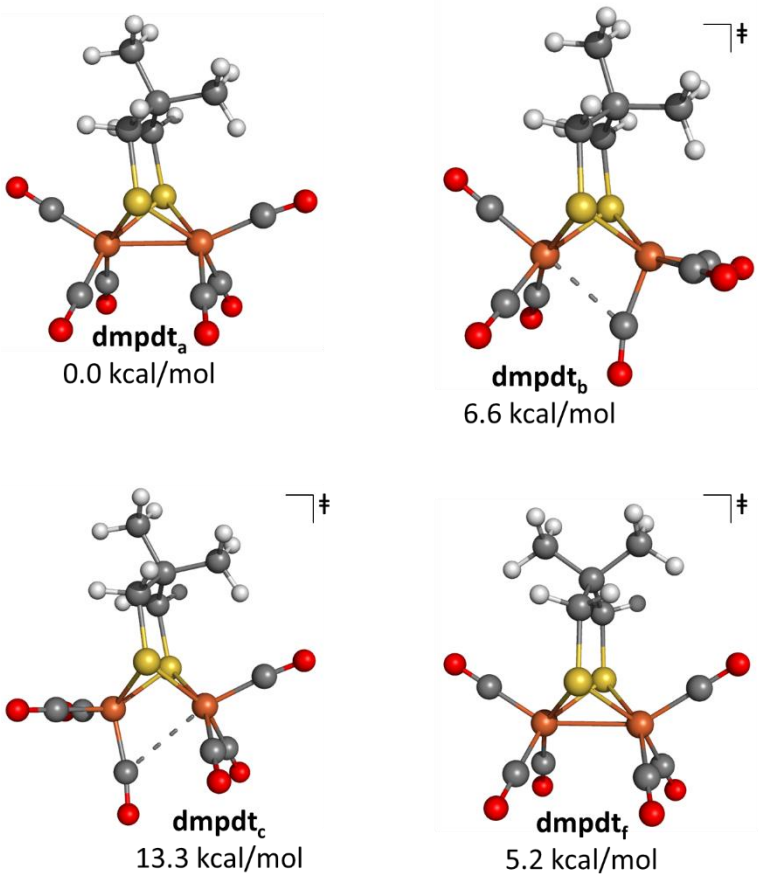

Figure IV-10. Calculated structures of the all-terminal ground state of **dmpdt, dmpdt$_a$**, and the transition states of the rotation of the iron in the boat conformation, **dmpdt$_b$**, the rotation of the iron in the chair conformation, **dmpdt$_c$**, and the ring flip, **dmpdt$_f$**, with free energies of the calculation with the TPSSTPSS functional reported.

show, with the same single ground state, **dmpdt$_a$**, and three transition states as **pdt**, one rotor (the iron in the chair configuration) has a much higher barrier, with **dmpdt$_c$** calculated to be 13.3 – 17.0 kcal/mol, than the other, Figure IV-10. The calculated transition state for the iron in the boat conformation, **dmpdt$_b$**, is only 6.6 – 9.6 kcal/mol. Thus, at a sufficiently low temperature (less than -87 °C), both irons will stop rotating and only the ring flip, with a transition state, **dmpdt$_f$**, calculated to be 5.2 – 6.1 kcal/mol, continues. Therefore, the two NMR resonances are assigned to the apical and basal COs on both $Fe(CO)_3$ units, as the chair/boat interconversion barrier in the **dmpdt** is too low to differentiate the two $Fe(CO)_3$ units, even cooling the complex to -120 °C.[197]

Effect of the Functional on Structure and Energy

There is little difference in the optimized structures of the (μ-SRS)$[Fe(CO)_3]_2$ complexes in either the ground or excited states. As a comparison, MPW1PW91 single point calculations were performed using the structures of the energy barrier to rotation of the $Fe(CO)_3$ unit that had been optimized with the B3LYP functional, and they were less than 0.2 kcal/mol different than the structures optimized with the MPW1PW91. The energy barrier of the ring flip was similar for each functional, typically with differences of less than 1 kcal/mol, with a maximum difference between functionals of 2.2 kcal/mol. The four functionals formed a trend, in which the TPSSTPSS functional was usually the lowest in energy and the ωB97xD functional was the highest. The B3LYP and MPW1PW91 functionals reported energies within 0.5 kcal/mol of each other and tended to be between the other functionals in energy. However, the TPSSTPSS functional did not always report

the lowest energy, the **NtBu** and **NH** complexes were exceptions. In fact, the TPSSTPSS functional reported an energy barrier ~1 kcal/mol higher than the other three functions for the **NH** complex. This complex was notable for being the only one to have all four functionals report greater energy barriers than the NMR spectroscopy experiment. When the five complexes with an FeS_2C_2X (X = NR, CR_2) metallacycle are ranked in order of increasing ring flip energy, the overall computational results are in agreement with the experimental data: **dmpdt** < **pdt** < **NMe** ≈ **NtBu** < **NH**.[182]

The energy barrier of the rotation of the $Fe(CO)_3$ unit as calculated by each functional followed a trend similar to the ring flip. The TPSSTPSS functional was consistently lower in energy than the B3LYP and MPW1PW91 functionals, which were energetically close to each other, with the B3LYP functional being between 0.2 and 1.1 kcal/mol higher in energy. The ωB97xD functional was the highest in energy for all seven complexes investigated. The difference between each functional is best seen in the degree of overestimation of each rotation barrier. The TPSSTPSS functional was a close match to the experimental energy values, typically within 1 kcal/mol. The B3LYP and MPW1PW91 functionals consistently overestimated the experimental energies by 1 – 2 kcal/mol, while the ωB97xD functional reported rotation barrier some 2.5 – 3.5 kcal/mol higher than the experimental data. These errors were systemic in nature, and a correction factor of 1.5 kcal/mol for the B3LYP and MPW1PW91 energies and 3.0 kcal/mol for the ωB97xD energies place all four functionals in close agreement with the energies obtained by NMR spectroscopy.

When ranked by increasing energy barriers to $Fe(CO)_3$ rotation, all four functionals predicted the order obtained experimentally with a single exception. The B3LYP functional reported the energy of the rotation of the **edt** complex, calculated to be 14.1 kcal/mol, as lower than the rotation of the **NtBu** complex, calculated to be 14.4 kcal/mol, when the experimental data and the three other functionals are in agreement that the **edt** complex has a higher barrier of rotation. That all four functionals were essentially correct in ranking the energy barriers of the series of $(\mu\text{-SRS})[Fe(CO)_3]_2$ complexes indicates that the fluxional processes of these complexes are well-described by Density Functional Theory.

Conclusions

The Density Functional Theory study of the intramolecular fluxional processes of a series of $(\mu\text{-SRS})[Fe(CO)_3]_2$ complexes was one portion of a paper in which these compounds were also investigated by VT NMR spectroscopy and cyclic voltammetry.[182] The goal was to answer the question of how might the bridging ligand affect their fluxional processes and proton reduction capacities through changing the bridgehead atom to carbon or nitrogen or increasing the steric bulk at that position. The calculations I provided reproduced the structures of the ground states of each complex as well as the transition states that correspond to each fluxional process. The relative energies of those transition states provided a computational basis for confirming the assignment of the energy barriers of those processes as determined by VT NMR spectroscopy.

By utilizing four different functionals,[190] I was able to determine that the choice of functional, while important, did not have an effect on the ability of DFT to match the experimental energy barrier trends across the series of complexes. The major difference in the functionals was seen to be a systematic offset in the energy of the rotational barrier in all of the complexes. Finally, with the positive correlation between experimental and calculated numbers, I was able to provide estimations of the energies of processes that could not be observed by NMR spectroscopy, such as the ring flip of **dmpdt** or the rotation barriers of the $Fe(CO)_3$ units in which the iron is in the chair conformation of the FeS_2C_2X metallacycle, and clarify NMR spectroscopic results that were ambiguous, such as the overlapping resonances of the **NtBu** complex.

CHAPTER V

A DENSITY FUNCTIONAL THEORY INVESTIGATION OF THE MECHANISM OF CARBON MONOXIDE INDUCED REDUCTIVE ELIMINATION OF A DISULFIDE IN AN N-HETEROCYCLIC CARBENE (NHC) / THIOLATE DINITROSYL IRON COMPLEX (DNIC)*

Preface

The chemistry of dinitrosyl iron complexes (DNICs) has been an area of interest to the Darensbourg research group in the past several years.[200-203] Recently, we have taken our investigations in a more fundamental direction, prompting a study of the processes involved in the changes to the reduction level of these complexes. When the reduction of an oxidized DNIC was found to be induced by CO(g), members of the Darensbourg group began a study of the kinetics of the reaction. With my own interests in computational chemistry and my investigations of complexes containing iron-bound carbon monoxide, nitric oxide, and cyanide; Chapter III, I joined the DNIC effort. Through the use of DFT a plausible mechanism for this unusual reaction was derived. My contributions are described in the following co-authored manuscript: "Carbon Monoxide Induced Reductive

*This chapter is reproduced in part in permission from Pulukkody, R.[†]; Kyran, S. J.[†]; Bethel, R. D.[†]; Hsieh, C.-H.; Hall, M. B.; Darensbourg, D. J.; Darensbourg, M. Y.; Carbon Monoxide Induced Reductive Elimination of Disulfide in an N-Heterocyclic Carbene (NHC)/Thiolate Dinitrosyl Inron Complex (DNIC). *Journal of the American Chemical Society*, **135**, 8423-8430 (2013). Copyright 2013 ACS Publications

Elimination of Disulfide in an N-Heterocyclic Carbene (NHC)/ Thiolate Dinitrosyl Iron Complex (DNIC)" Pulukkody, R.†; Kyran, S. J.†; Bethel, R. D.†; Hsieh, C.-H.; Hall, M. B.; Darensbourg, D. J.; Darensbourg, M. Y.; *Journal of the American Chemical Society*, **135**, 8423-8430 (2013).[204]

Introduction

An Introduction to Dinitrosyl Iron Complexes (DNICs)

Though it has been considered a toxic pollutant for many years, nitric oxide has been more recently found to play a key role in biochemistry as a small molecule messenger.[205,206] The functions of NO in humans may be regulatory, as with its ability to regulate of blood pressure and smooth muscle relaxation as well as protective, as it is known to take part in an immune response. Nitric oxide is produced *in vivo* by a family of enzymes known as Nitric Oxide Synthase (NOS), which convert L-arginine to L-citrulline, releasing an NO molecule.[206] However, as NO is a radical whose lifetime in the cellular environment is on the order of 2 ms to 2 s, the transport and storage of this molecule are of interest.[207]

It has been observed that the presence of NO can degrade iron-sulfur clusters in proteins.[208] One product of this degradation is a protein-bound $Fe(NO)_2$ unit, the dinitrosyl iron complex (DNIC).[209] These complexes were first observed in the 1960s, when the livers and other organs of rats that had been fed carcinogens were found to have a characteristic signal in the EPR spectrum at g = 2.03.[210,211] This signal is ubiquitous for DNICs with S

= ½. However, in addition to the multiple redox levels possible for iron, both the oxidized NO^+, nitrosyl, species (isoelectronic with CO) and reduced NO^-, nitroxyl, species (isoelectronic with O_2), as well as the neutral ·NO radical, are readily accessible. As the redox levels of iron and NO are similar, orbital interactions lead to "non-innocence" of the NO ligand and thus determination of the oxidation states of the components of the $Fe(NO)_2$ unit is non-trivial. In an effort to allow for the simple identification and classification of the overall redox level of metal complexes with nitric oxide ligands,

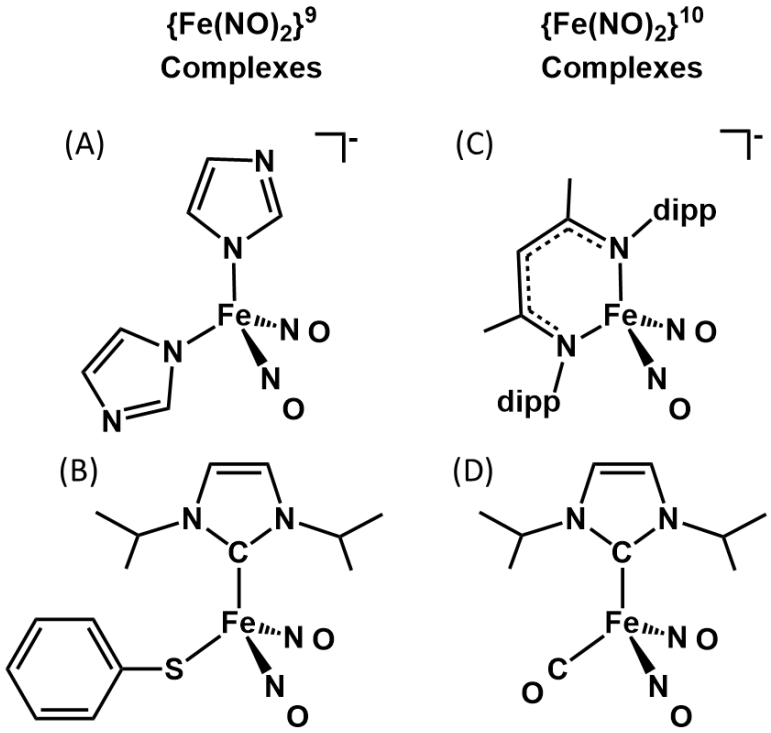

Figure V-1. Depiction of (A)[214] anion and (B)[200] neutral oxidized dinitrosyl iron complexes that are EPR active as well as the EPR silent, reduced, (C)[215] anionic and (D)[200] neutral DNICs.

Enemark and Feltham devised a notation system in which the sum of metal d electrons and NO π* electrons is written as a superscript outside a pair of braces that contain the $M(NO)_x$ unit in question, where M is the metal and $_x$ is the number of NO ligands.[176] In this scheme, the S = ½ DNIC is written $\{Fe(NO)_2\}^9$. Depending on the other ligands coordinated to the iron, this complex may be reduced to the S = 0, $\{Fe(NO)_2\}^{10}$, species.

In the past decade, numerous small molecule dinitrosyl iron[212,213] complexes have been synthesized in an effort to understand the chemistry of this system. These complexes have been synthesized in both the oxidized and reduced states, as seen on the left and right respectively of Figure V-1.[200,214,215]

Summary of the Paper

Reduction of the oxidized, $\{Fe(NO)_2\}^9$, DNIC in the form $(RS)_2Fe(NO)_2^-$ to the $\{Fe(NO)_2\}^{10}$ species is known to require harsh conditions, with both a strong reducing agent, such as sodium-biphenyl, and a good incoming nucleophile, such as phosphine. In

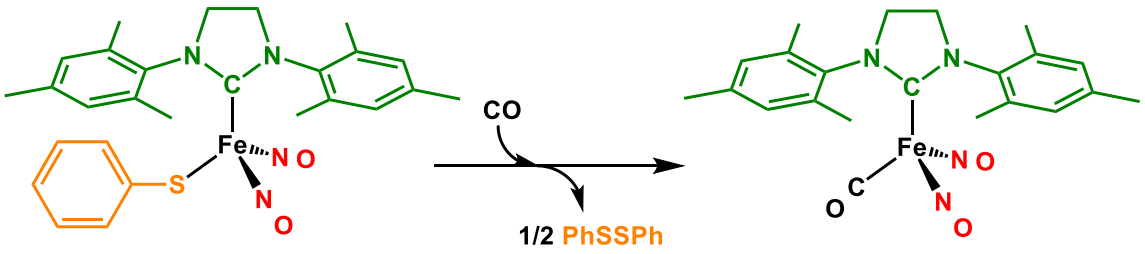

Figure V-2. Conversion of oxidized (NHC)(SR)$Fe(NO)_2$, **1**, to (NHC)(CO)$Fe(NO)_2$, **2**, in the presence of CO

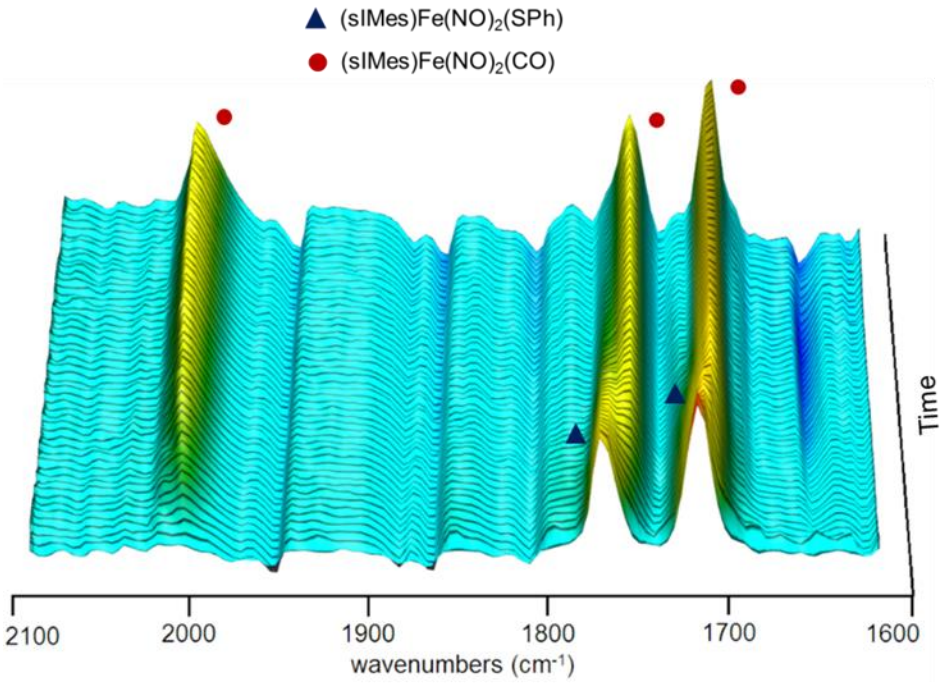

$$\text{Rate} = k[\text{DNIC}]^1[\text{CO}]^1$$

Figure V-3. Three-dimensional stacked plot of the reaction of complex **1** with CO(g) at 333 K in toluene, taken with permission from our paper[204] and overall rate expression for the production of **2**

contrast, the reduction of (NHC)(SR)Fe(NO)$_2$, **1**, NHC = 1,3-bis(2,4,6-trimethylphenyl)imidazolidin-2-ylidene, SR = thiophenyl, to (NHC)(CO)Fe(NO)$_2$, **2**, was discovered by Chung-Hung Hsieh and Randara Pulukkody to proceed without external reductant, requiring only the presence of CO(g) as the incoming ligand and generating phenyl disulfide as the oxidized byproduct, Figure V-2.[204] As the rate of conversion of **1** to **2** is amenable to kinetic monitoring, a series of measurements were performed by Samuel Kyran, in a toluene solution via *in situ* IR, Figure V-3. Under a constant

concentration of CO(g), the reaction was found to be first order in the DNIC starting material, **1**. By varying the pressure of CO(g), the reaction was monitored at various levels of CO concentration, with the finding that the formation of **2** is first order in CO as well, giving an overall bimolecular rate expression, first order in both CO and DNIC, Figure V-3. The activation parameters were determined by Eyring analysis and found to have values for $\Delta H^{\ddagger}$ of +7.80 ± 0.16 kcal/mol and $\Delta S^{\ddagger}$ of -45.0± 0.5 e.u., making $\Delta G^{\ddagger}$ +21.2 ± 0.2 kcal/mol at 298.15 K. With a small, positive enthalpy of activation and a large, negative entropy of activation, the Eyring analysis is indicative of an associative mechanism, consistent with the second order rate law.

Preliminary investigations of the reduction of **1** have been performed by Randara Pulukkody, using better donor ligands: triphenylphosphine, PPh_3; trimethylphosphine, PMe_3; and trimethylphosphine, $P(OMe)_3$.[204] Triphenylphosphine was not observed to react with **1**, likely due to its excessive steric bulk, leading us to investigate the smaller phosphine and phosphite reagents. In an unexpected development, the strongest σ-donor ligand, PMe_3, was the slowest to react with **1**, with the rate of reaction with $P(OMe)_3$, a ligand intermediate in σ-donor strength, falling between the phosphine and carbonyl reaction rates. The CO-induced reduction of **1** was then investigated by DFT in an effort to determine a mechanism consistent with both the second order rate law and Eyring

activation parameters. This mechanism should also explain the inverse relationship between the rate of reaction and the σ donor strength of the incoming ligand.

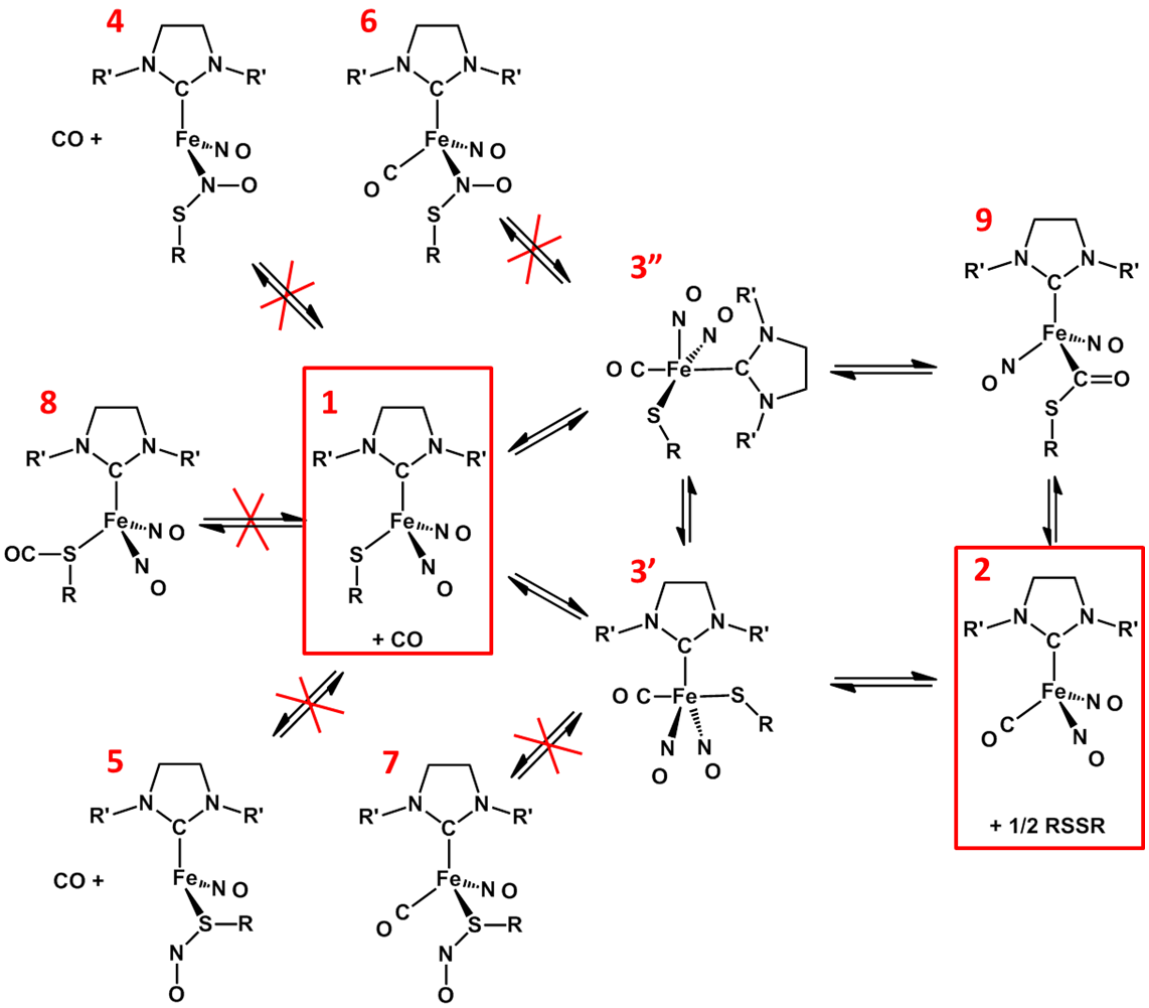

Figure V-4. Structures derived by DFT and explored as intermediates in CO addition to complex **1**. In DFT study, R = R' = Me; in kinetics study, R = Ph, R' = Mes.

*Computational Investigation of the Mechanism of CO Induced Reduction of **1***

Density Functional Theory was utilized in the study of the mechanism of the CO-induced reduction of **1**. As described in Chapter II, all calculations were performed using the BP86 functional[164,165] with the 6-311+G(d,p) basis set[156,157] on all atoms. These were selected for use in this study for their effectiveness at modeling DNICs, as determined by Brothers, *et al*.[166] The strength of DFT is the ability to locate the structures of all intermediates and transition states along a presumed reaction profile. However, in order to certain that the mechanism is correct, all possible reaction pathways must be analyzed. As in experimental studies of a mechanism, the exact mechanism can never be known with absolute confidence; a mechanism may never be proven, it can only be disproved. In fact, two mechanistic pathways, similar in energy, were identified in which the oxidized DNIC first attacks a CO molecule, generating an intermediate structure with a five-coordinate iron. This was followed by either homolytic Fe – S bond cleavage or thiolate migration onto the carbonyl ligand, then homolytic C – S bond cleavage, Figure V-4. In both mechanisms, the product **2** is generated along with a thiyl radical, two of which must combine to form a disulfide. The calculated energies are all reported relative to **1** and a free CO throughout this chapter, with the electronic, free, and enthalpic energies of all stable and pseudostable complexes, described below, provided in Table V-1. The relevant metric parameters of the calculated structures along the reaction profile are provided in Table V-2.

Results and Discussion

A Comparison of the Experimental and Calculated Structures of (NHC)(SR)Fe(NO)$_2$, ***1****, and (NHC)(CO)Fe(NO)$_2$,* ***2****.*

The complexes (NHC)(SR)Fe(NO)$_2$, **1**, and (NHC)(CO)Fe(NO)$_2$, **2**, where NHC = sIMes (1,3-bis(2,4,6-trimethylphenyl)imidazolidin-2-ylidene) and SR = SPh (phenylthiolate) for

Table V-1. Calculated electronic energy, free energy, and enthalpies of converged transition states and minima in Figure V-3

Species[a]	Electronic Energy (kcal/mol)	Free Energy (kcal/mol)	Enthalpy (kcal/mol)
1+CO	0.0	0.0	0.0
2+½RSSR	-19.6	-12.8	-18.5
3'	1.3	14.9	2.3
3"	1.3	15.2	2.4
{4+CO}[b]	35.9	37.2	34.7
{5+CO}	36.6	36.2	35.7
6	11.3	22.6	11.9
7	14.2	24.0	14.8
9	-0.8	10.4	0.4
[1-3']‡	9.5	19.2	9.7
[1-3"]‡	8.6	19.6	9.1
[3"-9]‡	4.3	18.4	4.7
[9-2]‡	5.9	17.0	6.4
[3'-2]‡	10.3	21.2	10.9

[a]All energies relative to the sum of **1** and a free CO ligand, which was defined as 0.0 kcal/mol. [b]Intermediates **4** and **5** were only located by freezing the S-N bond of the RSNO as described in the text.

the experimental structure, were optimized in the gas phase, both as the full experimental structures and in a truncated form, where NHC = sIMe (1,3-dimethylimidazolidin-2-ylidene) and SR = SMe (methylthiolate). A comparison of the metric parameters of the full and truncated optimized geometries with the X-ray crystal structures of **1** and **2** shows that there is little difference in the iron coordination environment between the full and truncated structures, Table V-1.[204] As observed by Brothers, *et al.* in a DFT study that benchmarked a series of functionals and basis sets with multiple DNICs, the structures optimized with the BP86/6-311+G(d,p) are consistent with the experimental structures.[166] However, the truncation of the mesityl groups of the NHC and phenyl group of the thiolate reduces the number of basis functions by over 50%, making the calculations much more efficient. The truncated structure does show that the Fe – N – O angles of the oxidized DNIC, **1**, are slightly more bent, 171.9° and 169.6°, than the same angles of the reduced DNIC, **2**, 171.4° and 174.9°, and in both instances are oriented towards each other in the "attracto" conformation seen in nearly all DNICs, while important distances such as the

Table V-2. Metric parameters of all calculated transition states and minima in lowest energy reaction coordinates.

Bond Length (Å)	1	[1-3']‡	3'	[3'-2]‡	[1-3'']‡	3''	[3''-9]‡	9	[9-2]‡	2
Fe-C(CO)	---	2.452	1.852	1.817	2.376	1.838	1.789	1.965	1.846	1.797
Fe-S(SR)	2.225	2.334	2.346	2.745	2.343	2.341	2.455	3.114	3.379	---
Fe-C(NHC)	2.005	2.042	2.012	2.004	1.974	1.997	2.058	2.019	2.010	1.978
Fe-N1	1.661	1.662	1.704	1.772	1.668	1.717	1.695	1.657	1.657	1.664
Fe-N2	1.658	1.672	1.76	1.698	1.676	1.774	1.737	1.663	1.668	1.662
N1-O1	1.185	1.184	1.184	1.181	1.187	1.189	1.186	1.181	1.180	1.186
N2-O2	1.190	1.184	1.193	1.194	1.188	1.197	1.193	1.186	1.164	1.184

Bond Angle (°)	1	[1-3']‡	3'	[3'-2]‡	[1-3'']‡	3''	[3''-9]‡	9	[9-2]‡	2
N1-Fe-N2	118.4	117.5	117.7	115.5	111.4	103.1	109.5	120.8	117.6	119.4
Fe-N1-O1	171.9	166.2	158.2	141.5	166.5	143.3	154.6	172.6	175.2	171.4
Fe-N2-O2	169.6	161.8	145.9	160.6	156.8	142.8	143.6	170.9	167.8	174.9
C(NHC)-Fe-S	102.6	83.5	79.7	77.9	80.9	77.7	84.2	---	---	---
C(CO)-Fe-S	---	164.1	168.9	169.5	80.0	86.8	64.0	---	---	---
C-Fe-C	---	81.5	89.2	91.8	157.0	158.0	146.7	103.7	109.6	97.3
Fe-C-O	---	134.8	174.7	174.9	137.2	178.4	167.5	130.6	162.2	176.6

Table V-3. Ball and stick representations and metric parameters of experimental and calculated structures of complexes **1** and **2**. The calculated structures include both the full structure and truncated structure, in which the mesityl and phenyl groups are replaced with methyl groups

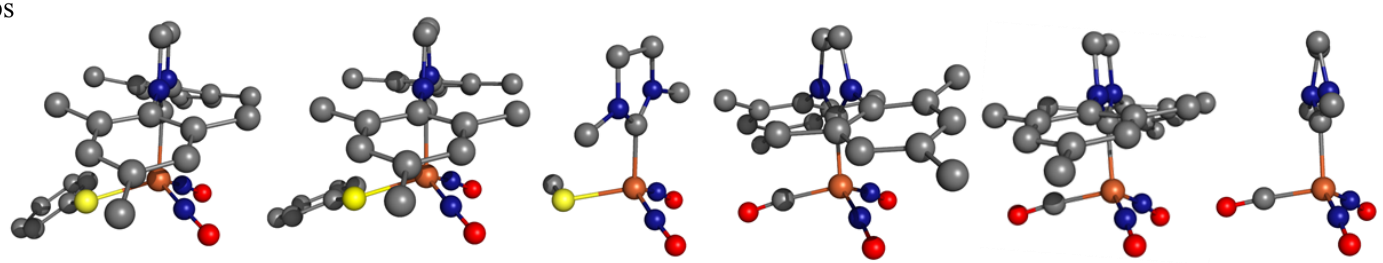

Bond Length (Å)	Experimental[a]	Calculated (Full)[a]	Calculated (Truncated)[a]	Experimental[b]	Calculated (Full)[b]	Calculated (Truncated)[b]
Fe-S(SR)	2.243(1)	2.241	2.225	-	-	-
Fe-C(CO)	-	-	-	1.771(2)	1.793	1.797
Fe-C(NHC)	2.048(1)	2.011	2.005	1.998(2)	1.975	1.978
Fe-N(1)	1.677(1)	1.660	1.661	1.658(2)	1.664	1.664
Fe-N(2)	1.666(1)	1.659	1.658	1.707(2)	1.664	1.662
N(1)-O(1)	1.174(5)	1.186	1.185	1.174(1)	1.183	1.186
N(2)-O(2)	1.184(5)	1.183	1.190	1.163(1)	1.183	1.184

Bond Angle (°)	Experimental[a]	Calculated (Full)[a]	Calculated (Truncated)[a]	Experimental[b]	Calculated (Full)[b]	Calculated (Truncated)[b]
Fe-N(1)-O(1)	168.4(1)	166.5	171.9	171.5(2)	172.1	171.4
Fe-N(2)-O(2)	168.5(1)	169.4	169.6	173.8(2)	172.3	174.9
N(1)-Fe-N(2)	115.3(2)	115.2	118.4	116.6(1)	119.7	119.4
C-Fe-S	109.1(1)	106.4	102.6	-	-	-
C-Fe-C	-	-	-	101.8(1)	99.2	97.3

[a]Structures and parameters of (NHC)(SR)Fe$(NO)_2$,**1.** [b]Structures and parameters of (NHC)(CO)Fe($(NO)_2$, **2**.

Fe – S, Fe – C(NHC), and Fe – C(CO) bonds show only minor deviations between the calculated and experimental structures. The greatest difference between the truncated and full calculated structures are the C(NHC) – Fe – S and C(NHC) – Fe – C(CO) angles, which are several degrees larger in the truncated structure (102.6° vs. 106.4° and 97.3° vs. 99.2° respectively), likely due to the loss of steric bulk that would otherwise push the other ligands towards each other and away from the NHC. However, while the mesityl groups of the sIMes in the experimental structure shield the iron center from incoming ligands on one side, the actual steric bulk is more than 3.5 Å distant from the iron, reducing the ligand's impact on coordinated ligand geometries to minimal. In addition to the subtle differences in coordination geometry, there is a change from an aryl thiolate to an alkyl thiolate in the truncated structure. This was examined experimentally. Unpublished results by Randara Pulukkody have shown that the mercaptoethane derivative of **1**, $(sIMes)(SCH_2CH_3)Fe(NO)_2$, also reacts with CO(g) to generate the reduced product **2**. Finally, the $Fe(NO)_2$ moiety is well-known to be redox non-innocent with the infrared stretching frequencies of the diatomic ligands acting as a sensitive reporter on the electron density in the Fe-NO π-system. As seen in Table V-3, the calculated ν(NO) bands of **1** are a near perfect match to the experimental data, while the calculated ν(CO) and ν(NO) bands of **2** are within the expected range, < 25 cm^{-1} from the experimental values. This provides evidence that the DFT calculations accurately reproduce the overall electronic structure of the DNIC complexes in this study.

Investigation of the Mechanism of the Reduction of the DNIC: Possible Intermediates Prior to Fe-CO Bond Formation

Although the rate determining step was experimentally determined to be first order in both CO and DNIC, Figure V-3, it was proposed that a site may be opened up by a process in which an iron-bound S-nitrosothiol (Fe-RSNO) exists in an equilibrium with the starting material, **1**. This would open up a site on the 17-electron tetrahedral iron and, depending on the route by with the RSNO is produced, could yield either the N-bound or S-bound forms. Therefore, both nitrosyl insertion into the Fe – S bond, forming the N-bound RSNO (intermediate **4**), and nitrosyl migration onto the thiolate, producing the S-bound RSNO (intermediate **5**), were examined, Figure V-5. Although the structures shown are the most stable calculated forms of each, neither is stable with respect to the starting material **1**, and

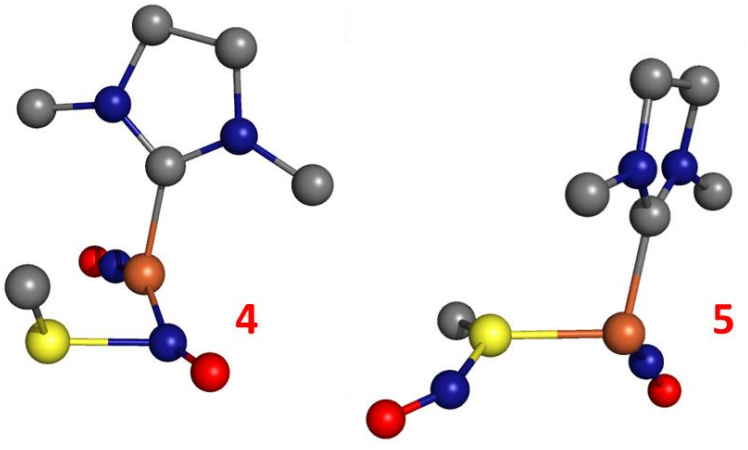

Figure V-5. Calculated structures of the three-coordinate iron intermediates formed by NO insertion into the Fe-SR bond (**4**) or NO migration onto the SR (**5**)

will revert to **1** upon reoptimization unless the N-S distance of the RSNO is constrained. These intermediates are far too high in energy, more than 36 kcal/mol when compared to **1**, and thus they are not reasonably in the reaction pathway.

A third possiblity considered was thiolate S/CO adduct formation, intermediate **8**, followed by CO insertion between the sulfur and iron. However, positioning a CO at the sulfur of the Fe – SR produced niether S-CO nor Fe-C(=O)SR interactions and no stable or constrained minimum could be located.

Five-Coordinate Intermediates Derived from Fe-CO Bond Formation

With the failure to locate an intermediate structure in an equilibrium with **1**, which may be more easily attacked by the poor nucleophile CO, direct coordination of the CO to Fe resulting in a five-coordinate 19 electron iron was examined. A trigonal bipyramidal

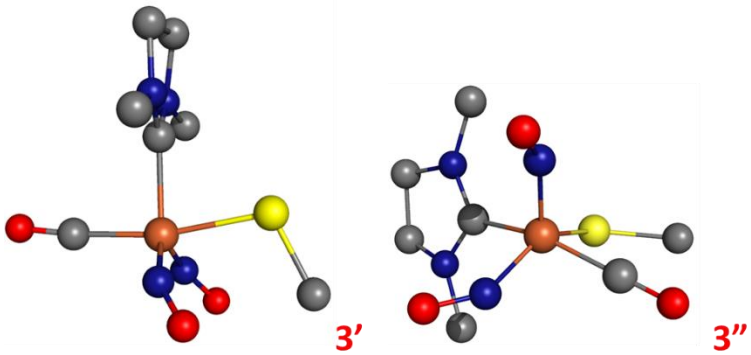

Figure V-6. Calculated structures of the two lowest energy five-coordinate iron intermediates formed by CO addition across from the SR (**3'**) or NHC (**3"**)

Table V-4. Isomers of the five-coordinate intermediate, **3**, grouped by axial ligands in a TBP structure, which are defined as the longest L-Fe-L angle.

Axial Ligand Set	CO/SMe	CO/NHC	NO/SMe	NHC/SMe	NHC/NO
Free Energy[a]	0.00	0.22	0.85	1.50	2.75
Bond Length (Å)	CO/SMe	CO/NHC	NO/SMe	NHC/SMe	NHC/NO
Fe-C(CO)	1.852	1.838	1.788	1.767	1.786
Fe-C(NHC)	2.012	1.997	2.011	1.978	2.004
Fe-N1	1.760	1.774	1.751	1.749	1.748
Fe-N2	1.704	1.717	1.720	1.734	1.727
Fe-S	2.346	2.341	2.370	2.376	2.381
Bond Angle (°)	CO/SMe	CO/NHC	NO/SMe	NHC/SMe	NHC/NO
Fe-N1-O1	145.9	142.8	148.1	150.4	150.6
Fe-N2-O2	158.2	143.3	157.0	164.7	154.8
N1-Fe-N2	117.7	103.1	104.9	121.0	105.5
τ Value	0.75	0.31	0.74	0.52	0.77

[a]Free energy is defined with **3'** set to 0 kcal/mol

complex of the formula $ML_2L'L''L'''$ could exist in seven possible geometric isomers. Optimizations of all seven possibilities found five stable isomers with similar free energies, all within 3 kcal/mol of each other, Table V-4. The two isomers with any of the π-acidic ligands (NO or CO) in both axial positions underwent Berry pseudorotations to generate lower energy isomers. The most stable isomer of **3**, **3'**, Figure V-6, has the carbonyl and thiolate ligands in the axial position of a largely trigonal bipyramidal structure, $\tau = 0.75$. As expected, the Fe – C – O angle is linear, 174.7°, but the two Fe – N – O angles are quite significantly bent, 158.2° and 145.9°. This bending is caused by the excess electron density on the 19 electron iron being pushed onto the NO ligands,

reducing them from a more neutral $NO^{\cdot}$ to a more negative NO^{-}. The increased electron density on the iron is also seen in the elongation of the Fe – S bond to 2.346 Å, as well as elongations of the Fe – N (NO) bonds, with one increasing by ~0.045 to 1.704 Å and the other by ~ 0.10 to 1.760 Å. Another isomer of **3**, **3"**, Figure V-6, is only 0.22 kcal/mol less stable than **3'**. The geometry of **3"** is largely square pyramidal, $\tau = 0.31$, with the CO and NHC ligands comprising the largest angle across the iron, in what would be the axial positions if the structure were trigonal bipyramidal. The metric parameters of this intermediate are similar to **3'**, with a linear Fe – C – O, 178.4°, two significantly bent Fe – N – O angles, at 142.8° and 143.3° and elongated Fe – S (2.341 Å) and Fe – N (1.717 and 1.774 Å) bonds. The three other isomers of **3** are not significantly higher in energy, ranging from 0.85 to 2.75 kcal/mol above **3'**.

*Transition States Leading to the Formation of **3'** and **3"***

The search for transition states leading to the formation of **3'** and **3"**, **[1-3']**‡ and **[1-3"]**‡ respectively, was carried out by performing a relaxed coordinate scan along the Fe – C(CO) bond, using the appropriate five-coordinate intermediate as a starting geometry. By reoptimizing the full structure while elongating the Fe – C bond by 0.1 Å repeatedly, a structure was located near the appropriate Fe – C distance for a transition state. A Berny calculation then located the transition states for CO addition to the DNIC, **[1-3']**‡ and **[1-3"]**‡, Figure V-7. The addition of a fifth ligand to $(NHC)(SR)Fe(NO)_2$ can occur on any of the four faces of the tetrahedron, yielding a structure with the incoming CO ligand in an axial position, with the DNIC ligand across from the face of the tetrahedron that was

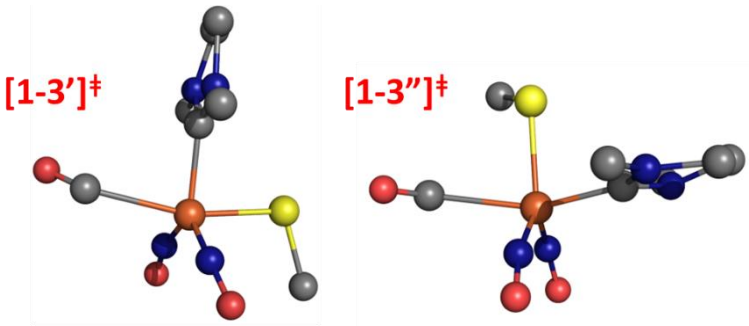

Figure V-7. Calculated structures of the transition states leading to the five-coordinate iron intermediates formed by CO addition across from the SR (**[1-3']**‡) or NHC (**[1-3"]**‡)

attacked in the other axial position. Thus, the CO would be anticipated to approach the DNIC across from the thiolate, **[1-3']**‡, or NHC, **[1-3"]**‡, as no stable intermediate could be located with both CO and NO in the axial positions of the five-coordinate intermediate.

Upon examination of the two transition states, an immediately apparent feature is the long Fe – C(CO) interaction, 2.452 Å for **[1-3']**‡ and 2.376 Å for **[1-3"]**‡, with a severe bend in the Fe – C – O angle, 134.8° and 137.2° respectively. Such a sharp bend is atypical for the usually linear metal-carbonyl bond unless the CO bridges two or more metals, which is not the case with these transition states. The reason the CO is bent on its approach to the DNIC may be more clearly seen in the SOMO, where the unpaired electron moves from the iron, its residence in the starting material, **1**, out onto the CO. As shown in Figure V-8, the unpaired electron on the $[Fe(NO)_2]$ captures the incoming ligand by donating into

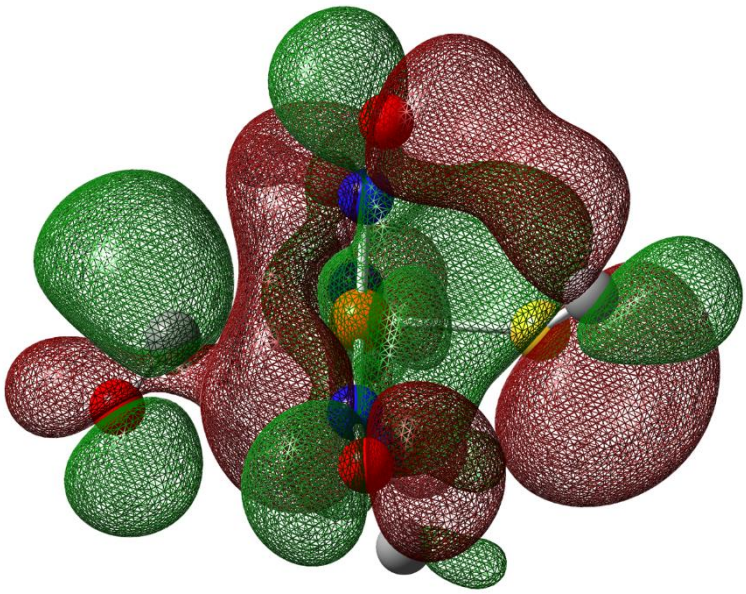

Figure V-8. SOMO of **[1-3']**‡ showing overlap of the unpaired electron orbital of the $[Fe(NO)_2]$ with the π* of the CO.

the π* orbital of the carbonyl, pulling the CO onto the DNIC, where it can then straighten and bind in the typical σ-donating, π-withdrawing fashion.

Another feature of these transition states is the subtle elongation of the Fe – S(SR) bond by *ca.* 0.1 Å, from 2.225 Å in **1** to 2.334 Å in **[1-3']**‡ and 2.343 Å in **[1-3"]**‡. At the same time, the Fe – N – O angles decrease as the nitrosyl ligands bend to accept more electron density. These transition states are similar in energy, at 19.2 and 19.6 kcal/mol for **[1-3']**‡ and **[1-3']**‡ respectively, making them indistinguishable within the accepted accuracy of DFT. With less than 2 kcal/mol difference between the energies of these transition states, calculated for the truncated structure, and the experimental $\Delta G^{\ddagger}$ of reaction, as well as the

experimental rate law being first order in both CO and DNIC, it is reasonable to assign either or both **[1-3']**‡ and **[1-3"]**‡ as the transition states for the rate determining step.

Possible Intermediates Subsequent to Fe-CO Bond Formation

With the knowledge that the 19 electron, 5-coordinate iron in intermediate **3** is less stable than a 17 electron, 4-coordinate iron, another search for iron-bound RSNO was carried out. Two intermediate structures were located, one of which has an N-bound RSNO, **6**, similar to **4**, while the other has an S-bound RSNO, **7**, similar to **5**, Figure V-9. The differences between these four-coordinate iron-bound RSNOs and the previous, three-coordinate iron-bound RSNOs is substantial, with a more than 10 kcal/mol stabilization

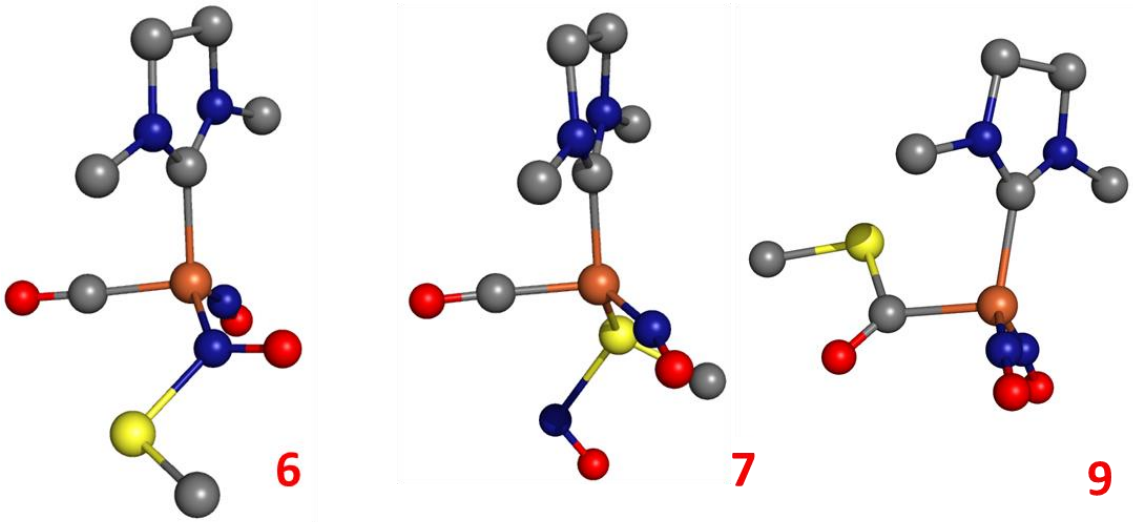

Figure V-9. Calculated structures of the four-coordinate iron intermediates formed by NO insertion into the Fe-SR bond (**6**), NO migration onto the SR (**7**), or CO insertion into the Fe-SR bond (**9**)

seen when the open site on the iron is occupied by a CO ligand, at 22.6 and 24.0 kcal/mol for **6** and **7** respectively. Despite being much more stable than **4** and **5**, these intermediates are still too high in energy to be on a productive reaction pathway.

A third possible intermediate, **9**, was examined in which the thiolate is moved from the iron to the carbonyl ligand, rather than NO, as in intermediate **6**. The regeneration of the tetrahedral geometry about the iron generates a more stable structure, Figures V-4 and V-9, with a free energy of +10.4 kcal/mol, than the five-coordinate intermediate, **3"**, that precedes it. With the removal of the thiolate from the iron core, the DNIC is once more a 17 electron species, and the excess electron density is removed from the NO ligands, as confirmed by the more linear Fe – N – O angles, which have straightened to 172.6° and 170.9°. As a consequence of the formation of a thiocarbonyl, the Fe – C(CO) distance increases by ~0.1 Å to 1.965 Å and the Fe – C – O angle reduces to 130.6°.

*Transition States Leading to the Formation of **9** and **2***

The search for transition states leading to the formation of **9** was carried out and the lowest energy transition state was located by performing a Berny calculation, using the input from a relaxed coordinate scan that increased the S – Fe – C (CO) angle of **9** in a step-wise manner. This transition state, **[3"-9]**‡, shows the thiolate migrating from the iron to the carbonyl ligand as the iron shifts back to a more tetrahedral coordination geometry, with a free energy of 18.4 kcal/mol, Figure V-10. The Fe – S bond elongates from 2.341 to 2.455 Å while the S – Fe – C (CO) angle decreases from 86.8° to 64.0°. As the Fe – N –

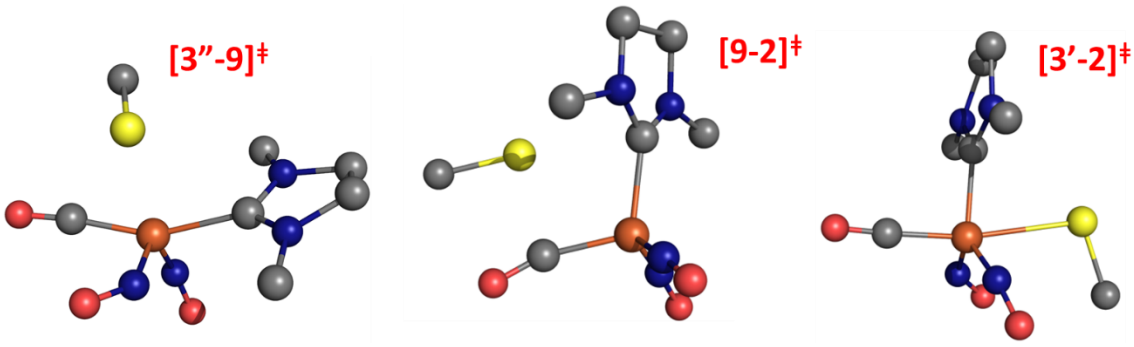

Figure V-10. Calculated structures of the transition states in which the SR migrates from the Fe to the CO, **[3”-9]**‡, The ·SR radical leaves by C – S homolytic bond cleavage, (**[9-2]**‡), and the ·SR radical leaves by Fe – S homolytic bond cleavage, **[3’-2]**‡

O angles remain bent, at 143.3° and 142.8°, the NO ligands can still be considered to store the excess electron density of a 19-electron iron.

The transition states leading to the generation of the reaction product, **2**, both develop from S – X homolytic bond cleavage, where X = C (CO) if the preceding intermediate is **9**, and where X = Fe if the preceding intermediate is **3’**, Figure V-10. Both transition states were located through Berny calculations in which a structure guess was found through relaxed coordinate scans along the S – C (CO) and S – Fe bonds for **[9-2]**‡ and **[3’-2]**‡, respectively. In both transition states, the S – X bond lengthens by ca. 0.3 Å, from 3.114 to 3.379 Å for **[9-2]**‡ and from 2.346 to 2.745 Å for **[3’-2]**‡. However, the other structural changes from the preceding intermediates, **9** and **3’**, are not similar, owing to the differences in the intermediates. The most significant change observed between **9** and **[9-2]**‡ is the straightening of the Fe – C – O bond, from 130.6° to 162.2° as the thiyl radical leaves the

carbonyl ligand, which is not present in the other transition state. The S – C bond cleavage is only +17.0 kcal/mol, while the S – Fe bond cleavage is significantly higher in energy, at +21.2 kcal/mol. The **[3'-2]**‡ transition state more closely resembles the thiolate migration in **[3"-9]**‡ than the S – C cleavage transition state, **[9-2]**‡. The difference in energies of these final transition states leading to the synthetic product, **2**, indicates that the reaction pathway in which the thiolate migrates onto the carbonyl ligand, by way of intermediate **9**, is favoured by ~1.5 kcal/mol.

As can be observed in the reaction profiles in Figures V-11 and V-12, the generation of a thiyl radical is +9.4 kcal/mol. Although the thermodynamic free energy of this reaction is uphill to this point, the coupling of two thiyl radicals to form a stable disulfide produces a large driving force ($\Delta G = -12.8$ kcal/mol) for the overall reaction.[216] The reaction profiles also show that the rate determining step involves the $Fe(NO)_2$ unit as a nucleophile toward the empty π^* orbitals of CO. This explains the unusual, inverse dependence of the rate of reaction on the strength of the incoming nucleophile that was observed experimentally.

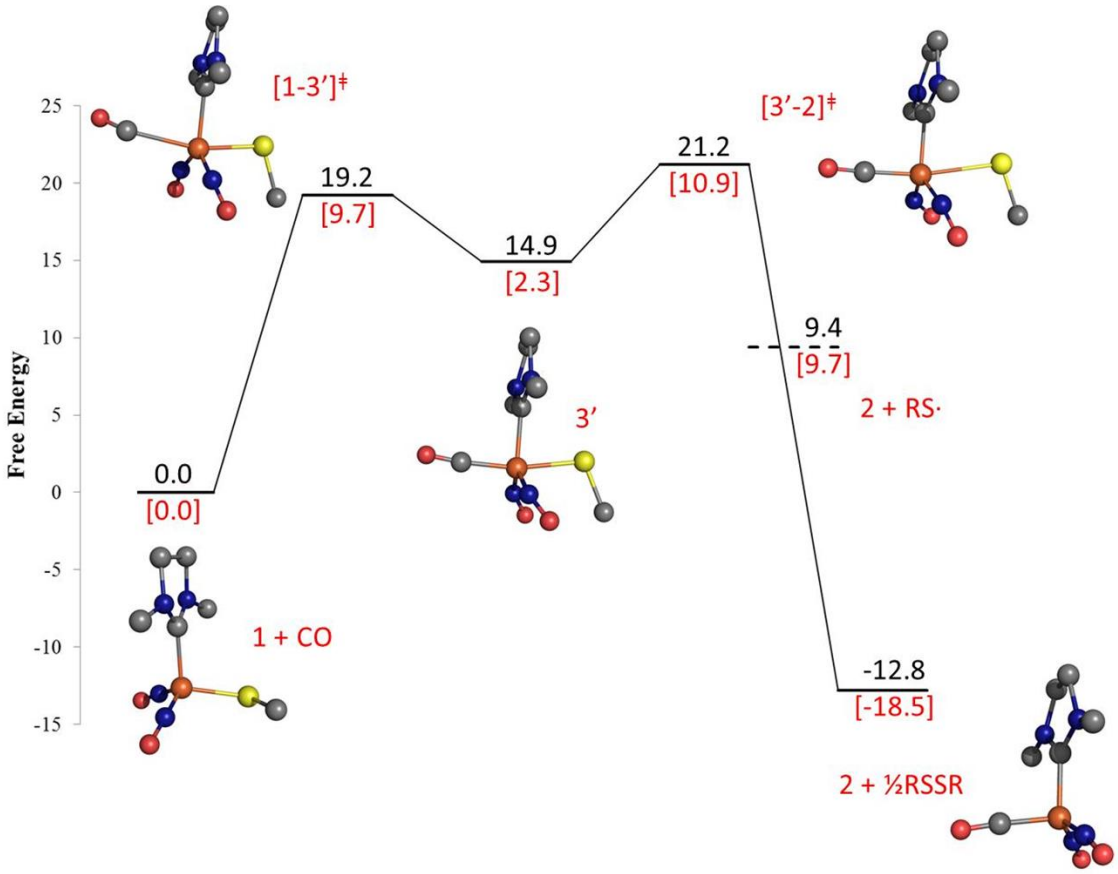

Figure V-11. Calculated reaction pathway in which the DNIC reactant, **1**, performs a nucleophilic attack on a CO molecule, generating a five-coordinate intermediate. The product, **2** is formed by homolytic Fe – S bond cleavage. The energies provided for each minimum and transition state structure in black are free energies, while those energies in red and bracketed are the enthalpies.

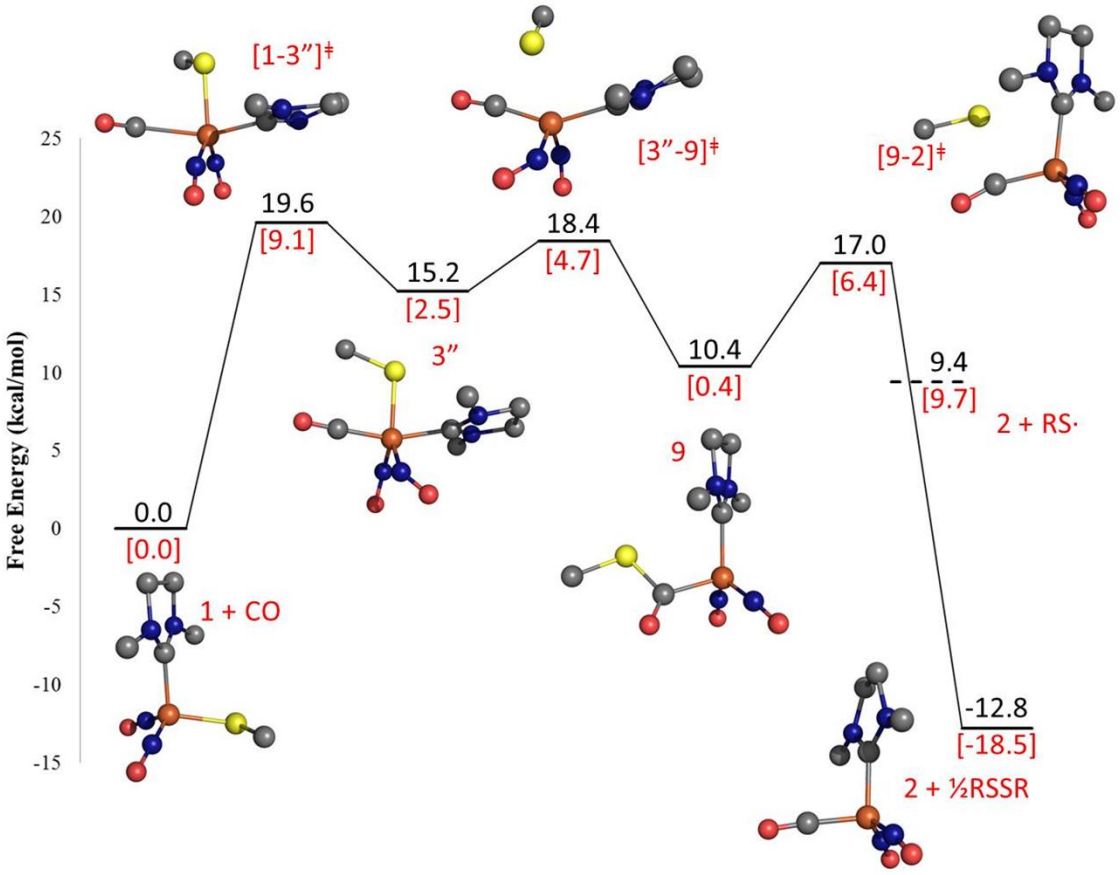

Figure V-12. Calculated reaction pathway in which the DNIC reactant, **1**, performs a nucleophilic attack on a CO molecule, generating a five-coordinate intermediate. In this scheme, the product, **2** is formed by homolytic C – S bond cleavage after thiolate migration on the the carbonyl ligand. The energies provided for each minimum and transition state structure in black are free energies, while those energies in red and bracketed are the enthalpies.

Conclusions

Density Functional Theory predicted two plausible reaction pathways, by which the CO induced reductive elimination of a disulfide might proceed under the mild reaction conditions observed. The experimental activation energy at 298.15 K, determined by Eyring analysis is within 2 kcal/mol of both calculated reaction pathways, Figures V-11 and V-12, while the associative mechanism predicted by experiment, being first order in both **1** and CO, was supported. However, a mechanism in which the $Fe(NO)_2$ unit acts as a nucleophile, grabbing the CO by its empty π^* orbital, was not anticipated. That the $Fe(NO)_2$ moiety remained intact, even with Fe – C (CO) bond formation leading to a five-coordinate, 19-electron iron, speaks to the stability of the dinitrosyl iron unit.

A recent paper from the Darensbourg research group performed further investigation of the CO induced reduction of **1**, by Hammett analysis. Varying the phenylthiolate ligand by substitution of electron donating or withdrawing groups in the *para* position allowed for kinetics studies to be carried out with subtle perturbations of the electron density at the iron. This study supported the mechanisms I have described above, in which the DNIC acts as the nucleophile. Unfortunately, the differences in the rates of reactions for the series of complexes investigated were small, usually within an order of magnitude of the rate of reaction of complex **1**. Although attempts to continue computational correlations were made, the activation barriers for both **[1-3']**‡ and **[1-3"]**‡ were too similar in energy across the series, ranging from 19.5 to 21.1 kcal/mol, and no clear trend could be established.

CHAPTER VI

CONCLUDING REMARKS*

As our knowledge of the properties of hydrogenase enzymes grows, we have found that the fundamental chemistry of iron with diatomic ligands continues to find new relevance on the cutting edge of research. The hydrogenase field is easily one of the best examples of the explosive growth of bioorganometallic chemistry, with a June 2014 search for the term "hydrogenase" using the Scifinder locating more than 3200 references in the past five years alone. A new and rapidly growing field of hydrogenase research is the biosynthesis of the [FeFe]-H_2ase and its active site. I have been particularly interested in the development of this subject during my graduate studies at Texas A&M, highlighting some of the most important discoveries in the field. That the 2Fe portion of the active site is a genuine organometallic species, replete with carbon monoxide, cyanide, and a previously biologically unknown dithiolate cofactor, coupled with the impressive rate of the [FeFe]-H_2ase catalysis of H_2 production from mild potential electrons and water as proton source,[217] has brought global attention of chemists in search of an optimal synthetic analogue of the active site, without protein, as prospective molecular electrocatalysts for hydrogen production.

*This chapter is reproduced in part in permission from Bethel, R. D.; Singleton, M. L.; Darensbourg, M. Y.; . The Modular Assembly of Clusters is the Natural Synthetic Strategy for the Active Site of [FeFe] Hydrogenase *Angewandte Chemie, International Edition*, **49**, 8567-8569 (2010). Copyright 2010 Wiley-VCH Verlag GmbH& Co. KGaA, Weinheim.

The presence of those diatomic ligands and their coordination in the active site has raised a number of questions: How does nature generate and manage CN^- and CO, known to poison metal sites if uncontrolled? How is the azadithiolate that connects the irons within the 2Fe subsite made? How is the active site assembled? Does a 6Fe supercluster precede and extrude the 2Fe subsite, or is the assembly modular? What can the study of synthetic analogues inform chemists of the reactivity of the 2Fe subsite?[168]

Insights into the first two questions have been provided by recent discoveries from Britt and coworkers and their studies of the HydG maturase,[75] which utilizes radical SAM (S-adenosyl methionine) pathways to degrade tyrosine into p-cresol and the diatomic ligands, CO and CN^-.[71,72,218] This is presumed to occur through the generation of a glycyl radical, which is observed by freeze-quench EPR spectroscopy to bind to the iron of a second 4Fe4S cluster in the HydG protein. This HN=CH-COO moiety is then split into an iron-bound cyanide and carbonyl through an unknown mechanism.[75] Upon addition of another CO ligand, thought to require a second tyrosine, an $Fe(CO)_2(CN)$ unit has been observed by FTIR spectroscopy. The current hypothesis is that two of these units are linked together by a bridging azadithiolate ligand, perhaps provided by the HydE maturase,[219,220] generating an active site precursor similar to the synthetic $(\mu\text{-adt})[Fe(CO)_2(CN)]_2^{2-}$.

Guidance to answers to the next two questions has been provided by Mulder, Peters, Broderick et al., and additional biosynthetic and spectroscopic results on the nature of the 2Fe2S subsite precursor.[76,183] They obtained the [FeFe]-H_2ase (also known as HydA) protein expressed in the absence of the HydE, HydF, and HydG proteins, known to be required for the synthesis of the 2Fe subsite and the maturation of the enzyme into active

form.[76] The immature protein, produced without the accessory proteins and known as HydAΔ^{EFG}.

Whereas structures of the native HydA show the full active site H-cluster in the form of cysteine-bridged subsites, that is, 4Fe4S(μ-SCys)2Fe, only the 4Fe4S cluster is found in HydAΔ^{EFG}. The structure of HydAΔ^{EFG} shows the already-present 4Fe4S cluster resides in a cavity at the end of a channel (8–15 Å wide and 25 Å long; Figure VI-1). Overlays of the structures of the immature or apo-protein that lacks the 2Fe subsite with the complete or holo-protein show that the channel has closed in the latter, thus wrapping up the completed active site.

Analysis of the channel composition in HydAΔ^{EFG} indicates that positive amino acid residues (an arginine and two lysines) flank the entrance, thus most likely attracting the 2Fe subcluster with its negatively charged cyanides; another lysine within the channel is purported to form hydrogen bonds to the 2Fe subsite once it is in place as a constituent of the H-cluster.[76] Yet another clue as to the guidance mechanism is a cysteine near the end of the cavity, the sulfur side chain of which is exposed and might be expected to swap out with a labile ligand on the 2Fe unit, becoming the bridge between the 4Fe4S and the 2Fe subunits.

Without a doubt, the ligand substitution processes of the (μ-SRS)[$Fe_2(CO)_x(L)_{6-x}$] complexes that I have performed on the benchtop and investigated *in silico*, as reported in Chapter III, are necessary to the attachment of the 4Fe4S cluster in the apo-HydA enzyme to the 2Fe subsite. My own investigations have found that the displacement of a CO by

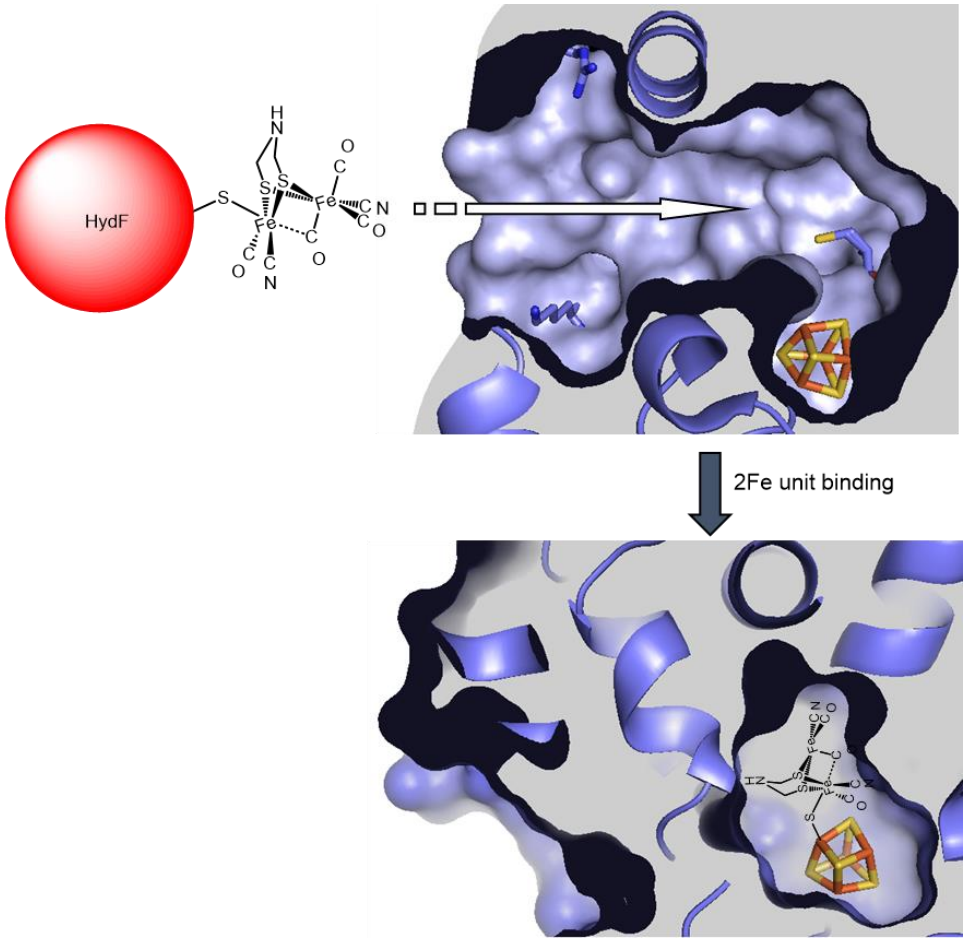

Figure VI-1. This figure, adapted from reference 168 with permission, shows the pre-assembled 2Fe organometallic unit as itinserts into apo-HydA. Positively charged residues help direct the precursor unit to the already present 4Fe4S, possibly with assistance of a cysteine sulfur atom within the channel. When the 2Fe units bind to the 4Fe4S cluster at the base of the channel, completing the H-cluster, the cavity collapses, burying the active site within the protein.[66]

an incoming ligand, such as what is seen by the attachment of a (μ-adt)$[Fe(CO)_2(CN)]_2$ unit to the iron-sulfur cluster bound thiolate buried in the HydA enzyme, has shown that a nucleophilic ligand will prefer to attack the electron-poor iron site. If the diiron subunit

is to bind to a thiolate, either the 2Fe unit has been oxidized, allowing for SR/CO exchange, or perhaps the Fe-bound thiolate has been sufficiently masked by the electron-withdrawing iron-sulfur cluster to allow for a more electrophilic attack to occur.

Indeed, we (Professor Marcetta Darensbourg and I) have highlighted[221] the results of Fontecave, Happe, and coworkers, who reported in a pair of papers,[53,142] the symmetric, synthetic (μ-SRS)$[Fe(CO)_2(CN)]_2^{2-}$ synthon was found to bind to HydF, the maturase thought to act as a scaffold for active site delivery to apo-HydA. FTIR and EPR spectroscopic studies of HydF bound to a series of diiron molecules, varying by the bridgehead: CH_2, NH, or O, have shown that this protein can carry and deliver the 2Fe site analogues to the HydA, completing the biosynthesis and generating an intact [FeFe]-H_2ase enzyme.[53] Although the enzymes with the CH_2 and NH bridgeheads were virtually indistinguishable by spectroscopy, only the enzyme with the amine in the dithiolate bridge was functional in H^+ reduction studies, producing H_2 at a rate comparable to the native enzyme. An even more recent report has shown that the HydF scaffold may be unnecessary for H_2ase activation, as the (μ-adt)$[Fe(CO)_2(CN)]_2^{2-}$ molecule can bind to and activate the apo-HydA enzyme without the need for its so-called "chaperone".[142] That the diiron unit, which becomes the 2Fe subunit of the active site, does not require assistance to obtain the correct geometry in the active site may be attributed to the fluxional motions that I described in Chapter IV. At room temperature, the $Fe(CO)_2(CN)$ moieties are free to rotate, but the presence of non-carbonyl ligands may provide a means for the enzyme active site to "lock" into the optimal geometry. This geometry in which the distal iron has generated an open site may be achieved through the introduction of a hydrogen bond

between the cyanide ligand and an N-H proton from an amino acid lining the active site cavity.[9]

The implications of this stepwise assembly mechanism are profound for biologists and for chemists. Mulder et al. note a similarity between the structural features described above and the nitrogenase protein that lacks the FeMo cofactor and the holo-protein.[76] This could signal that the ability of such proteins to incorporate a pre-existing abiotic catalyst could be a wide spread motif in early metalloenzyme development.

For chemists, the speculation that the original 2Fe subsite was a standalone ancient catalyst, recognized by evolving microorganisms as beneficial to their growth and prosperity, reinvigorates designs to use synthetic ligands to reproduce the electronic environment about the prebiotic iron sulfide catalyst. However, despite reports of more than 400 model complexes; none perform the $2H^+ + 2e^- \rightarrow H_2$ catalysis as does the H-cluster. Is there a requirement for the 4Fe4S cluster to be attached? This feat has been demonstrated to be feasible in an elegant synthetic analogue of the full 6Fe cluster;[222] however, with no greater catalytic success. In another highlight of a recent hydrogenase model complex,[223] I have shown an example of the progress that has been made in the synthesis of complexes that better mimic this function through the inclusion of the redox-active ligand derived from ferrocene, which Rauchfuss and coworkers have linked to a diiron hydrogenase model complex through a phosphine ligand, Figure VI-2.[224] With the addition of the *cis*-1,2-bis(diphenylphosphino)ethylene (dppv) ligand, known to promote the "rotated" isomeric form upon oxidation of the diiron core, as well as the inclusion of

an amine in the bridgehead position of the dithiolate ligand, this model complex has shown catalytic H_2 oxidation without the massive over-pressurization that previous generations

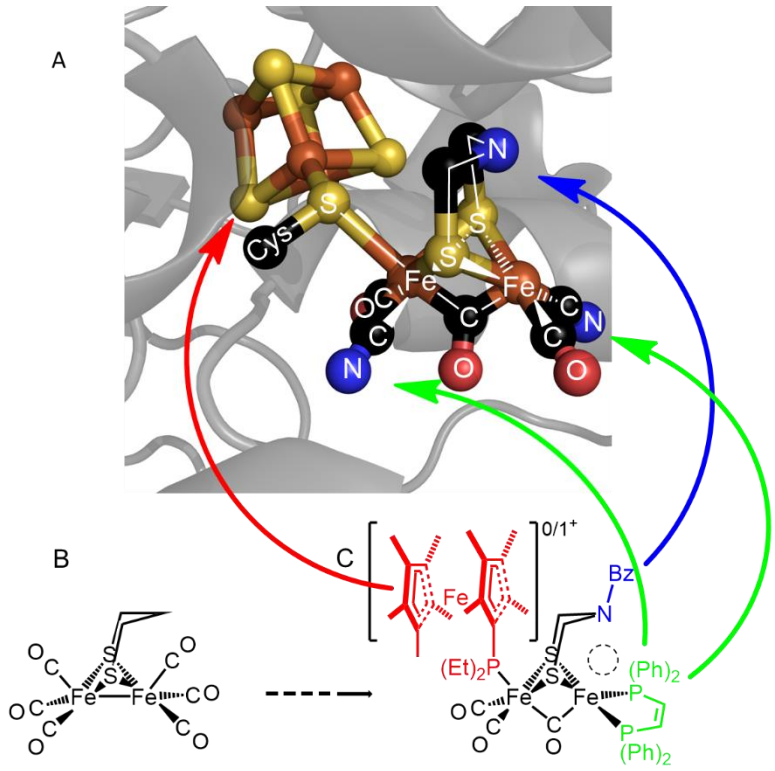

Figure VI-2. In this figure adapted from reference 223, a cartoon of the 6Fe, hydrogen producing cluster in the [FeFe]-hydrogenase is shown with the redox-active 4Fe4S cluster, pendent amine, and electron donating cyanide ligands indicated (A).[47] The bridgehead position in the dithiolate cofactor within the 2Fe subsite is replaced by a nitrogen, and a bridging carbonyl is inserted between the two iron atoms, reflecting the current understanding of the [FeFe]-Hydrogenase active site. The parent model complex, (μ-pdt)$[Fe(CO)_3]_2$ (B) is modified into a better model of the active site[40] (C), with key functionalities of the active site modeled as indicated by red, blue and green arrows.

of model complexes have required. Thus it indeed appears to be the 2Fe subsite that must be strategically tuned in electronic and steric properties, both at the metal site where the reaction occurs and in the coordination spheres surrounding it.

The natural approach to the synthesis begins with oxidized iron, possibly from the iron-sulfur clusters, whereas the synthetic analogues typically use reduced iron in (μ-SRS)$[Fe^{I}(CO)_3]_2$ as precursor. These complexes achieve stable rotated forms in only a few cases,[109,225,226] which in nearly every instance return to the "unrotated" isomeric form on reduction. This suggests that the chemists' efforts might profitably be directed in pursuit of 1) alternative FeFe precursors and 2) supramolecular constructs that will collapse around the 2Fe synthetic analogue and maintain it in the rotated form throughout its electrocatalytic cycle.

The role of organometallic-like iron moieties in nature is further emphasized in the physiologically significant $Fe(NO)_2$ complexes. As this unit in its reduced form, $\{Fe(NO)_2\}^{10}$, is isoelectronic with $Fe^0(CO)_x(CN)_{3-x}$, the chemistry mediated by complexes containing $L_2Fe(CO)_x(CN)_{3-x}$ or $L_2Fe(NO)_2$ can be comparable. Hence, through studies of CO addition to $(NHC)(SR)Fe(NO)_2$ as explored in Chapter V,[204] the possibility of an associative process giving rise to the displacement of a thiyl radical is relevant to the processes observed in the assembly of the hydrogenase enzymes as well as the redox processes of DNICs *in vivo*.

In conclusion, the role of the chemist in the growing bioorganometallic field is to provide insight into the native behavior of the small molecules that are key to the activity of an

enzyme or the form in which a more reactive unit may be stored. My own studies have added to our knowledge of the regioselective CO displacement reactions of diiron model complexes and their fluxional processes, which may help to explain how this unique biological unit is generated, as well as my proposed mechanism for CO induced reductive elimination of a thiyl radical by way of a five-coordinate intermediate. It is my hope that these papers may prompt new investigations to continue to explore this rich and growing field.

REFERENCES

(1) Stephenson, M. S., L. H. *Biochemical Journal* **1931**, *25*, 205.

(2) Bagley, K. A. V. G., C. J.; Chen, M.; Duin, E. C.; Albracht, S. P. J; Woodruff *Biochemistry* **1994**, *33*, 9229.

(3) Happe, R. P. R., W.; Pierik, A. J.; Albracht, S. P. J.; Bagley, K. A. *Nature* **1997**, *385*, 126.

(4) Pierik, A. J. R., W.; Happe, R. P.; Bagley, K. A.; Albracht, S. P. J. *Journal of Biological Chemistry* **1999**, *274*, 3331.

(5) Lai, C.-H.; Lee, W.-Z.; Miller, M. L.; Reibenspies, J. H.; Darensbourg, D. J.; Darensbourg, M. Y. *Journal of the American Chemical Society* **1998**, *120*, 10103.

(6) Higuchi, Y. O., H.; Miki, K.; Yasuoka, N.; Yagi, T. *Structure* **1999**, *7*, 549.

(7) Volbeda, A. C., M.-H.; Piras, C.; Hatchikian, E. C.; Frey, M.; Fontecilla-Camps, J. C.; *Nature* **1995**, *373*, 580.

(8) Volbeda, A.; Martin, L.; Cavazza, C.; Matho, M.; Faber, B. W.; Roseboom, W.; Albracht, S. P.; Garcin, E.; Rousset, M.; Fontecilla-Camps, J. C. *Journal of Biological Inorganic Chemistry* **2005**, *10*, 239.

(9) Nicolet, Y. L., B. J.; Fontecilla-Camps, J. C.; Peters, J. W. *Trends in Biochemical Sciences* **2000**, *25*, 138.

(10) Nicolet, Y. P., C.; Legrand, P.; Hatchikian, C. E.; Fontecilla-Camps, J. C. *Structure* **1999**, *7*, 13.

(11) De Lacey, A. L. S., C.; Cavazza, C.; Hatchikian, E. C.; Fernandez, V. M. *Journal of the American Chemical Society* **2000**, *122*, 11232.

(12) Nicolet, Y. d. L., A. L.; Vernède, X.; Fernandez, V. M.; Hatchikian, E. C.; Fontecilla-Camps, J. C *Journal of the American Chemical Society* **2001**, *123*, 1596.

(13) Peters, J. W. *Science* **1998**, *282*, 1853.

(14) Hiromoto, T.; Ataka, K.; Pilak, O.; Vogt, S.; Stagni, M. S.; Meyer-Klaucke, W.; Warkentin, E.; Thauer, R. K.; Shima, S.; Ermler, U. *FEBS letters* **2009**, *583*, 585.

(15) Lyon, E. J.; Shima, S.; Buurman, G.; Chowdhuri, S.; Batschauer, A.; Steinbach, K.; Thauer, R. K. *European Journal of Biochemistry* **2004**, *271*, 195.

(16) Korbas, M.; Vogt, S.; Meyer-Klaucke, W.; Bill, E.; Lyon, E. J.; Thauer, R. K.; Shima, S. *The Journal of Biological Chemistry* **2006**, *281*, 30804.

(17) Shima, S.; Pilak, O.; Vogt, S.; Schick, M.; Stagni, M. S.; Meyer-Klaucke, W.; Warkentin, E.; Thauer, R. K.; Ermler, U. *Science* **2008**, *321*, 572.

(18) Vignais, P. M. B., B. *Chemical Reviews* **2007**, *107*, 4206.

(19) Hoberman, H. D. R., D. *Journal of Biological Chemistry* **1943**, *147*, 211.

(20) Sadana, J. C. J., V. *Biochemica et Biophysica Acta* **1956**, *19*, 440.

(21) Shug, A. L. W., P. W.; Green, D. E.; Mahler, H. R. *Journal of the American Chemical Society* **1956**, *76*, 3355.

(22) Beinert, H. *Science* **1997**, *277*, 653.

(23) Nakos, G. M., L. *Biochemica et Biophysica Acta* **1971**, *227*, 576.

(24) Moura, J. J. G. M., I.; Huynh, B. H.; Krüger, H.-J.; Teixeira, M.; DuVarney, R. C.; DerVartanian, D. V.; Xavier, A. V.; Peck, Jr., H. D.; LeGall, J. *Biochemical and Biophysical Research Communications* **1982**, *108*, 1388.

(25) Teixeira, M. M., I.; Xavier, A. V.; Huynh, B. H.; DerVartanian, D. V.; Peck, Jr., H. D.; LeGall, J.; Moura, J. J. G.; *Journal of Biological Chemistry* **1985**, *260*, 8942.

(26) Roberts, L. M. L., P. A. *Journal of the American Chemical Society* **1995**, *117*, 2565.

(27) Lindahl, P. A. In *Metal Ions in Life Sciences* Sigel, S., and Sigel, Ed. 2009; Vol. 6, p 133.

(28) Webster, C. E. D., M. Y.; Lindahl, P. A.; Hall, M., B. *Journal of the American Chemical Society* **2004**, *126*, 3410.

(29) Riorden, C., G. *Journal of Biological Inorganic Chemistry* **2004**, *9*, 509.

(30) *Organometallic Chemistry of B12 Coenzymes*; Kräutler, B., Ed., 2009; Vol. 6.

(31) Groves, J. T. *Journal of Inorganic Biochemistry* **2006**, *100*, 434.

(32) Takai, K.; Gamo, T.; Tsunogai, U.; Nakayama, N.; Hirayama, H.; Nealson, K. H.; Horikoshi, K. *Extremophiles : life under extreme conditions* **2004**, *8*, 269.

(33) Ma, K. S., R., N.; Kelly, R., M.; Adams, M., W., W. *Proceedings of the National Academy of Sciences of the United States of America* **1993**, *90*, 5341.

(34) Cammack, R.; Taylor and Francis: London, U.K., 2001.

(35) Vincent, K. A. P., A.; Armstrong, F. A *Chemical Reviews* **2007**, *107*, 4366.

(36) Gordon, J. C.; Kubas, G. J. *Organometallics* **2010**, *29*, 4682.

(37) Kubas, G. J. *Journal of the Chemical Society, Chemical Communications* **1980**, 61.

(38) Kubas, G. J. R., R., R.; Swanson, B. I.; Vergamini, P., J.; Wasserman, H., J.; *Journal of the American Chemical Society* **1984**, *106*, 452.

(39) Crabtree, R. H. *Angewandte Chemie* **1993**, *32*, 789.

(40) Kubas, G. J. *Metal Dihydrogen and σ-Bond Complexes: Structure, Theory, and Reactivity*, 2002.

(41) Crabtree, R., H.; Lavin, M.; Bonneviot, L. *Journal of the American Chemical Society* **1986**, *108*, 4032.

(42) Heinekey, D., M.; Lledós, A.; Lluch, J., M. *Chemical Society Reviews* **2004**, *33*, 175.

(43) Heinekey, D. M. *Journal of Labelled Compounds and Radiopharmaceuticals* **2007**, *50*, 1063.

(44) Kuhlman, R. *Coordination Chemistry Reviews* **1997**, *167*, 205.

(45) Forde, C. E.; Landau, S. E.; Morris, R. H. *Journal of the Chemical Society, Dalton Transactions* **1997**, 1663.

(46) Greco, C.; Bruschi, M.; Fantucci, P.; Ryde, U.; De Gioia, L. *Journal of the American Chemical Society* **2011**, *133*, 18742.

(47) Bruschi, M. G., C.; Bertini, L.; Rantucci, P.; Ryde, U.; De Gioia, L. *Journal of the American Chemical Society* **2010**, *132*, 4992.

(48) Garcin, E. V., X.; Hatchikian, E., C.; Volbeda, A.; Frey, M.; Fontecilla-Camps, J., C. *Structure* **1999**, *5*, 557.

(49) Shomura, Y.; Yoon, K. S.; Nishihara, H.; Higuchi, Y. *Nature* **2011**, *479*, 253.

(50) Pandelia, M.-E. B., D.; Izask, R.; Infossi, P.; Giudici-Orticoni, M.-T.; Bill, E.; Neese, F.; Lubitz, W. *Proceedings of the National Academy of Sciences of the United States of America* **2013**, *110*, 482.

(51) Silakov, A.; Wenk, B.; Reijerse, E.; Lubitz, W. *Physical Chemistry Chemical Physics : PCCP* **2009**, *11*, 6592.

(52) Erdem, O. F.; Schwartz, L.; Stein, M.; Silakov, A.; Kaur-Ghumaan, S.; Huang, P.; Ott, S.; Reijerse, E. J.; Lubitz, W. *Angewandte Chemie* **2011**, *50*, 1439.

(53) Berggren, G.; Adamska, A.; Lambertz, C.; Simmons, T. R.; Esselborn, J.; Atta, M.; Gambarelli, S.; Mouesca, J. M.; Reijerse, E.; Lubitz, W.; Happe, T.; Artero, V.; Fontecave, M. *Nature* **2013**, *499*, 66.

(54) Zirngibl, C. H., R.; Thauer, R., K. *Federation of European Biochemical Societies* **1990**, *261*, 112.

(55) Thauer, R., K.; Klein, A., R.; Hartmann, G., C. *Chemical Reviews* **1996**, *96*, 3031.

(56) Shima, S.; Thauer, R. K. *Chemical Record* **2007**, *7*, 37.

(57) Dey, S.; Das, P. K.; Dey, A. *Coordination Chemistry Reviews* **2013**, *257*, 42.

(58) Yang, X.; Hall, M. B. *Journal of the American Chemical Society* **2009**, *131*, 10901.

(59) Liu, Z.-P. H., P. *Journal of the American Chemical Society* **2002**, *124*, 5175.

(60) Fan, H.-J. H., M., B. *Journal of the American Chemical Society* **2001**, *123*, 3828.

(61) Lubitz, W. R., E.; van Gastel, M. *Chemical Reviews* **2007**, *107*, 4331.

(62) Goris, T.; Wait, A. F.; Saggu, M.; Fritsch, J.; Heidary, N.; Stein, M.; Zebger, I.; Lendzian, F.; Armstrong, F. A.; Friedrich, B.; Lenz, O. *Nature Chemical Biology* **2011**, *7*, 310.

(63) Volbeda, A. A., P.; Darnault, C.; Mouseca, J.-M.; Parkin, A.; Roessler, M., M.; Armstrong, F., A.; Fontecilla-Camps, J., C. *Proceedings of the National Academy of Sciences of the United States of America* **2012**, *109*, 5305.

(64) Swanson, K. D.; Duffus, B. R.; Beard, T. E.; Peters, J. W.; Broderick, J. B. *European Journal of Inorganic Chemistry* **2011**, *2011*, 935.

(65) Ohki, Y.; Tatsumi, K. *European Journal of Inorganic Chemistry* **2011**, *2011*, 973.

(66) Böck, A.; King, P. W.; Blokesch, M.; Posewitz, M. C. **2006**, *51*, 1.

(67) Lenz, O.; Ludwig, M.; Schubert, T.; Burstel, I.; Ganskow, S.; Goris, T.; Schwarze, A.; Friedrich, B. *Chemphyschem* **2010**, *11*, 1107.

(68) Fontecilla-Camps, J. C. V., A.; Cavazza, C.; Nicolet, Y. *Chemical Reviews* **2007**, *107*, 4273.

(69) Stripp, S. T.; Soboh, B.; Lindenstrauss, U.; Braussemann, M.; Herzberg, M.; Nies, D. H.; Sawers, R. G.; Heberle, J. *Biochemistry* **2013**, *52*, 3289.

(70) Rauchfuss, T. B. *Angewandte Chemie* **2010**, *49*, 4166.

(71) Driesener, R. C.; Challand, M. R.; McGlynn, S. E.; Shepard, E. M.; Boyd, E. S.; Broderick, J. B.; Peters, J. W.; Roach, P. L. *Angewandte Chemie* **2010**, *49*, 1687.

(72) Shepard, E., M.; Duffus, B., R.; George, S., J.; McGlynn, S., E.; Challand, M., R.; Swanson, K., D.; Roach, P., L.; Cramer, S., P.; Peters, J., W.; Broderick, J., B *Journal of the American Chemical Society* **2010**, *132*, 9247.

(73) Nicolet, Y.; Martin, L.; Tron, C.; Fontecilla-Camps, J. C. *FEBS letters* **2010**, *584*, 4197.

(74) Driesener, R. C.; Duffus, B. R.; Shepard, E. M.; Bruzas, I. R.; Duschene, K. S.; Coleman, N. J.; Marrison, A. P.; Salvadori, E.; Kay, C. W.; Peters, J. W.; Broderick, J. B.; Roach, P. L. *Biochemistry* **2013**, *52*, 8696.

(75) Kuchenreuther, J. M.; Myers, W. K.; Stich, T. A.; George, S. J.; Nejatyjahromy, Y.; Swartz, J. R.; Britt, R. D. *Science* **2013**, *342*, 472.

(76) Mulder, D. W.; Boyd, E. S.; Sarma, R.; Lange, R. K.; Endrizzi, J. A.; Broderick, J. B.; Peters, J. W. *Nature* **2010**, *465*, 248.

(77) Mulder, D. W.; Ortillo, D. O.; Gardenghi, D. J.; Naumov, A. V.; Ruebush, S. S.; Szilagyi, R. K.; Huynh, B.; Broderick, J. B.; Peters, J. W. *Biochemistry* **2009**, *48*, 6240.

(78) Graf, E., G.; Thauer, R., K. *FEBS letters* **1981**, *136*, 165.

(79) Tard, C. P., C. J. *Chemical Reviews* **2009**, *109*, 1145.

(80) Groysman, S. H., R., H. *Biochemistry* **2009**, *48*, 2310.

(81) Bouwman, E.; Reedijk, J. *Coordination Chemistry Reviews* **2005**, *249*, 1555.

(82) Coffey, C., E. *Journal of Inorganic Nuclear Chemistry* **1963**, *25*, 179.

(83) Heinekey, D. M. *Journal of Organometallic Chemistry* **2009**, *694*, 2671.

(84) Gloaguen, F.; Rauchfuss, T. B. *Chemical Society Reviews* **2009**, *38*, 100.

(85) Zhu, W.; Marr, A. C.; Wang, Q.; Neese, F.; Spencer, D. J.; Blake, A. J.; Cooke, P. A.; Wilson, C.; Schroder, M. *Proceedings of the National Academy of Sciences of the United States of America* **2005**, *102*, 18280.

(86) Ohki, Y.; Yasumura, K.; Kuge, K.; Tanino, S.; Ando, M.; Li, Z.; Tatsumi, K. *Proceedings of the National Academy of Sciences of the United States of America* **2008**, *105*, 7652.

(87) Li, Z. O., Y.; Tatsumi, K. *Journal of the American Chemical Society* **2005**, *127*, 8950.

(88) Jiang, J.; Maruani, M.; Solaimanzadeh, J.; Lo, W.; Koch, S. A.; Millar, M. *Inorganic Chemistry* **2009**, *48*, 6359.

(89) Osterloh, F. S., W.; Haase, D.; Pohl, S. *Journal of the Chemical Society, Chemical Communications* **1997**, *33*, 979.

(90) Tanino, S. L. Z. O., Y.; Tatsumi, K. *Inorganic Chemistry* **2009**, *48*, 2358.

(91) Schilter, D.; Nilges, M. J.; Chakrabarti, M.; Lindahl, P. A.; Rauchfuss, T. B.; Stein, M. *Inorganic Chemistry* **2012**, *51*, 2338.

(92) Canaguier, S.; Field, M.; Oudart, Y.; Pecaut, J.; Fontecave, M.; Artero, V. *Journal of the Chemical Society, Chemical Communications* **2010**, *46*, 5876.

(93) Lai, C.-H. R., J., H.; Darensbourg, M., Y. *Angewandte Chemie* **1996**, *35*, 2390.

(94) Verhagen, Johanna A. W.; Lutz, M.; Spek, Anthony L.; Bouwman, E. *European Journal of Inorganic Chemistry* **2003**, *2003*, 3968.

(95) Liaw, W.-F. C., C.-Y.; Lee, G.-H.; Peng, S.-M.; Lai, C.-H.; Darensbourg, M. Y. *Inorganic Chemistry* **2000**, *39*, 480.

(96) Carroll, M. E.; Barton, B. E.; Gray, D. L.; Mack, A. E.; Rauchfuss, T. B. *Inorganic Chemistry* **2011**, *50*, 9554.

(97) Ogo, S.; Ichikawa, K.; Kishima, T.; Matsumoto, T.; Nakai, H.; Kusaka, K.; Ohhara, T. *Science* **2013**, *339*, 682.

(98) DuBois, M., R.; DuBois, D., L. *Chemical Society Reviews* **2009**, *39*, 62.

(99) Curtis, C., J.; Miedaner, A.; Ciancanelli, R.; Ellis, W., W.; Noll, B., C.; DuBois, M., R.; DuBois, D., L. *Inorganic Chemistry* **2003**, *42*, 216.

(100) Helm, M. L.; Stewart, M. P.; Bullock, R. M.; DuBois, M. R.; DuBois, D. L. *Science* **2011**, *333*, 863.

(101) Liu, T. D., D., L.; Bullock, R., M. *Nature Chemistry* **2013**, *5*, 228.

(102) Reihlen, H. G., A.; Hessling, G. *Justus Leibigs Annalen der Chemie* **1929**, 268.

(103) McGlynn, S., E.; Mulder, D., W.; Shepard, E., M.; Broderick, J., B.; Peters, J., W. *Journal of the Chemical Society, Dalton Transactions* **2009**, *22*.

(104) Darensbourg, M. Y.; Lyon, E. J.; Zhao, X.; Georgakaki, I. P. *Proceedings of the National Academy of Sciences of the United States of America* **2003**, *100*, 3683.

(105) Li, H. R., T., B. *Journal of the American Chemical Society* **2002**, *124*, 726.

(106) Lyon, E. J.; Georgakaki, I. P.; Reibenspies, J. H.; Darensbourg, M. Y. *Journal of the American Chemical Society* **2001**, *123*, 3268.

(107) Felton, G. A. N.; Mebi, C. A.; Petro, B. J.; Vannucci, A. K.; Evans, D. H.; Glass, R. S.; Lichtenberger, D. L. *Journal of Organometallic Chemistry* **2009**, *694*, 2681.

(108) Capon, J.-F.; Gloaguen, F.; Schollhammer, P.; Talarmin, J. *Journal of Electroanalytical Chemistry* **2006**, *595*, 47.

(109) Liu, T. D., M., Y. *Journal of the American Chemical Society* **2007**, *129*, 7008.

(110) Tye, J. W.; Lee, J.; Wang, H. W.; Mejia-Rodriguez, R.; Reibenspies, J. H.; Hall, M. B.; Darensbourg, M. Y. *Inorganic Chemistry* **2005**, *44*, 5550.

(111) Boyke, C., A.; Rauchfuss, T., B.; Wilson, S., R.; Rohmer, M.-M.; Bénard, M. *Journal of the American Chemical Society* **2004**, *126*, 15151.

(112) Nehring, J., L.; Heinekey, D., M. *Inorganic chemistry* **2003**, *42*, 4288.

(113) Zaffaroni, R.; Rauchfuss, T. B.; Gray, D. L.; De Gioia, L.; Zampella, G. *Journal of the American Chemical Society* **2012**, *134*, 19260.

(114) Justice, A. K.; Rauchfuss, T. B.; Wilson, S. R. *Angewandte Chemie* **2007**, *46*, 6152.

(115) Green, K., N.; Hess, J., L.; Thomas, C., M.; Darensbourg, M., Y. *Journal of the Chemical Society, Dalton Transactions* **2009**, *22*, 4344.

(116) Xu, E.; Xiao, Z.; Liu, H.; Long, L.; Li, L.; Liu, X. *RSC Advances* **2012**, *2*, 10171.

(117) Singleton, M., L.; Reibenspies, J., H.; Darensbourg, M., Y *Journal of the American Chemical Society* **2010**, *132*, 8870.

(118) Li, X.; Wang, M.; Zheng, D.; Han, K.; Dong, J.; Sun, L. *Energy & Environmental Science* **2012**, *5*, 8220.

(119) Song, L.-C. Y., Z.-Y.; Bian, H.-Z.; Hu, Q.-M. *Organometallics* **2004**, *23*, 3082.

(120) Song, L.-C. Y., Z.-Y.; Hua, Y.-J.; Wang, H.-T.; Liu, Y.;Hu, Q.-M. *Organometallics* **2007**, *26*, 2106.

(121) Fauvel, K. M., R.; Poilblanc, R. *Inorganic Chemistry* **1976**, *4*, 976.

(122) Tye, J. W.; Darensbourg, M. Y.; Hall, M. B. *Inorganic Chemistry* **2006**, *45*, 1552.

(123) Liu, T.; Li, B.; Popescu, C. V.; Bilko, A.; Perez, L. M.; Hall, M. B.; Darensbourg, M. Y. *Chemistry* **2010**, *16*, 3083.

(124) Chen, D.; Scopelliti, R.; Hu, X. *Angewandte Chemie* **2011**, *50*, 5671.

(125) Wright, J. A.; Turrell, P. J.; Pickett, C. J. *Organometallics* **2010**, *29*, 6146.

(126) Turrell, P. J.; Hill, A. D.; Ibrahim, S. K.; Wright, J. A.; Pickett, C. J. *Journal of the Chemical Society, Dalton Transactions* **2013**, *42*, 8140.

(127) Evans, R. M.; Parkin, A.; Roessler, M. M.; Murphy, B. J.; Adamson, H.; Lukey, M. J.; Sargent, F.; Volbeda, A.; Fontecilla-Camps, J. C.; Armstrong, F. A. *Journal of the American Chemical Society* **2013**, *135*, 2694.

(128) Gao, S.; Guo, H.; Peng, X.; Zhao, X.; Duan, Q.; Liang, Q.; Jiang, D. *New Journal of Chemistry* **2013**, *37*, 1437.

(129) Stoian, S. A.; Hsieh, C. H.; Singleton, M. L.; Casuras, A. F.; Darensbourg, M. Y.; McNeely, K.; Sweely, K.; Popescu, C. V. *Journal of Biological Inorganic Chemistry* **2013**, *18*, 609.

(130) Song, L.-C. W., L.-X.; Jia, G.-J.; Li, Q.-L.; Ming, J.-B. *Organometallics* **2012**, *31*, 5081.

(131) Yu, S.; Wang, F.; Wang, J.-J.; Wang, H.-Y.; Chen, B.; Feng, K.; Tung, C.-H.; Wu, L.-Z. *Pure and Applied Chemistry* **2013**, *85*.

(132) Song, L.-C. G., W.; Luo, X.; Wang, Z.-X.; Sun, X.-J.; Song, H.-B. *Organometallics* **2012**, *31*, 3324.

(133) Li, Y. Z., W.; Qian, G.; Xiao, Z.; Liu, X *Applied Organometallic Chemistry* **2013**, *27*, 253.

(134) Heine, D. P., C.; Schubert, U., S.; Weigand, W. *Journal of Polymer Science* **2013**, *51*, 2171.

(135) Yu, T.; Zeng, Y.; Chen, J.; Li, Y. Y.; Yang, G.; Li, Y. *Angewandte Chemie* **2013**, *52*, 5631.

(136) Pullen, S.; Fei, H.; Orthaber, A.; Cohen, S. M.; Ott, S. *Journal of the American Chemical Society* **2013**, *135*, 16997.

(137) Chen, L. W., M.; Gloaguen, F.; Zheng, D.; Zhang, P.; Sun, L *Inorganic Chemistry* **2013**, *52*, 1798.

(138) Ridley, F.; Ghosh, S.; Hogarth, G.; Hollingsworth, N.; Holt, K. B.; Unwin, D. G. *Journal of Electroanalytical Chemistry* **2013**, *703*, 14.

(139) Manor, B. C.; Rauchfuss, T. B. *Journal of the American Chemical Society* **2013**, *135*, 11895.

(140) Weber, K. K., T.; Shafaat, H., S.; Weyhermuller, T.; Bill, E.; van Gastel, M.; Neese, F.; Lubitz, W. *Journal of the American Chemical Society* **2012**, *134*, 20745.

(141) Siegbahn, P. E. M. T., J. W.; Hall, M. B. *Chemical Reviews* **2007**, *107*, 4414.

(142) Esselborn, J. L., C.; Adamska-Venkatesh, A.; Simmons, T.; Berggren, G.; Noth, J.; Siebel, J.; Hemschemeier, A.; Artero, V.; Reijerse, E.; Fontecave, M.; Lubitz, W.; Happe, T. *Nature Chemical Biology* **2013**, *9*, 607.

(143) Arduengo, A. J., III; Dias, H. V. R.; Harlow, R. L.; Kline, M. *Journal of the American Chemical Society* **1992**, *114*.

(144) Bantreil, X.; Nolan, S. P. *Nature Protocols* **2011**, *6*, 69.

(145) Tonzetich, Z. J.; Heroguel, F.; Do, L. H.; Lippard, S. J. *Inorganic Chemistry* **2011**, *50*, 1570.

(146) Capon, J. F. E. H., S.; Gloaguen, F.; Schollhammer, P.; Talarmin, J *Organometallics* **2005**, *24*, 2020.

(147) Thomas, C. M.; Liu, T.; Hall, M. B.; Darensbourg, M. Y. *Inorganic Chemistry* **2008**, *47*, 7009.

(148) Bruker AXS Inc.: Madison, WI, 2007.

(149) Sheldrick, G. M.; Bruker AXS Inc.: Madison, WI, 2001.

(150) Sheldrick, G. M.; Universitat Gottingen: Gottingen, Germany, 1997.

(151) Sheldrick, G. M.; Universitat Gottingen: Gottingen, Germany, 1997.

(152) Frisch, M. J. T., G. W.; Schlegel, H. B.; Scuseria, G. E.; Robb, M. A.; Cheeseman, J. R.; Scalmani, G.; Barone, V.; Mennucci, B.; Petersson, G. A.; Nakatsuji, H.; Caricato, M.; Li, X.; Hratchian, H. P.; Izmaylov, A. F.; Bloino, J.; Zheng, G.; Sonnenberg, J. L.; Hada, M.; Ehara, M.; Toyota, K.; Fukuda, R.; Hasegawa, J.; Ishida, M.; Nakajima, T.; Honda, Y.; Kitao, O.; Nakai, H.; Vreven, T.; Montgomery, J. A., Jr.; Peralta, J. E.; Ogliaro, F.; Bearpark, M.; Heyd, J. J.; Brothers, E.; Kudin, K. N.; Staroverov, V. N.; Kobayashi, R.; Normand, J.; Raghavachari, K.; Rendell, A.; Burant, J. C.; Iyengar, S. S.; Tomasi, J.; Cossi, M.; Rega, N.; Millam, N. J.; Klene, M.; Knox, J. E.; Cross, J. B.; Bakken, V.; Adamo, C.; Jaramillo, J.; Gomperts, R.; Stratmann, R. E.; Yazyev, O.; Austin, A. J.; Cammi, R.; Pomelli, C.; Ochterski, J. W.; Martin, R. L.; Morokuma, K.; Zakrzewski, V. G.; Voth, G. A.; Salvador, P.; Dannenberg, J. J.; Dapprich, S.; Daniels, A. D.; Farkas, Ö.; Foresman, J. B.; Ortiz, J. V.; Cioslowski, J.; Fox, D. J.; Gaussian, Inc.: Wallingford, CT, 2009.

(153) Becke, A. D. *Journal of Chemical Physics* **1993**, *98*, 5648−5652.

(154) Stephens, P. J. D., F. J.; Chabalowski, C. F.; Frisch, M. J. *Journal of Chemical Physics* **1994**, *98*, 11623−11627.

(155) Lee, C. T. Y., W. T.; Parr, R. G. *Physics Review: B* **1988**, *37*, 785−789.

(156) Krishnan, R. B., J. S.; Seeger, R.; Pople, J. A. *Journal of Chemical Physics* **1980**, *72*, 650−654.

(157) McLean, A. D. C., G. S. *Journal of Chemical Physics* **1980**, *72*, 5639−5648.

(158) Peng, C. S., H. B. *Israel Journal of Chemistry* **1993**, *33*.

(159) Peng, C. A., P. Y.; Schlegel, H. B.; Frisch, M. J. *J Chemical Compositions* **1996**, *17*.

(160) Semichem, Inc.: 12456 W. 62nd Terrace. Suite D, Shawnee, KS, 66216, 1992.

(161) Adamo, C. B., V. *Journal of Chemical Physics* **1998**, *108*, 664−675.

(162) Tao, J. P., J. P.; Staroverov, V. N.; Scuseria, G. E. *Physics Review Letters* **2003**, *91*.

(163) Chai, J.-D. H.-G., M. *Physical Chemistry Chemical Physics : PCCP* **2009**, *10*, 6615−6620.

(164) Becke, A. D. *Physics Review: A* **1988**, *38*, 3098−3100.

(165) Perdew, J. P. *Physics Review: B* **1986**, *33*, 8822−8824.

(166) Brothers, S. M. D., M. Y.; Hall, M. B. *Inorganic Chemistry* **2009**, *50*, 8532−8540.

(167) Stanley, J. L.; Rauchfuss, T. B.; Wilson, S. R. *Organometallics* **2007**, *26*, 1907.

(168) Bethel, R. D.; Singleton, M. L.; Darensbourg, M. Y. *Angewandte Chemie* **2010**, *49*, 8567.

(169) Li, B.; Liu, T.; Singleton, M. L.; Darensbourg, M. Y. *Inorganic Chemistry* **2009**, *48*, 8393.

(170) Olsen, M. T.; Gray, D. L.; Rauchfuss, T. B.; Gioia, L. D.; Zampella, G. *Journal of the Chemical Society: Chemical Communications* **2011**, *47*, 6554.

(171) Tye, J. W.; Darensbourg, M. Y.; Hall, M. B. *Journal of Molecular Structure: THEOCHEM* **2006**, *771*, 123.

(172) Zhao, X.; Chiang, C. Y.; Miller, M. L.; Rampersad, M. V.; Darensbourg, M. Y. *Journal of the American Chemical Society* **2003**, *125*, 518.

(173) Olsen, M. T. B., M.; De Gioia, L; Rauchfuss, T. B.; Wilson, S. R. *Journal of the American Chemical Society* **2008**, *130*, 12021.

(174) Olsen, M. T. J., A. K.; Gloaguen, F.; Rauchfuss, T. B.; Wilson, S. R. *Inorganic Chemistry* **2008**, *47*, 11816.

(175) Hsieh, C. H.; Erdem, O. F.; Harman, S. D.; Singleton, M. L.; Reijerse, E.; Lubitz, W.; Popescu, C. V.; Reibenspies, J. H.; Brothers, S. M.; Hall, M. B.; Darensbourg, M. Y. *Journal of the American Chemical Society* **2012**, *134*, 13089.

(176) Enemark, J. H. F., R. D. *Coordination Chemistry Reviews* **1974**, *13*, 339.

(177) Connelly, N., G.; Geiger, W. E. *Chemical Reviews* **1996**, *96*, 877.

(178) Heo, G. S., Hillman, P. E. and Bartsch, R. A. *Journal of Heterocyclic Chemistry* **1982**, *19*, 1099.

(179) Muller, J. B., R. *Journal of Molecular Structure* **2000**, *520*, 215.

(180) Fischer, R. A.; Miehr, H., E.; Mattner, M. R.; Ambacher, O.; Metzger, T.; Born, E.; Weinkauf, S.; Pulham, C. R.; Parsons, S. *Chemistry: A European Journal* **1996**, *2*.

(181) Thomas, C. M. L., T.; Hall, M. B.; Darensbourg, M. Y. *Journal of the Chemical Society, Chemical Communications* **2008**, 1563.

(182) Crouthers, D. J. D., J. A.; Bethel, R. D.; Munoz, D. G.; Darensbourg, M. Y. *Organometallics* **2014**.

(183) Lyon, E. J. G., I. P.; Reibenspies, J. H.; Darensbourg, M. Y. *Angewandte Chemie* **1999**, *38*, 3178.

(184) Georgakaki, I. P. T., L. M.; Lyon, E. J.; Hall, M., B.; Darensbourg, M. Y. *Coordination Chemistry Reviews* **2003**, 255.

(185) Bertini, L. G., C.; Bruschi, M.; Fantucci, P.; De Gioia, L. *Organometallics* **2010**, *29*, 2013.

(186) Zampella, G. F., P.; De Gioia,L. *Journal of the Chemical Society, Chemical Communications* **2010**, *46*, 8824.

(187) Kessler, H. *Angewandte Chemie* **1970**, *9*, 219.

(188) Zampella, G.; Fantucci, P.; De Gioia, L. *Journal of the American Chemical Society* **2009**, *131*, 10909.

(189) Baffert, C.; Bertini, L.; Lautier, T.; Greco, C.; Sybirna, K.; Ezanno, P.; Etienne, E.; Soucaille, P.; Bertrand, P.; Bottin, H.; Meynial-Salles, I.; De Gioia, L.; Leger, C. *Journal of the American Chemical Society* **2011**, *133*, 2096.

(190) Cramer, C. J. T., D. G. *Physical Chemistry Chemical Physics : PCCP* **2009**, *11*, 10757.

(191) Sousa, S. F. F., P. A.; Ramos, M. J. *Journal of Physical Chemistry: A* **2007**, *111*.

(192) Staroverov, V. N. S., G. E.; Tao, J.; Perdew, J. P. *Journal of Chemical Physics* **2003**, *119*, 12129.

(193) Perdew, J. P.; Akademie Verlag: Berlin, 1991; Vol. 11.

(194) Perdew, J. P. W., Y. *Physics Review: B* **1992**, *45*, 13244.

(195) Lynch, B. J. T., D. G. *Journal of Physical Chemistry: A* **2001**, *105*, 2936.

(196) Grimme, S. *Journal of Chemical Composition* **2006**, *27*, 1787.

(197) Singleton, M. L.; Jenkins, R. M.; Klemashevich, C. L.; Darensbourg, M. Y. *Comptes Rendus Chimie* **2008**, *11*, 861.

(198) Wei, C. H.; Dahl, L. F. *Inorganic Chemistry* **1965**, *4*, 1.

(199) Messelhauser, J. L., I.-P.; Haug, K.; Hiller, W. *Z.Naturforsch.,B:Chem.Sci* **1985**, *40*, 1064.

(200) Hess, J. L.; Hsieh, C. H.; Reibenspies, J. H.; Darensbourg, M. Y. *Inorganic Chemistry* **2011**, *50*, 8541.

(201) Hess, J. L.; Hsieh, C. H.; Brothers, S. M.; Hall, M. B.; Darensbourg, M. Y. *Journal of the American Chemical Society* **2011**, *133*, 20426.

(202) Hsieh, C.-H.; Chupik, R. B.; Pinder, T. A.; Darensbourg, M. Y. *Polyhedron* **2013**, *58*, 151.

(203) Hsieh, C. H.; Brothers, S. M.; Reibenspies, J. H.; Hall, M. B.; Popescu, C. V.; Darensbourg, M. Y. *Inorganic Chemistry* **2013**, *52*, 2119.

(204) Pulukkody, R.; Kyran, S. J.; Bethel, R. D.; Hsieh, C. H.; Hall, M. B.; Darensbourg, D. J.; Darensbourg, M. Y. *Journal of the American Chemical Society* **2013**, *135*, 8423.

(205) Culotta, E. K., D. E. Jr. *Science* **1992**, *258*, 1862.

(206) Vanin, A. F. *Nitric Oxide* **2009**, *21*, 1.

(207) Richardson, D. R. L., H. C. *Biochem Biophys Acta* **2008**, *1780*, 638.

(208) Cruz-Ramos, H. C. J. W., G.; Hughes, M. N.; Scott. C.; Thomson, A. J.; Green, J.; Poole, R. K. *EMBO J.* **2002**, *12*, 3235.

(209) Foster, M. W. C., J. A. *Journal of the American Chemical Society* **1999**, *121*, 4093.

(210) Vithayathil, A. J. T., J. L.; Commoner, B *Nature* **1965**, *207*, 1246.

(211) Woolum, J. C. C., B. *Biochem Biophys Acta* **1970**, *201*, 131.

(212) McBride, D. W. S., S. L.; Stone, F. G. A. *Inorganic Chemistry* **1962**, *1*, 386−388.

(213) Atkinson, F. L. B., H. E.; Brown, N. C.; Connelly, N. G.; Crossley, J. G.; Orpen, A. G.; Rieger, A. L.; Rieger, P. H. *Journal of the Chemical Society, Dalton Transactions* **1996**, 3491−3502.

(214) Reginato, N. M., C. T. C.; Pervitsky, D.; Li, L. *Journal of the American Chemical Society* **1999**, *121*, 10217.

(215) Wang, W. N., M., J.; Rauchfuss, T., B.; Stein, M. *Journal of the American Chemical Society* **2013**, *135*, 3633.

(216) Melzer, M. M. M., S.; Cardenas, A. J. P.; Williams, K. D.; Zhang, S.; Meyer, K.; Warren, T. H. *Inorganic Chemistry* **2012**, *51*, 8658−8660.

(217) Peters, J. W. *Met. Ions Life Sci.* **2009**, *6*.

(218) Pilet, E.; Nicolet, Y.; Mathevon, C.; Douki, T.; Fontecilla-Camps, J. C.; Fontecave, M. *FEBS letters* **2009**, *583*, 506.

(219) Nicolet, Y.; Rubach, J. K.; Posewitz, M. C.; Amara, P.; Mathevon, C.; Atta, M.; Fontecave, M.; Fontecilla-Camps, J. C. *The Journal of Biological Chemistry* **2008**, *283*, 18861.

(220) Dey, A. *Inorganic Chemistry* **2011**, *50*, 397.

(221) Bethel, R. D. D., M. Y. *Nature* **2013**, *499*, 40.

(222) Tard, C. L., X.; Ibrahim, S., K.; Bruschi, M.; De Gioia, L.; Davies, S., C.; Yang, X.; Wang, L.-S.; Sawers, G.; Pickett, C., J. *Nature* **2005**, *433*, 610.

(223) Darensbourg, M. Y. B., R. D. *Nature Chemistry* **2012**, *4*, 11.

(224) Camara, J., M.; Rauchfuss, T., B. *Nature Chemistry* **2011**, *4*, 26.

(225) Singleton, M. L.; Bhuvanesh, N.; Reibenspies, J. H.; Darensbourg, M. Y. *Angewandte Chemie* **2008**, *47*, 9492.

(226) Justice, A., K.; Rauchfuss, T., B.; Wilson, S., R. *Angewandte Chemie* **2007**, *46*, 6152.